

SEVEN-YEAR WILKINSON MICROWAVE ANISOTROPY PROBE (WMAP*) OBSERVATIONS: COSMOLOGICAL INTERPRETATION

E. KOMATSU¹, K. M. SMITH², J. DUNKLEY³, C. L. BENNETT⁴, B. GOLD⁴, G. HINSHAW⁵, N. JAROSIK⁶, D. LARSON⁴, M. R. NOLTA⁷, L. PAGE⁶, D. N. SPERGEL^{2,8}, M. HALPERN⁹, R. S. HILL¹⁰, A. KOGUT⁵, M. LIMON¹¹, S. S. MEYER¹², N. ODEGARD¹⁰, G. S. TUCKER¹³, J. L. WEILAND¹⁰, E. WOLLACK⁵, AND E. L. WRIGHT¹⁴

¹ Texas Cosmology Center and Department of Astronomy, University of Texas, Austin, 2511 Speedway, RLM 15.306, Austin, TX 78712, USA;
 komatsu@astro.as.utexas.edu

² Department of Astrophysical Sciences, Peyton Hall, Princeton University, Princeton, NJ 08544-1001, USA

³ Astrophysics, University of Oxford, Keble Road, Oxford, OX1 3RH, UK

⁴ Department of Physics & Astronomy, The Johns Hopkins University, 3400 North Charles Street, Baltimore, MD 21218-2686, USA

⁵ Code 665, NASA/Goddard Space Flight Center, Greenbelt, MD 20771, USA

⁶ Department of Physics, Jadwin Hall, Princeton University, Princeton, NJ 08544-0708, USA

⁷ Canadian Institute for Theoretical Astrophysics, 60 St. George Street, University of Toronto, Toronto, ON M5S 3H8, Canada

⁸ Princeton Center for Theoretical Physics, Princeton University, Princeton, NJ 08544, USA

⁹ Department of Physics and Astronomy, University of British Columbia, Vancouver, BC V6T 1Z1, Canada

¹⁰ ADNET Systems, Inc., 7515 Mission Drive, Suite A100 Lanham, MD 20706, USA

¹¹ Columbia Astrophysics Laboratory, 550 West 120th Street, Mail Code 5247, New York, NY 10027-6902, USA

¹² Department of Astrophysics and Physics, KICP and EFI, University of Chicago, Chicago, IL 60637, USA

¹³ Department of Physics, Brown University, 182 Hope Street, Providence, RI 02912-1843, USA

¹⁴ UCLA Physics & Astronomy, P.O. Box 951547, Los Angeles, CA 90095-1547, USA

Received 2010 January 26; accepted 2010 October 27; published 2011 January 11

ABSTRACT

The combination of seven-year data from *WMAP* and improved astrophysical data rigorously tests the standard cosmological model and places new constraints on its basic parameters and extensions. By combining the *WMAP* data with the latest distance measurements from the baryon acoustic oscillations (BAO) in the distribution of galaxies and the Hubble constant (H_0) measurement, we determine the parameters of the simplest six-parameter Λ CDM model. The power-law index of the primordial power spectrum is $n_s = 0.968 \pm 0.012$ (68% CL) for this data combination, a measurement that excludes the Harrison–Zel’dovich–Peebles spectrum by 99.5% CL. The other parameters, including those beyond the minimal set, are also consistent with, and improved from, the five-year results. We find no convincing deviations from the minimal model. The seven-year temperature power spectrum gives a better determination of the third acoustic peak, which results in a better determination of the redshift of the matter-radiation equality epoch. Notable examples of improved parameters are the total mass of neutrinos, $\sum m_\nu < 0.58$ eV (95% CL), and the effective number of neutrino species, $N_{\text{eff}} = 4.34^{+0.86}_{-0.88}$ (68% CL), which benefit from better determinations of the third peak and H_0 . The limit on a constant dark energy equation of state parameter from *WMAP*+BAO+ H_0 , without high-redshift Type Ia supernovae, is $w = -1.10 \pm 0.14$ (68% CL). We detect the effect of primordial helium on the temperature power spectrum and provide a new test of big bang nucleosynthesis by measuring $Y_p = 0.326 \pm 0.075$ (68% CL). We detect, and show on the map for the first time, the tangential and radial polarization patterns around hot and cold spots of temperature fluctuations, an important test of physical processes at $z = 1090$ and the dominance of adiabatic scalar fluctuations. The seven-year polarization data have significantly improved: we now detect the temperature–E-mode polarization cross power spectrum at 21σ , compared with 13σ from the five-year data. With the seven-year temperature–B-mode cross power spectrum, the limit on a rotation of the polarization plane due to potential parity-violating effects has improved by 38% to $\Delta\alpha = -1.1 \pm 1.4$ (statistical) ± 1.5 (systematic) (68% CL). We report significant detections of the Sunyaev–Zel’dovich (SZ) effect at the locations of known clusters of galaxies. The measured SZ signal agrees well with the expected signal from the X-ray data on a cluster-by-cluster basis. However, it is a factor of 0.5–0.7 times the predictions from “universal profile” of Arnaud et al., analytical models, and hydrodynamical simulations. We find, for the first time in the SZ effect, a significant difference between the cooling-flow and non-cooling-flow clusters (or relaxed and non-relaxed clusters), which can explain some of the discrepancy. This lower amplitude is consistent with the lower-than-theoretically expected SZ power spectrum recently measured by the South Pole Telescope Collaboration.

Key words: cosmic background radiation – cosmology: observations – dark matter – early universe – space vehicles

1. INTRODUCTION

A simple cosmological model, a flat universe with nearly scale-invariant adiabatic Gaussian fluctuations, has proven to

be a remarkably good fit to ever improving cosmic microwave background (CMB) data (Hinshaw et al. 2009; Reichardt et al. 2009; Brown et al. 2009), large-scale structure data (Reid et al. 2010b; Percival et al. 2010), supernova data (Hicken et al. 2009a; Kessler et al. 2009), cluster measurements (Vikhlinin et al. 2009b; Mantz et al. 2010c), distance measurements (Riess et al. 2009), and measurements of strong (Suyu et al. 2010;

* *WMAP* is the result of a partnership between Princeton University and NASA’s Goddard Space Flight Center. Scientific guidance is provided by the *WMAP* Science Team.

Fadeley et al. 2010) and weak (Massey et al. 2007; Fu et al. 2008; Schrabbach et al. 2010) gravitational lensing effects.

Observations of CMB have been playing an essential role in testing the model and constraining its basic parameters. The *WMAP* satellite (Bennett et al. 2003a, 2003b) has been measuring temperature and polarization anisotropies of the CMB over the full sky since 2001. With seven years of integration, the errors in the temperature spectrum at each multipole are dominated by cosmic variance (rather than by noise) up to $l \approx 550$, and the signal-to-noise at each multipole exceeds unity up to $l \approx 900$ (Larson et al. 2011). The power spectrum of primary CMB on smaller angular scales has been measured by other experiments up to $l \approx 3000$ (Reichardt et al. 2009; Brown et al. 2009; Lueker et al. 2010; Fowler et al. 2010).

The polarization data show the most dramatic improvements over our earlier *WMAP* results: the temperature–polarization cross power spectra measured by *WMAP* at $l \gtrsim 10$ are still dominated by noise, and the errors in the seven-year cross power spectra have improved by nearly 40% compared to the five-year cross power spectra. While the error in the power spectrum of the cosmological *E*-mode polarization (Seljak & Zaldarriaga 1997; Kamionkowski et al. 1997b) averaged over $l = 2\text{--}7$ is cosmic-variance limited, individual multipoles are not yet cosmic-variance limited. Moreover, the cosmological *B*-mode polarization has not been detected (Nolta et al. 2009; Komatsu et al. 2009a; Brown et al. 2009; Chiang et al. 2010).

The temperature–polarization (TE and TB) power spectra offer unique tests of the standard model. The TE spectrum can be predicted given the cosmological constraints from the temperature power spectrum, and the TB spectrum is predicted to vanish in a parity-conserving universe. They also provide a clear physical picture of how the CMB polarization is created from quadrupole temperature anisotropy. We show the success of the standard model in an even more striking way by measuring this correlation in map space, rather than in harmonic space.

The constraints on the basic six parameters of a flat Λ CDM model (see Table 1), as well as those on the parameters beyond the minimal set (see Table 2), continue to improve with the seven-year *WMAP* temperature and polarization data, combined with improved external astrophysical data sets. In this paper, we shall give an update on the cosmological parameters, as determined from the latest cosmological data set. Our best estimates of the cosmological parameters are presented in the last columns of Tables 1 and 2 under the name “*WMAP+BAO+H₀*.” While this is the minimal combination of robust data sets such that adding other data sets does not significantly improve most parameters, the other data combinations provide better limits than *WMAP+BAO+H₀* in some cases. For example, adding the small-scale CMB data improves the limit on the primordial helium abundance, Y_p (see Table 3 and Section 4.8), the supernova data are needed to improve limits on properties of dark energy (see Table 4 and Section 5), and the power spectrum of Luminous Red Galaxies (LRGs; see Section 3.2.3) improves limits on properties of neutrinos (see footnotes g, h, and i in Table 2 and Sections 4.6 and 4.7).

The CMB can also be used to probe the abundance as well as the physics of clusters of galaxies, via the SZ effect (Zel'dovich & Sunyaev 1969; Sunyaev & Zel'dovich 1972). In this paper, we present the *WMAP* measurement of the averaged profile of SZ effect measured toward the directions of known clusters of galaxies, and discuss implications of the *WMAP* measurement for the very small-scale ($l \gtrsim 3000$) power spectrum recently measured by the South Pole Telescope (SPT; Lueker et al. 2010)

and Atacama Cosmology Telescope (ACT; Fowler et al. 2010) collaborations.

This paper is one of six papers on the analysis of the *WMAP* seven-year data: Jarosik et al. (2011) report on the data processing, map-making, and systematic error limits; Gold et al. (2011) on the modeling, understanding, and subtraction of the temperature and polarized foreground emission; Larson et al. (2011) on the measurements of the temperature and polarization power spectra, extensive testing of the parameter estimation methodology by Monte Carlo simulations, and the cosmological parameters inferred from the *WMAP* data alone; Bennett et al. (2011) on the assessments of statistical significance of various “anomalies” in the *WMAP* temperature map reported in the literature; and Weiland et al. (2011) on *WMAP*'s measurements of the brightnesses of planets and various celestial calibrators.

This paper is organized as follows. In Section 2, we present results from the new method of analyzing the polarization patterns around temperature hot and cold spots. In Section 3, we briefly summarize new aspects of our analysis of the *WMAP* seven-year temperature and polarization data, as well as improvements from the five-year data. In Section 4, we present updates on various cosmological parameters, except for dark energy. We explore the nature of dark energy in Section 5. In Section 6, we present limits on primordial non-Gaussianity parameters f_{NL} . In Section 7, we report detection, characterization, and interpretation of the SZ effect toward locations of known clusters of galaxies. We conclude in Section 8.

2. CMB POLARIZATION ON THE MAP

2.1. Motivation

Electron–photon scattering converts quadrupole temperature anisotropy in the CMB at the decoupling epoch, $z = 1090$, into linear polarization (Rees 1968; Basko & Polnarev 1980; Kaiser 1983; Bond & Efstathiou 1984; Polnarev 1985; Bond & Efstathiou 1987; Harari & Zaldarriaga 1993). This produces a correlation between the temperature pattern and the polarization pattern (Coulson et al. 1994; Crittenden et al. 1995). Different mechanisms for generating fluctuations produce distinctive correlated patterns in temperature and polarization:

1. Adiabatic scalar fluctuations predict a radial polarization pattern around temperature cold spots and a tangential pattern around temperature hot spots on angular scales greater than the horizon size at the decoupling epoch, $\gtrsim 2^\circ$. On angular scales smaller than the sound horizon size at the decoupling epoch, *both* radial *and* tangential patterns are formed around both hot and cold spots, as the acoustic oscillation of the CMB modulates the polarization pattern (Coulson et al. 1994). As we have not seen any evidence for non-adiabatic fluctuations (Komatsu et al. 2009a, see Section 4.4 for the seven-year limits), in this section we shall assume that fluctuations are purely adiabatic.
2. Tensor fluctuations predict the opposite pattern: the temperature cold spots are surrounded by a tangential polarization pattern, while the hot spots are surrounded by a radial pattern (Crittenden et al. 1995). Since there is no acoustic oscillation for tensor modes, there is no modulation of polarization patterns around temperature spots on small angular scales. We do not expect this contribution to be visible in the *WMAP* data, given the noise level.
3. Defect models predict that there should be minimal correlations between temperature and polarization on $2^\circ \lesssim \theta \lesssim 10^\circ$ (Seljak et al. 1997). The detection of large-scale

Table 1
Summary of the Cosmological Parameters of Λ CDM Model^a

Class	Parameter	WMAP Seven-year ML ^b	WMAP+BAO+ H_0 ML	WMAP Seven-year Mean ^c	WMAP+BAO+ H_0 Mean
Primary	$100\Omega_bh^2$	2.227	2.253	$2.249^{+0.056}_{-0.057}$	2.255 ± 0.054
	$\Omega_c h^2$	0.1116	0.1122	0.1120 ± 0.0056	0.1126 ± 0.0036
	Ω_Λ	0.729	0.728	$0.727^{+0.030}_{-0.029}$	0.725 ± 0.016
	n_s	0.966	0.967	0.967 ± 0.014	0.968 ± 0.012
	τ	0.085	0.085	0.088 ± 0.015	0.088 ± 0.014
	$\Delta_R^2(k_0)^d$	2.42×10^{-9}	2.42×10^{-9}	$(2.43 \pm 0.11) \times 10^{-9}$	$(2.430 \pm 0.091) \times 10^{-9}$
Derived	σ_8	0.809	0.810	$0.811^{+0.030}_{-0.031}$	0.816 ± 0.024
	H_0	$70.3 \text{ km s}^{-1} \text{ Mpc}^{-1}$	$70.4 \text{ km s}^{-1} \text{ Mpc}^{-1}$	$70.4 \pm 2.5 \text{ km s}^{-1} \text{ Mpc}^{-1}$	$70.2 \pm 1.4 \text{ km s}^{-1} \text{ Mpc}^{-1}$
	Ω_b	0.0451	0.0455	0.0455 ± 0.0028	0.0458 ± 0.0016
	Ω_c	0.226	0.226	0.228 ± 0.027	0.229 ± 0.015
	$\Omega_m h^2$	0.1338	0.1347	$0.1345^{+0.056}_{-0.055}$	0.1352 ± 0.0036
	z_{reion}^e	10.4	10.3	10.6 ± 1.2	10.6 ± 1.2
	t_0^f	13.79 Gyr	13.76 Gyr	$13.77 \pm 0.13 \text{ Gyr}$	$13.76 \pm 0.11 \text{ Gyr}$

Notes.

^a The parameters listed here are derived using the RECFAST 1.5 and version 4.1 of the WMAP likelihood code. All the other parameters in the other tables are derived using the RECFAST 1.4.2 and version 4.0 of the WMAP likelihood code, unless stated otherwise. The difference is small. See Appendix A for comparison.

^b Larson et al. (2011). “ML” refers to the maximum likelihood parameters.

^c Larson et al. (2011). “Mean” refers to the mean of the posterior distribution of each parameter. The quoted errors show the 68% confidence levels (CLs).

^d $\Delta_R^2(k) = k^3 P_R(k)/(2\pi^2)$ and $k_0 = 0.002 \text{ Mpc}^{-1}$.

^e “Redshift of reionization,” if the universe was reionized instantaneously from the neutral state to the fully ionized state at z_{reion} . Note that these values are somewhat different from those in Table 1 of Komatsu et al. (2009a), largely because of the changes in the treatment of reionization history in the Boltzmann code CAMB (Lewis 2008).

^f The present-day age of the universe.

Table 2

Summary of the 95% Confidence Limits on Deviations From the Simple (Flat, Gaussian, Adiabatic, Power-law) Λ CDM Model Except for Dark Energy Parameters

Section	Name	Case	WMAP Seven-year	WMAP+BAO+SN ^a	WMAP+BAO+ H_0
Section 4.1	Grav. wave ^b	No running ind.	$r < 0.36^c$	$r < 0.20$	$r < 0.24$
Section 4.2	Running index	No grav. wave	$-0.084 < dn_s/d \ln k < 0.020^c$	$-0.065 < dn_s/d \ln k < 0.010$	$-0.061 < dn_s/d \ln k < 0.017$
Section 4.3	Curvature	$w = -1$	N/A	$-0.0178 < \Omega_k < 0.0063$	$-0.0133 < \Omega_k < 0.0084$
Section 4.4	Adiabaticity	Axion	$\alpha_0 < 0.13^c$	$\alpha_0 < 0.064$	$\alpha_0 < 0.077$
		Curvaton	$\alpha_{-1} < 0.011^c$	$\alpha_{-1} < 0.0037$	$\alpha_{-1} < 0.0047$
Section 4.5	Parity violation	Chern-Simons ^d	$-5.0 < \Delta\alpha < 2.8^e$	N/A	N/A
Section 4.6	Neutrino mass ^f	$w = -1$	$\sum m_\nu < 1.3 \text{ eV}^c$	$\sum m_\nu < 0.71 \text{ eV}$	$\sum m_\nu < 0.58 \text{ eV}^g$
		$w \neq -1$	$\sum m_\nu < 1.4 \text{ eV}^c$	$\sum m_\nu < 0.91 \text{ eV}$	$\sum m_\nu < 1.3 \text{ eV}^h$
Section 4.7	Relativistic species	$w = -1$	$N_{\text{eff}} > 2.7^c$	N/A	$4.34^{+0.86}_{-0.88} \text{ (68\% CL)}^i$
Section 6	Gaussianity ^j	Local	$-10 < f_{NL}^{\text{local}} < 74^k$	N/A	N/A
		Equilateral	$-214 < f_{NL}^{\text{equil}} < 266$	N/A	N/A
		Orthogonal	$-410 < f_{NL}^{\text{orthog}} < 6$	N/A	N/A

Notes.

^a “SN” denotes the “Constitution” sample of Type Ia supernovae compiled by Hicken et al. (2009a), which is an extension of the “Union” sample (Kowalski et al. 2008) that we used for the five-year “WMAP+BAO+SN” parameters presented in Komatsu et al. (2009a). Systematic errors in the supernova data are not included. While the parameters in this column can be compared directly to the five-year WMAP+BAO+SN parameters, they may not be as robust as the “WMAP+BAO+ H_0 ” parameters, as the other compilations of the supernova data do not give the same answers (Hicken et al. 2009a; Kessler et al. 2009). See Section 3.2.4 for more discussion. The SN data will be used to put limits on dark energy properties. See Section 5 and Table 4.

^b In the form of the tensor-to-scalar ratio, r , at $k = 0.002 \text{ Mpc}^{-1}$.

^c Larson et al. (2011).

^d For an interaction of the form given by $[\phi(t)/M] F_{\alpha\beta} \tilde{F}^{\alpha\beta}$, the polarization rotation angle is $\Delta\alpha = M^{-1} \int \frac{dt}{a} \dot{\phi}$.

^e The 68% CL limit is $\Delta\alpha = -1.1^\circ \pm 1.2^\circ (\text{stat.}) \pm 1.5^\circ (\text{sys.})$, where the first error is statistical and the second error is systematic.

^f $\sum m_\nu = 94(\Omega_\nu h^2) \text{ eV}$.

^g For WMAP+LRG+ H_0 , $\sum m_\nu < 0.44 \text{ eV}$.

^h For WMAP+LRG+ H_0 , $\sum m_\nu < 0.71 \text{ eV}$.

ⁱ The 95% limit is $2.7 < N_{\text{eff}} < 6.2$. For WMAP+LRG+ H_0 , $N_{\text{eff}} = 4.25 \pm 0.80$ (68%) and $2.8 < N_{\text{eff}} < 5.9$ (95%).

^j V+W map masked by the KQ75y7 mask. The Galactic foreground templates are marginalized over.

^k When combined with the limit on f_{NL}^{local} from SDSS, $-29 < f_{NL}^{\text{local}} < 70$ (Slosar et al. 2008), we find $-5 < f_{NL}^{\text{local}} < 59$.

temperature polarization fluctuations rules out any causal models as the primary mechanism for generating the CMB fluctuations (Spergel & Zaldarriaga 1997). This implies that

the fluctuations were either generated during an accelerating phase in the early universe or were present at the time of the initial singularity.

Table 3
Primordial Helium Abundance^a

WMAP Only	WMAP+ACBAR+QUaD
$Y_p < 0.51$ (95% CL)	$Y_p = 0.326 \pm 0.075$ (68% CL) ^b

Notes.^a See Section 4.8.^b The 95% CL limit is $0.16 < Y_p < 0.46$. For WMAP+ACBAR+QUaD+LRG+ H_0 , $Y_{\text{He}} = 0.349 \pm 0.064$ (68% CL) and $0.20 < Y_p < 0.46$ (95% CL).

This section presents the first direct measurement of the predicted pattern of adiabatic scalar fluctuations in CMB polarization maps. We stack maps of Stokes Q and U around temperature hot and cold spots to show the expected polarization pattern at the statistical significance level of 8σ . While we have detected the TE correlations in the first year data (Kogut et al. 2003), we present here the direct real space pattern around hot and cold spots. In Section 2.5, we discuss the relationship between the two measurements.

2.2. Measuring Peak–Polarization Correlation

We first identify temperature hot (or cold) spots, and then stack the polarization data (i.e., Stokes Q and U) on the locations of the spots. As we shall show below, the resulting polarization data are equivalent to the temperature peak–polarization correlation function which is similar to, but different in an important way from, the temperature–polarization correlation function.

2.2.1. Q_r and U_r : Transformed Stokes Parameters

Our definitions of Stokes Q and U follow that of Kogut et al. (2003): the polarization that is parallel to the Galactic meridian is $Q > 0$ and $U = 0$. Starting from this, the polarization that is rotated by 45° from east to west (clockwise, as seen by an observer on Earth looking up at the sky) has $Q = 0$ and $U > 0$, that perpendicular to the Galactic meridian has $Q < 0$ and $U = 0$, and that rotated further by 45° from east to west has $Q = 0$ and $U < 0$. With one more rotation we go back to $Q > 0$ and $U = 0$. We show this in Figure 1.

As the predicted polarization pattern around temperature spots is either radial or tangential, we find it most convenient to work with Q_r and U_r first introduced by Kamionkowski et al. (1997b):

$$Q_r(\theta) = -Q(\theta) \cos(2\phi) - U(\theta) \sin(2\phi), \quad (1)$$

Table 4
Summary of the 68% Limits on Dark Energy Properties from WMAP Combined with Other Data Sets

Section	Curvature	Parameter	+BAO+ H_0	+BAO+ $H_0+D_{\Delta t}$ ^a	+BAO+SN ^b
Section 5.1	$\Omega_k = 0$	Constant w	-1.10 ± 0.14	-1.08 ± 0.13	-0.980 ± 0.053
Section 5.2	$\Omega_k \neq 0$	Constant w	-1.44 ± 0.27	-1.39 ± 0.25	$-0.999^{+0.057}_{-0.056}$
		Ω_k	$-0.0125^{+0.0064}_{-0.0067}$	$-0.0111^{+0.0060}_{-0.0063}$	$-0.0057^{+0.0067}_{-0.0068}$
			$+H_0+\text{SN}$	$+BAO+H_0+\text{SN}$	$+BAO+H_0+D_{\Delta t}+\text{SN}$
Section 5.3	$\Omega_k = 0$	w_0	-0.83 ± 0.16	-0.93 ± 0.13	-0.93 ± 0.12
		w_a	$-0.80^{+0.84}_{-0.83}$	$-0.41^{+0.72}_{-0.71}$	$-0.38^{+0.66}_{-0.65}$

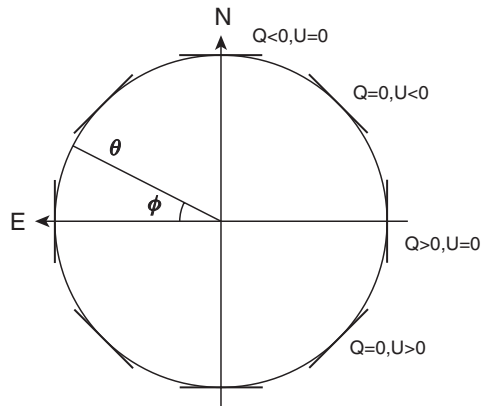
Notes.^a “ $D_{\Delta t}$ ” denotes the time-delay distance to the lens system B1608+656 at $z = 0.63$ measured by Suyu et al. (2010). See Section 3.2.5 for details.^b “SN” denotes the “Constitution” sample of Type Ia supernovae compiled by Hicken et al. (2009a), which is an extension of the “Union” sample (Kowalski et al. 2008) that we used for the five-year “WMAP+BAO+SN” parameters presented in Komatsu et al. (2009a). Systematic errors in the supernova data are not included.

Figure 1. Coordinate system for Stokes Q and U . We use Galactic coordinates with north up and east left. In this example, Q_r is always negative, and U_r is always zero. When $Q_r > 0$ and $U_r = 0$, the polarization pattern is radial.

$$U_r(\theta) = Q(\theta) \sin(2\phi) - U(\theta) \cos(2\phi). \quad (2)$$

These transformed Stokes parameters are defined with respect to the new coordinate system that is rotated by ϕ , and thus they are defined with respect to the line connecting the temperature spot at the center of the coordinate and the polarization at an angular distance θ from the center (also see Figure 1). Note that we have used the small-angle (flat-sky) approximation for simplicity of the algebra. This approximation is justified as we are interested in relatively small angular scales, $\theta < 5^\circ$.

The above definition of Q_r is equivalent to the so-called tangential shear statistic used by the weak gravitational lensing community. By following what has been already done for the tangential shear, we can find the necessary formulae for Q_r and U_r . Specifically, we shall follow the derivations given in Jeong et al. (2009).

With the small-angle approximation, Q and U are related to the E - and B -mode polarization in Fourier space (Seljak & Zaldarriaga 1997; Kamionkowski et al. 1997a) as

$$-Q(\theta) = \int \frac{d^2\mathbf{l}}{(2\pi)^2} [E_l \cos(2\phi) - B_l \sin(2\phi)] e^{i\mathbf{l}\cdot\theta}, \quad (3)$$

$$-U(\theta) = \int \frac{d^2\mathbf{l}}{(2\pi)^2} [E_l \sin(2\phi) + B_l \cos(2\phi)] e^{i\mathbf{l}\cdot\theta}, \quad (4)$$

where ϕ is the angle between \mathbf{l} and the line of Galactic latitude, $\mathbf{l} = (l \cos \phi, l \sin \phi)$. Note that we have included

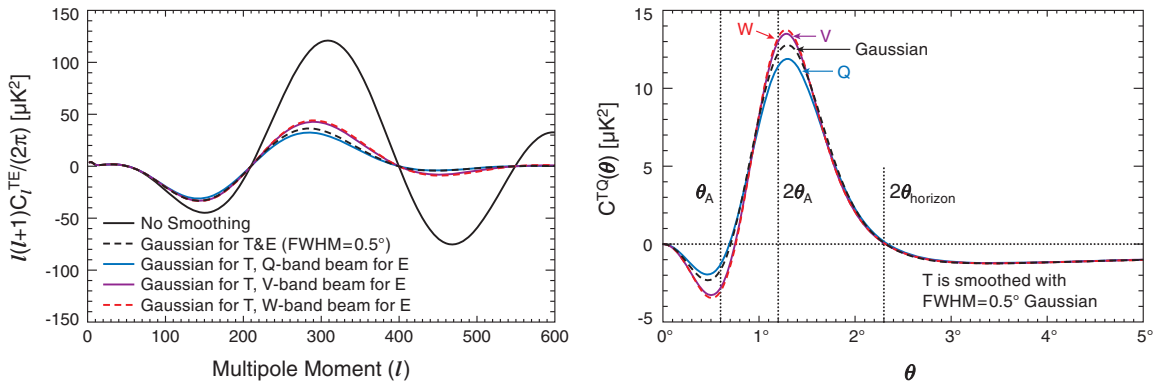


Figure 2. Temperature–polarization cross correlation with various smoothing functions. Left: the TE power spectrum with no smoothing is shown in the black solid line. For the other curves, the temperature is always smoothed with a \$0.5^\circ\$ (FWHM) Gaussian, whereas the polarization is smoothed with either the same Gaussian (black dashed), Q-band beam (blue solid), V-band beam (purple solid), or W-band beam (red dashed). Right: the corresponding spatial temperature–\$Q_r\$ correlation functions. The vertical dotted lines indicate (from left to right): the acoustic scale, \$2\times\$ the acoustic scale, and \$2\times\$ the horizon size, all evaluated at the decoupling epoch.

the negative signs on the left-hand side because our sign convention for the Stokes parameters is opposite of that used in Equation (38) of Zaldarriaga & Seljak (1997). The transformed Stokes parameters are given by

$$-Q_r(\theta) = - \int \frac{d^2\mathbf{l}}{(2\pi)^2} \{E_{\mathbf{l}} \cos[2(\phi - \varphi)] + B_{\mathbf{l}} \sin[2(\phi - \varphi)]\} e^{i\mathbf{l}\cdot\theta}, \quad (5)$$

$$-U_r(\theta) = \int \frac{d^2\mathbf{l}}{(2\pi)^2} \{E_{\mathbf{l}} \sin[2(\phi - \varphi)] - B_{\mathbf{l}} \cos[2(\phi - \varphi)]\} e^{i\mathbf{l}\cdot\theta}. \quad (6)$$

The stacking of \$Q_r\$ and \$U_r\$ at the locations of temperature peaks can be written as

$$\langle Q_r \rangle(\theta) = \frac{1}{N_{\text{pk}}} \int d^2\hat{\mathbf{n}} M(\hat{\mathbf{n}}) \langle n_{\text{pk}}(\hat{\mathbf{n}}) Q_r(\hat{\mathbf{n}} + \hat{\theta}) \rangle, \quad (7)$$

$$\langle U_r \rangle(\theta) = \frac{1}{N_{\text{pk}}} \int d^2\hat{\mathbf{n}} M(\hat{\mathbf{n}}) \langle n_{\text{pk}}(\hat{\mathbf{n}}) U_r(\hat{\mathbf{n}} + \hat{\theta}) \rangle, \quad (8)$$

where the angle bracket, \$\langle \dots \rangle\$, denotes the average over the locations of peaks, \$n_{\text{pk}}(\hat{\mathbf{n}})\$ is the surface number density of peaks (of the temperature fluctuation) at the location \$\hat{\mathbf{n}}\$, \$N_{\text{pk}}\$ is the total number of temperature peaks used in the stacking analysis, and \$M(\hat{\mathbf{n}})\$ is equal to 0 at the masked pixels and 1 otherwise. Defining the density contrast of peaks, \$\delta_{\text{pk}} \equiv n_{\text{pk}}/\bar{n}_{\text{pk}} - 1\$, we find

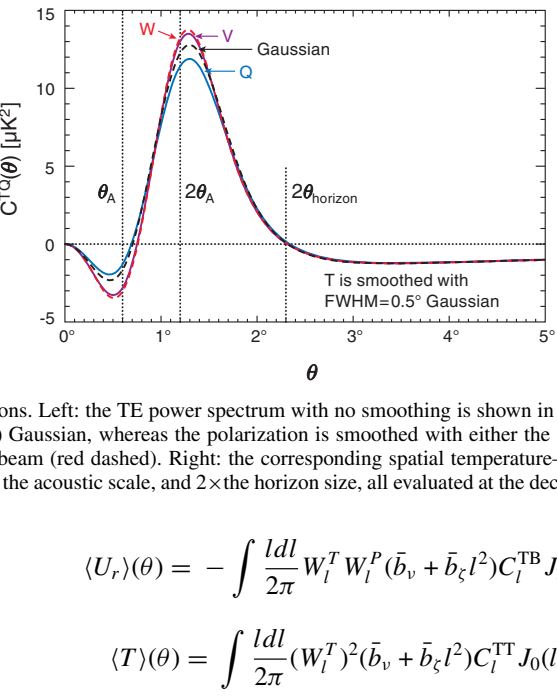
$$\langle Q_r \rangle(\theta) = \frac{1}{f_{\text{sky}}} \int \frac{d^2\hat{\mathbf{n}}}{4\pi} M(\hat{\mathbf{n}}) \langle \delta_{\text{pk}}(\hat{\mathbf{n}}) Q_r(\hat{\mathbf{n}} + \hat{\theta}) \rangle, \quad (9)$$

$$\langle U_r \rangle(\theta) = \frac{1}{f_{\text{sky}}} \int \frac{d^2\hat{\mathbf{n}}}{4\pi} M(\hat{\mathbf{n}}) \langle \delta_{\text{pk}}(\hat{\mathbf{n}}) U_r(\hat{\mathbf{n}} + \hat{\theta}) \rangle, \quad (10)$$

where \$f_{\text{sky}} \equiv \int M(\hat{\mathbf{n}}) d^2\hat{\mathbf{n}}/(4\pi)\$ is the fraction of sky outside of the mask, and we have used \$N_{\text{pk}} = 4\pi f_{\text{sky}} \bar{n}_{\text{pk}}\$.

In Appendix B, we use the statistics of peaks of Gaussian random fields to relate \$\langle Q_r \rangle\$ to the temperature–\$E\$-mode polarization cross power spectrum \$C_l^{\text{TE}}\$, \$\langle U_r \rangle\$ to the temperature–\$B\$-mode polarization cross power spectrum \$C_l^{\text{TB}}\$, and the stacked temperature profile, \$\langle T \rangle\$, to the temperature power spectrum \$C_l^{\text{TT}}\$. We find

$$\langle Q_r \rangle(\theta) = - \int \frac{ldl}{2\pi} W_l^T W_l^P (\bar{b}_v + \bar{b}_\zeta l^2) C_l^{\text{TE}} J_2(l\theta), \quad (11)$$



$$\langle U_r \rangle(\theta) = - \int \frac{ldl}{2\pi} W_l^T W_l^P (\bar{b}_v + \bar{b}_\zeta l^2) C_l^{\text{TB}} J_2(l\theta), \quad (12)$$

$$\langle T \rangle(\theta) = \int \frac{ldl}{2\pi} (W_l^T)^2 (\bar{b}_v + \bar{b}_\zeta l^2) C_l^{\text{TT}} J_0(l\theta), \quad (13)$$

where \$W_l^T\$ and \$W_l^P\$ are the harmonic transform of window functions, which are a combination of the experimental beam, pixel window, and any other additional smoothing applied to the temperature and polarization data, respectively, and \$\bar{b}_v + \bar{b}_\zeta l^2\$ is the “scale-dependent bias” of peaks found by Desjacques (2008) averaged over peaks. See Appendix B for details.

2.2.2. Prediction and Physical Interpretation

What do \$\langle Q_r \rangle(\theta)\$ and \$\langle U_r \rangle(\theta)\$ look like? The \$Q_r\$ map is expected to be non-zero for a cosmological signal, while the \$U_r\$ map is expected to vanish in a parity-conserving universe unless some systematic error rotates the polarization plane uniformly.

To understand the shape of \$Q_r\$ as well as its physical implications, let us begin by showing the smoothed \$C_l^{\text{TE}}\$ spectra and the corresponding temperature–\$Q_r\$ correlation functions, \$C^{TQ_r}(\theta)\$, in Figure 2. (Note that \$C^{TQ_r}\$ and \$C^{TU_r}\$ can be computed from Equations (11) and (12), respectively, with \$b_v = 1\$ and \$b_\zeta = 0\$.) This shows three distinct effects causing polarization of CMB (see Hu & White 1997, for a pedagogical review):

1. \$\theta \gtrsim 2\theta_{\text{horizon}}\$, where \$\theta_{\text{horizon}}\$ is the angular size of the radius of the horizon size at the decoupling epoch. Using the comoving horizon size of \$r_{\text{horizon}} = 0.286\$ Gpc and the comoving angular diameter distance to the decoupling epoch of \$d_A = 14\$ Gpc as derived from the WMAP data, we find \$\theta_{\text{horizon}} = 1.2^\circ\$. As this scale is so much greater than the sound horizon size (see below), only gravity affects the physics. Suppose that there is a Newtonian gravitational potential, \$\Phi_N\$, at the center of a perturbation, \$\theta = 0\$. If it is overdense at the center, \$\Phi_N < 0\$, and thus it is a cold spot according to the Sachs–Wolfe formula (Sachs & Wolfe 1967), \$\Delta T/T = \Phi_N/3 < 0\$. The photon fluid in this region will flow into the gravitational potential well, creating a converging flow. Such a flow creates the quadrupole temperature anisotropy around an electron at \$\theta \geq 2\theta_{\text{horizon}}\$, producing polarization that is radial, i.e., \$Q_r > 0\$. Since the temperature is negative, we obtain \$\langle T Q_r \rangle < 0\$, i.e., anti-correlation (Coulson et al. 1994). On the other hand,

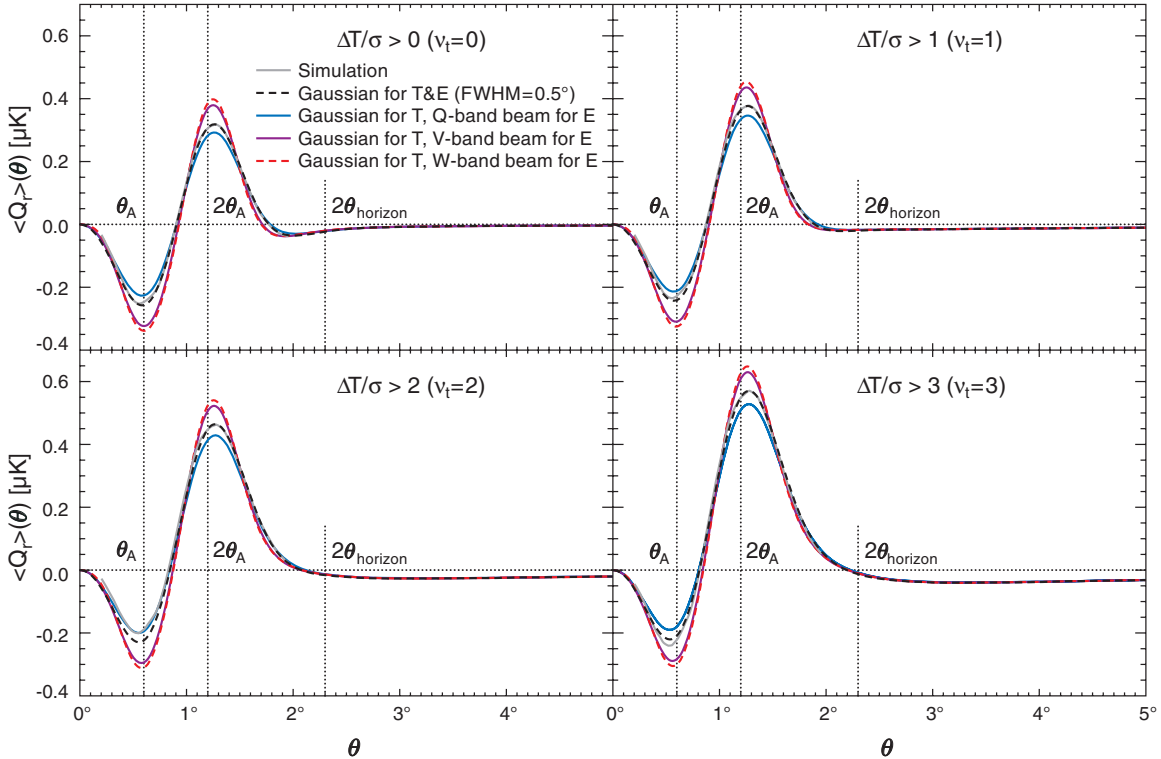


Figure 3. Predicted temperature peak–polarization cross correlation, as measured by the stacked profile of the transformed Stokes Q_r , computed from Equation (11) for various values of the threshold peak heights. The temperature is always smoothed with a $0^{\circ}5$ (FWHM) Gaussian, whereas the polarization is smoothed with either the same Gaussian (black dashed), Q-band beam (blue solid), V-band beam (purple solid), or W-band beam (red dashed). Top left: all temperature hot spots are stacked. Top right: spots greater than 1σ are stacked. Bottom left: spots greater than 2σ are stacked. Bottom right: spots greater than 3σ are stacked. The light gray lines show the average of the measurements from noiseless simulations with a Gaussian smoothing of $0^{\circ}5$ FWHM. The agreement is excellent.

if it is overdense at the center, then the photon fluid moves outward, producing polarization that is tangential, i.e., $Q_r < 0$. Since the temperature is positive, we obtain $\langle T Q_r \rangle < 0$, i.e., anti-correlation. The anti-correlation at $\theta \geq 2\theta_{\text{horizon}}$ is a smoking gun for the presence of super-horizon fluctuations at the decoupling epoch (Spergel & Zaldarriaga 1997), which has been confirmed by the *WMAP* data (Peiris et al. 2003).

2. $\theta \simeq 2\theta_A$, where θ_A is the angular size of the radius of the *sound* horizon size at the decoupling epoch. Using the comoving sound horizon size of $r_s = 0.147$ Gpc and $d_A = 14$ Gpc as derived from the *WMAP* data, we find $\theta_A = 0^{\circ}6$. Again, consider a potential well with $\Phi_N < 0$ at the center. As the photon fluid flows into the well, it compresses, increasing the temperature of the photons. Whether or not this increase can reverse the sign of the temperature fluctuation (from negative to positive) depends on whether the initial perturbation was adiabatic. If it was adiabatic, then the temperature would reverse sign at $\theta \lesssim 2\theta_{\text{horizon}}$. Note that the photon fluid is still flowing in, and thus the polarization direction is radial, $Q_r > 0$. However, now that the temperature is positive, the correlation reverses sign: $\langle T Q_r \rangle > 0$. A similar argument (with the opposite sign) can be used to show the same result, $\langle T Q_r \rangle > 0$, for $\Phi_N > 0$ at the center. As an aside, the temperature reverses sign on smaller angular scales for isocurvature fluctuations.
3. $\theta \simeq \theta_A$. Again, consider a potential well with $\Phi_N < 0$ at the center. At $\theta \lesssim 2\theta_A$, the pressure of the photon fluid is so great that it can slow down the flow of the fluid. Eventually, at $\theta \sim \theta_A$, the pressure becomes large enough to reverse

the direction of the flow (i.e., the photon fluid expands). As a result the polarization direction becomes tangential, $Q_r < 0$; however, as the temperature is still positive, the correlation reverses sign again: $\langle T Q_r \rangle < 0$.

On even smaller scales, the correlation reverses sign again (see Figure 2 of Coulson et al. 1994) because the temperature gets too cold due to expansion. We do not see this effect in Figure 2 because of the smoothing. Lastly, there is no correlation between T and Q_r at $\theta = 0$ because of symmetry.

These features are essentially preserved in the peak–polarization correlation as measured by the stacked polarization profiles. We show them in Figure 3 for various values of the threshold peak heights. The important difference is that, thanks to the scale-dependent bias $\propto l^2$, the small-scale trough at $\theta \simeq \theta_A$ is enhanced, making it easier to observe. On the other hand, the large-scale anti-correlation is suppressed. We can therefore conclude that, with the *WMAP* data, we should be able to measure the compression phase at $\theta \simeq 2\theta_A = 1^{\circ}2$, as well as the reversal phase at $\theta \simeq \theta_A = 0^{\circ}6$. We also show the profiles calculated from numerical simulations (gray solid lines). The agreement with Equation (11) is excellent. We also show the predicted profiles of the stacked temperature data in Figure 4.

2.3. Analysis Method

2.3.1. Temperature Data

We use the foreground-reduced V + W temperature map at the HEALPix resolution of $N_{\text{side}} = 512$ to find temperature peaks. First, we smooth the foreground-reduced temperature maps in

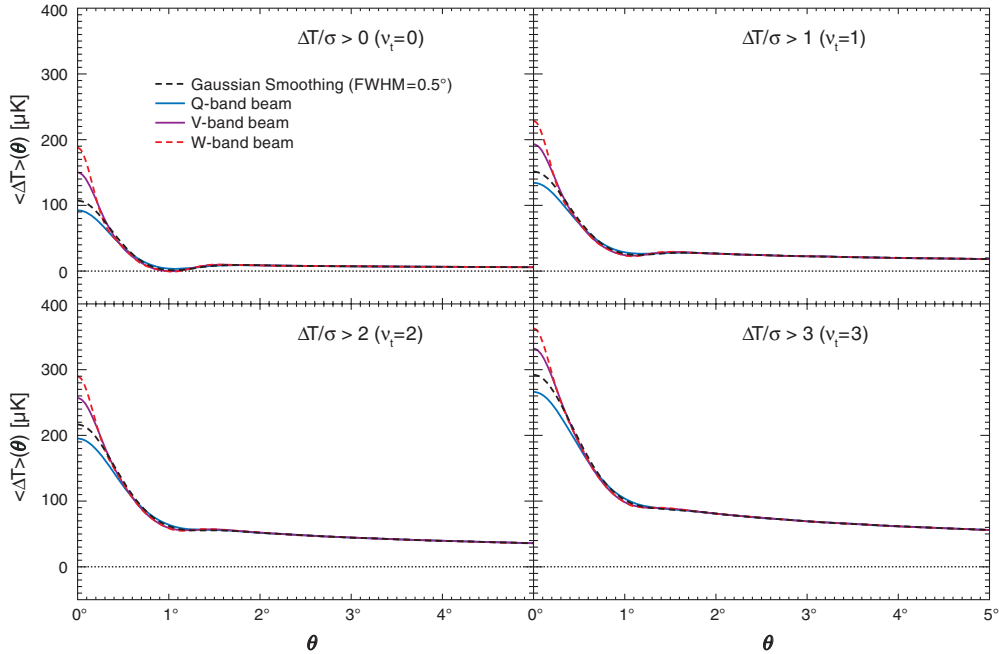


Figure 4. Predicted temperature peak–temperature correlation, as measured by the stacked temperature profile, computed from Equation (13) for various values of the threshold peak heights. The choices of the smoothing functions and the threshold peak heights are the same as in Figure 3.

six differencing assemblies (DAs) (V1, V2, W1, W2, W3, W4) to a common resolution of 0.5° (FWHM) using

$$\Delta T(\hat{\mathbf{n}}) = \sum_{lm} a_{lm} \frac{W_l^T}{b_l} Y_{lm}(\hat{\mathbf{n}}), \quad (14)$$

where b_l is the appropriate beam transfer function for each DA (Jarosik et al. 2011), and $W_l^T = p_l \exp[-l(l+1)\sigma_{\text{FWHM}}^2/(16 \ln 2)]$ is the pixel window function for $N_{\text{side}} = 512$, p_l , times the spherical harmonic transform of a Gaussian with $\sigma_{\text{FWHM}} = 0.5^{\circ}$. We then co-add the foreground-reduced V- and W-band maps with the inverse noise variance weighting, and remove the monopole from the region outside of the mask (which is already negligibly small, $1.07 \times 10^{-4} \mu\text{K}$). For the mask, we combine the new seven-year KQ85 mask, KQ85y7 (defined in Gold et al. 2011; also see Section 3.1) and P06 masks, leaving 68.7% of the sky available for the analysis.

We find the locations of minima and maxima using the software “hotspot” in the HEALPix package (Gorski et al. 2005). Over the full sky (without the mask), we find 20953 maxima and 20974 minima. As the maxima and minima found by hotspot still contain negative and positive peaks, respectively, we further select the “hot spots” by removing all negative peaks from maxima, and the “cold spots” by removing all positive peaks from minima. This procedure corresponds to setting the threshold peak height to $v_t = 0$; thus, our prediction for $\langle Q_r \rangle(\theta)$ is the top left panel of Figure 3.

Outside of the mask, we find 12,387 hot spots and 12,628 cold spots. The rms temperature fluctuation is $\sigma_0 = 83.9 \mu\text{K}$. What does the theory predict? Using Equation (B15) with the power spectrum $C_l^{\text{TT}} = (C_l^{\text{TT,signal}} p_l^2 + N_l^{\text{TT}}/b_l^2) \exp[-l(l+1)\sigma_{\text{FWHM}}^2/(8 \ln 2)]$ where $N_l^{\text{TT}} = 7.47 \times 10^{-3} \mu\text{K}^2 \text{sr}$ is the noise bias of the V+W map before Gaussian smoothing and $C_l^{\text{TT,signal}}$ is the five-year best-fitting power-law ΛCDM temperature power spectrum, we find $4\pi f_{\text{sky}} \bar{n}_{\text{pk}} = 1230$ for $v_t = 0$ and $f_{\text{sky}} = 0.687$; thus, the number of ob-

served hot and cold spots is consistent with the predicted number.¹⁵

2.3.2. Polarization Data

As for the polarization data, we use the *raw* (i.e., without foreground cleaning) polarization maps in V and W bands. We have checked that the cleaned maps give similar results with slightly larger error bars, which is consistent with the excess noise introduced by the template foreground cleaning procedure (Page et al. 2007; Gold et al. 2009, 2011). As we are focused on relatively small angular scales, $\theta \lesssim 2^{\circ}$, in this analysis, the results presented in this section would not be affected by a potential systematic effect causing an excess power in the W-band polarization data on large angular scales, $l \lesssim 10$. However, note that this excess power could just be a statistical fluctuation (Jarosik et al. 2011). We form two sets of the data: (1) V, W, and V + W band maps smoothed to a common resolution of 0.5° , and (2) V, W, and V + W band maps without any additional smoothing. The first set is used only for visualization, whereas the second set is used for the χ^2 analysis.

We extract a square region of $5^{\circ} \times 5^{\circ}$ around each temperature hot or cold spot. We then co-add the extracted T images with uniform weighting, and Q and U images with the inverse noise variance weighting. We have eliminated the pixels masked by KQ85y7 and P06 from each $5^{\circ} \times 5^{\circ}$ region when we co-add images, and thus the resulting stacked image has the smallest noise at the center (because the masked pixels usually appear near the edge of each image). We also accumulate the inverse noise variance per pixel as we co-add Q and U maps. The co-added inverse noise variance maps of Q and U will be used to estimate the errors of the stacked images of Q and U per pixel, which will then be used for the χ^2 analysis.

¹⁵ Note that the predicted number is $4\pi f_{\text{sky}} \bar{n}_{\text{pk}} = 10549$ if we ignore the noise bias; thus, even with a Gaussian smoothing, the contribution from noise is not negligible.

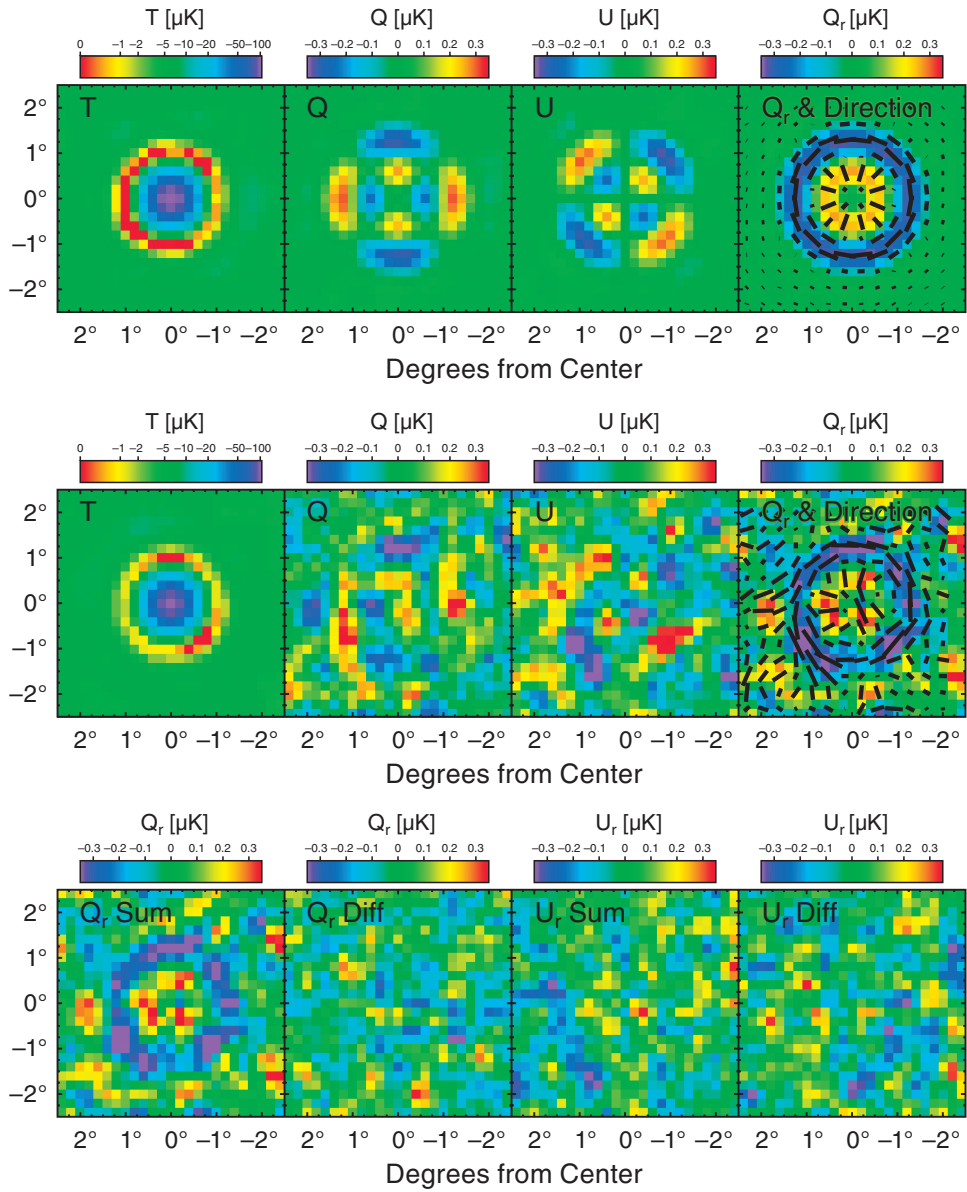


Figure 5. Stacked images of temperature and polarization data around temperature cold spots. Each panel shows a $5^\circ \times 5^\circ$ region with north up and east left. Both the temperature and polarization data have been smoothed to a common resolution of 0.5° . Top: simulated images with no instrumental noise. From left to right: the stacked temperature, Stokes Q , Stokes U , and transformed Stokes Q_r (see Equation (1)) overlaid with the polarization directions. Middle: WMAP seven-year $V + W$ data. In the observed map of Q_r , the compression phase at 1.2° and the reversal phase at 0.6° are clearly visible. Bottom: null tests. From left to right: the stacked Q_r from the sum map and from the difference map $(V - W)/2$, the stacked U_r from the sum map and from the difference map. The latter three maps are all consistent with noise. Note that U_r , which probes the TB correlation (see Equation (12)), is expected to vanish in a parity-conserving universe.

We find that the stacked images of Q and U have constant offsets, which is not surprising. Since these affect our determination of polarization directions, we remove monopoles from the stacked images of Q and U . The size of each pixel in the stacked image is 0.2° , and the number of pixels is $25^2 = 625$.

Finally, we compute Q_r and U_r from the stacked images of Stokes Q and U using Equations (1) and (2), respectively.

2.4. Results

In Figures 5 and 6, we show the stacked images of T , Q , U , Q_r , and U_r around temperature cold spots and hot spots, respectively. The peak values of the stacked temperature profiles agree with the predictions (see the dashed line in the top left panel of Figure 4). A dip in temperature (for hot spots; a bump for cold spots) at $\theta \simeq 1^\circ$ is clearly visible in the data. While the Stokes Q

and U measured from the data exhibit the expected features, they are still fairly noisy. The most striking images are the stacked Q_r (and T). The predicted features are clearly visible, particularly the compression phase at 1.2° and the reversal phase at 0.6° in Q_r : the polarization directions around temperature cold spots are radial at $\theta \simeq 0.6^\circ$ and tangential at $\theta \simeq 1.2^\circ$, and those around temperature hot spots show the opposite patterns, as predicted.

How significant are these features? Before performing the quantitative χ^2 analysis, we first compare Q_r and U_r using both the $(V + W)/2$ sum map (here, $V + W$ refers to the inverse noise variance weighted average) as well as the $(V - W)/2$ difference map (bottom panels of Figures 5 and 6). The Q_r map (which is expected to be non-zero for a cosmological signal) shows clear differences between the sum and difference maps, while the U_r map (which is expected to vanish in a parity-conserving

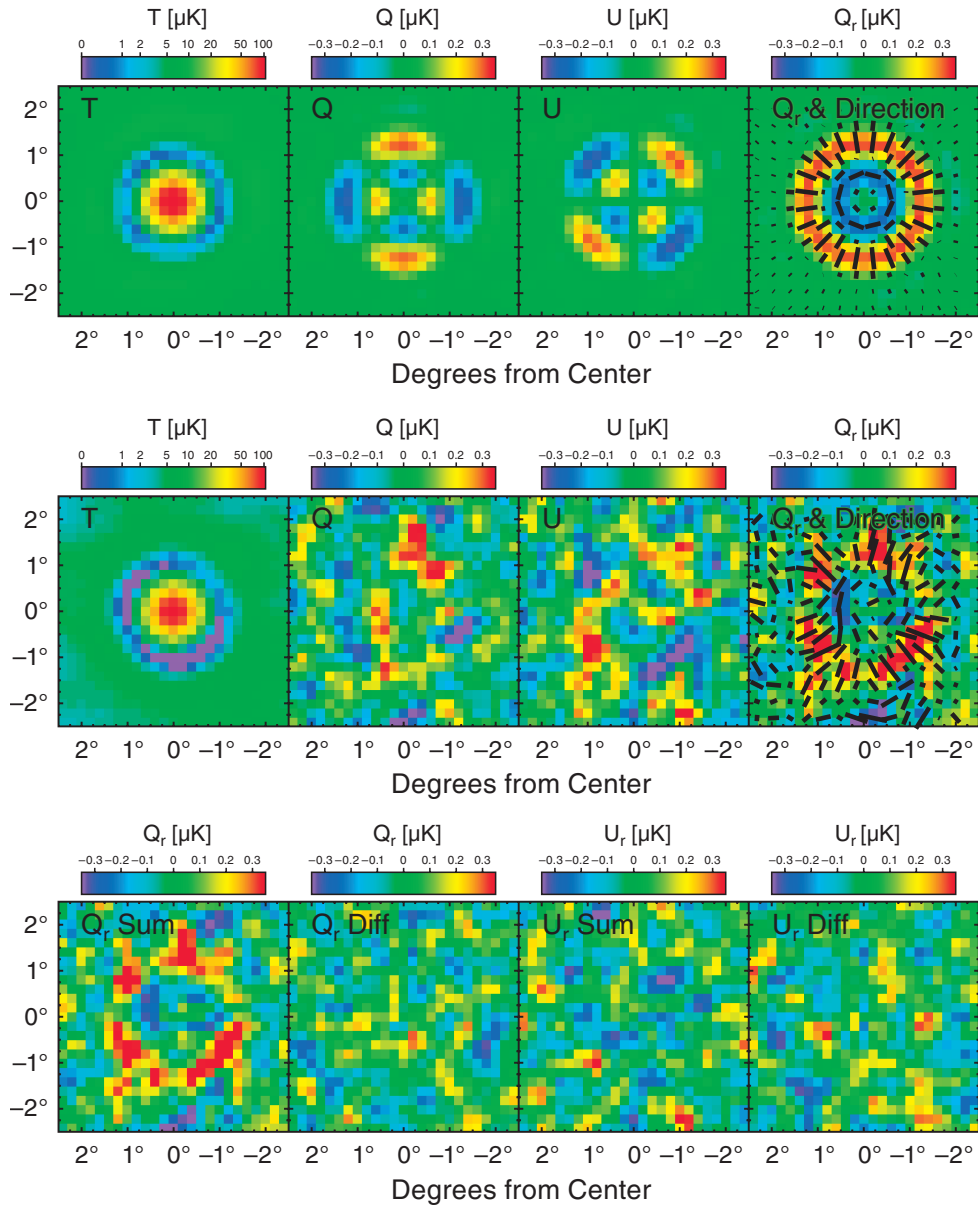


Figure 6. Same as Figure 5 but for temperature hot spots.

universe unless some systematic error rotates the polarization plane uniformly) is consistent with zero in both the sum and difference maps.

Next, we perform the standard χ^2 analysis. We summarize the results in Table 5. We report the values of χ^2 measured with respect to zero signal in the second column, where the number of degrees of freedom (dof) is 625. For each sum map combination, we fit the data to the predicted signal to find the best-fitting amplitude.

The largest improvement in χ^2 is observed for Q_r , as expected from the visual inspection of Figures 5 and 6: we find 0.82 ± 0.15 and 0.90 ± 0.15 for the stacking of Q_r around hot and cold spots, respectively. The improvement in χ^2 is $\Delta\chi^2 = -29.2$ and -36.2 , respectively; thus, we detect the expected polarization patterns around hot and cold spots at the level of 5.4σ and 6σ , respectively. The combined significance exceeds 8σ .

On the other hand, we do not find any evidence for U_r . The χ^2 values with respect to zero signal per dof are $629.2/625$ (hot spots) and $657.8/625$ (cold spots), and the probabilities of

finding larger values of χ^2 are 44.5% and 18%, respectively. But, can we learn anything about cosmology from this result? While the standard model predicts $C_l^{\text{TB}} = 0$ and hence $\langle U_r \rangle = 0$, models in which the global parity symmetry is violated can create $C_l^{\text{TB}} = \sin(2\Delta\alpha)C_l^{\text{TE}}$ (Lue et al. 1999; Carroll 1998; Feng et al. 2005). Therefore, we fit the measured U_r to the predicted Q_r , finding a null result: $\sin(2\Delta\alpha) = -0.13 \pm 0.15$ and 0.20 ± 0.15 (68% CL), or equivalently $\Delta\alpha = -3.7^\circ \pm 4.3^\circ$ and $5.7^\circ \pm 4.3^\circ$ (68% CL) for hot and cold spots, respectively. Averaging these numbers, we obtain $\Delta\alpha = 1.0^\circ \pm 3.0^\circ$ (68% CL), which is consistent with (although not as stringent as) the limit we find from the full analysis presented in Section 4.5. Finally, all the χ^2 values measured from the difference maps are consistent with a null signal.

How do these results compare to the full analysis of the TE power spectrum? By fitting the seven-year C_l^{TE} data to the same power spectrum used above (five-year best-fitting power-law ΛCDM model from $l = 24$ to 800, i.e., dof=777), we find the best-fitting amplitude of 0.999 ± 0.048 and $\Delta\chi^2 = -434.5$,

Table 5
Statistics of the Results from the Stacked Polarization Analysis

Data Combination ^a	χ^2 ^b	Best-fitting Amplitude ^c	$\Delta\chi^2$ ^d
Hot, Q , V + W	661.9	0.57 ± 0.21	-7.3
Hot, U , V + W	661.1	1.07 ± 0.21	-24.7
Hot, Q_r , V + W	694.2	0.82 ± 0.15	-29.2
Hot, U_r , V + W	629.2	-0.13 ± 0.15	-0.18
Cold, Q , V + W	668.3	0.89 ± 0.21	-18.2
Cold, U , V + W	682.7	0.86 ± 0.21	-16.7
Cold, Q_r , V + W	682.2	0.90 ± 0.15	-36.2
Cold, U_r , V + W	657.8	0.20 ± 0.15	-0.46
Hot, Q , V - W	559.8		
Hot, U , V - W	629.8		
Hot, Q_r , V - W	662.2		
Hot, U_r , V - W	567.0		
Cold, Q , V - W	584.0		
Cold, U , V - W	668.2		
Cold, Q_r , V - W	616.0		
Cold, U_r , V - W	636.9		

Notes.

^a “Hot” and “Cold” denote the stacking around temperature hot spots and cold spots, respectively.

^b Computed with respect to zero signal. The number of degrees of freedom is $25^2 = 625$.

^c Best-fitting amplitudes for the corresponding theoretical predictions. The quoted errors show the 68% confidence level. Note that, for U_r , we used the prediction for Q_r ; thus, the fitted amplitude may be interpreted as $\sin(2\Delta\alpha)$, where $\Delta\alpha$ is the rotation of the polarization plane due to, e.g., violation of global parity symmetry.

^d Difference between the second column and χ^2 after removing the model with the best-fitting amplitude given in the third column.

i.e., a 21σ detection of the TE signal. This is reasonable, as we used only the V- and W-band data for the stacking analysis, while we used also the Q-band data for measuring the TE power spectrum; $\langle Q_r \rangle(\theta)$ is insensitive to information on $\theta \gtrsim 2^\circ$ (see top left panel of Figure 3); and the smoothing suppresses the power at $l \gtrsim 400$ (see left panel of Figure 2). Nevertheless, there is probably a way to extract more information from $\langle Q_r \rangle(\theta)$ by, for example, combining data at different threshold peak heights and smoothing scales.

2.5. Discussion

If the temperature fluctuations of the CMB obey Gaussian statistics and global parity symmetry is respected on cosmological scales, the temperature-E-mode polarization cross power spectrum, C_l^{TE} , contains all the information about the temperature-polarization correlation. In this sense, the stacked polarization images do not add any new information.

The detection and measurement of the temperature-E mode polarization cross-correlation power spectrum, C_l^{TE} (Kovac et al. 2002; Kogut et al. 2003; Spergel et al. 2003), can be regarded as equivalent to finding the predicted polarization patterns around hot and cold spots. While we have shown that one can write the stacked polarization profile around temperature spots in terms of an integral of C_l^{TE} , the formal equivalence between this new method and C_l^{TE} is valid only when temperature fluctuations obey Gaussian statistics, as the stacked Q and U maps measure correlations between temperature peaks and polarization. So far there is no convincing evidence for non-Gaussianity in the temperature fluctuations observed by WMAP (Komatsu et al. 2003, see Section 6 for the seven-year limits on primordial non-

Gaussianity, and Bennett et al. 2011 for discussion on other non-Gaussian features).

Nevertheless, they provide striking confirmation of our understanding of the physics at the decoupling epoch in the form of radial and tangential polarization patterns at two characteristic angular scales that are important for the physics of acoustic oscillation: the compression phase at $\theta = 2\theta_A$ and the reversal phase at $\theta = \theta_A$.

Also, this analysis does not require any analysis in harmonic space, nor decomposition to E and B modes. The analysis is so straightforward and intuitive that the method presented here would also be useful for null tests and systematic error checks. The stacked image of U_r should be particularly useful for systematic error checks.

Any experiments that measure both temperature and polarization should be able to produce the stacked images such as presented in Figures 5 and 6.

3. SUMMARY OF SEVEN-YEAR PARAMETER ESTIMATION

3.1. Improvements from the Five-year Analysis

Foreground mask. The seven-year temperature analysis masks, KQ85y7 and KQ75y7, have been slightly enlarged to mask the regions that have excess foreground emission, particularly in the H II regions Gum and Ophiuchus, identified in the difference between foreground-reduced maps at different frequencies. As a result, the new KQ85y7 and KQ75y7 masks eliminate an additional 3.4% and 1.0% of the sky, leaving 78.27% and 70.61% of the sky for the cosmological analyses, respectively. See Section 2.1 of Gold et al. (2011) for details. There is no change in the polarization P06 mask (see Section 4.2 of Page et al. 2007, for definition of this mask), which leaves 73.28% of the sky.

Point sources and the SZ effect. We continue to marginalize over a contribution from unresolved point sources, assuming that the antenna temperature of point sources declines with frequency as $\nu^{-2.09}$ (see Equation (5) of Nolta et al. 2009). The five-year estimate of the power spectrum from unresolved point sources in Q band in units of antenna temperature, A_{ps} , was $10^3 A_{\text{ps}} = 11 \pm 1 \mu\text{K}^2\text{sr}$ (Nolta et al. 2009), and we used this value and the error bar to marginalize over the power spectrum of residual point sources in the seven-year parameter estimation. The subsequent analysis showed that the seven-year estimate of the power spectrum is $10^3 A_{\text{ps}} = 9.0 \pm 0.7 \mu\text{K}^2\text{sr}$ (Larson et al. 2011), which is somewhat lower than the five-year value because more sources are resolved by WMAP and included in the source mask. The difference in the diffuse mask (between KQ85y5 and KQ85y7) does not affect the value of A_{ps} very much: we find 9.3 instead of 9.0 if we use the five-year diffuse mask and the seven-year source mask. The source power spectrum is sub-dominant in the total power. We have checked that the parameter results are insensitive to the difference between the five-year and seven-year residual source estimates.

We continue to marginalize over a contribution from the SZ effect using the same template as for the 3- and five-year analyses (Komatsu & Seljak 2002). We assume a uniform prior on the amplitude of this template as $0 < A_{\text{SZ}} < 2$, which is now justified by the latest limits from the SPT collaboration, $A_{\text{SZ}} = 0.37 \pm 0.17$ (68% CL; Lueker et al. 2010), and the ACT Collaboration, $A_{\text{SZ}} < 1.63$ (95% CL; Fowler et al. 2010).

High- l temperature and polarization. We increase the multipole range of the power spectra used for the cosmological

parameter estimation from 2–1000 to 2–1200 for the TT power spectrum, and from 2–450 to 2–800 for the TE power spectrum. We use the seven-year V- and W-band maps (Jarosik et al. 2011) to measure the high- l TT power spectrum in $l = 33$ –1200. While we used only Q- and V-band maps to measure the high- l TE and TB power spectra for the five-year analysis (Nolta et al. 2009), we also include W-band maps in the seven-year high- l polarization analysis.

With these data, we now detect the high- l TE power spectrum at 21σ , compared to 13σ for the five-year high- l TE data. This is a consequence of adding two more years of data and the W-band data. The TB data can be used to probe a rotation angle of the polarization plane, $\Delta\alpha$, due to potential parity-violating effects or systematic effects. With the seven-year high- l TB data we find a limit $\Delta\alpha = -0.9 \pm 1.4$ (68% CL). For comparison, the limit from the five-year high- l TB power spectrum was $\Delta\alpha = -1.2 \pm 2.2$ (68% CL; Komatsu et al. 2009a). See Section 4.5 for the seven-year limit on $\Delta\alpha$ from the full analysis.

Low- l temperature and polarization. Except for using the seven-year maps and the new temperature KQ85y7 mask, there is no change in the analysis of the low- l temperature and polarization data: we use the internal linear combination map (Gold et al. 2011) to measure the low- l TT power spectrum in $l = 2$ –32, and calculate the likelihood using the Gibbs sampling and Blackwell–Rao (BR) estimator (Jewell et al. 2004; Wandelt 2003; Wandelt et al. 2004; O’Dwyer et al. 2004; Eriksen et al. 2004, 2007a, 2007b; Chu et al. 2005; Larson et al. 2007). For the implementation of the BR estimator in the five-year analysis, see Section 2.1 of Dunkley et al. (2009). We use Ka-, Q-, and V-band maps for the low- l polarization analysis in $l = 2$ –23, and evaluate the likelihood directly in pixel space as described in Appendix D of Page et al. (2007).

To get a feel for improvements in the low- l polarization data with two additional years of integration, we note that the seven-year limits on the optical depth, and the tensor-to-scalar ratio and rotation angle from the low- l polarization data *alone*, are $\tau = 0.088 \pm 0.015$ (68% CL; see Larson et al. 2011), $r < 1.6$ (95% CL; see Section 4.1), and $\Delta\alpha = -3.8 \pm 5.2$ (68% CL; see Section 4.5), respectively. The corresponding five-year limits were $\tau = 0.087 \pm 0.017$ (Dunkley et al. 2009), $r < 2.7$ (see Section 4.1), and $\Delta\alpha = -7.5 \pm 7.3$ (Komatsu et al. 2009a), respectively.

In Table 6, we summarize the improvements from the five-year data mentioned above.

3.2. External Data Sets

The *WMAP* data are statistically powerful enough to constrain six parameters of a flat Λ CDM model with a tilted spectrum. However, to constrain deviations from this minimal model, other CMB data probing smaller angular scales and astrophysical data probing the expansion rates, distances, and growth of structure are useful.

3.2.1. Small-scale CMB Data

The best limits on the primordial helium abundance, Y_p , are obtained when the *WMAP* data are combined with the power spectrum data from other CMB experiments probing smaller angular scales, $l \gtrsim 1000$.

We use the temperature power spectra from the Arcminute Cosmology Bolometer Array Receiver (ACBAR; Reichardt et al. 2009) and QUEST at DASI (QUaD) (Brown et al. 2009) experiments. For the former, we use the temperature power

Table 6
Polarization Data: Improvements from the Five-year data

l Range	Type	Seven Year	Five Year
High l^a	TE	Detected at 21σ	Detected at 13σ
	TB	$\Delta\alpha = -0.9 \pm 1.4$	$\Delta\alpha = -1.2 \pm 2.2$
Low l^b	EE	$\tau = 0.088 \pm 0.015$	$\tau = 0.087 \pm 0.017$
	BB	$r < 2.1$ (95% CL)	$r < 4.7$ (95% CL)
	EE/BB	$r < 1.6$ (95% CL)	$r < 2.7$ (95% CL)
	TB/EB	$\Delta\alpha = -3.8 \pm 5.2$	$\Delta\alpha = -7.5 \pm 7.3$
All l	TE/EE/BB	$r < 0.93$ (95% CL)	$r < 1.6$ (95% CL)
	TB/EB ^c	$\Delta\alpha = -1.1 \pm 1.4$	$\Delta\alpha = -1.7 \pm 2.1$

Notes.

^a $l \geq 24$. The Q-, V-, and W-band data are used for the seven-year analysis, whereas only the Q- and V-band data were used for the five-year analysis.

^b $2 \leq l \leq 23$. The Ka-, Q-, and V-band data are used for both the seven-year and five-year analyses.

^c The quoted errors are statistical only and do not include the systematic error ± 1.5 (see Section 4.5).

spectrum binned in 16 band powers in the multipole range $900 < l < 2000$. For the latter, we use the temperature power spectrum binned in 13 band powers in $900 < l < 2000$.

We marginalize over the beam and calibration errors of each experiment: for ACBAR, the beam error is 2.6% on a 5 arcmin (FWHM) Gaussian beam and the calibration error is 2.05% in temperature. For QUaD, the beam error combines a 2.5% error on 5.2 and 3.8 arcmin (FWHM) Gaussian beams at 100 GHz and 150 GHz, respectively, with an additional term accounting for the sidelobe uncertainty (see Appendix A of Brown et al. 2009, for details). The calibration error is 3.4% in temperature.

The ACBAR data are calibrated to the *WMAP* five-year temperature data, and the QUaD data are calibrated to the BOOMERanG data (Masi et al. 2006) which are, in turn, calibrated to the *WMAP* 1-year temperature data. (The QUaD team takes into account the change in the calibration from the 1-year to the five-year *WMAP* data.) The calibration errors quoted above are much greater than the calibration uncertainty of the *WMAP* five-year data (0.2%; Hinshaw et al. 2007). This is due to the noise of the ACBAR, QUaD, and BOOMERanG data. In other words, the above calibration errors are dominated by the statistical errors that are uncorrelated with the *WMAP* data. We thus treat the *WMAP*, ACBAR, and QUaD data as independent.

Figure 7 shows the *WMAP* seven-year temperature power spectrum (Larson et al. 2011) as well as the temperature power spectra from ACBAR and QUaD.

We do not use the other, previous small-scale CMB data, as their statistical errors are much larger than those of ACBAR and QUaD, and thus adding them would not improve the constraints on the cosmological parameters significantly. The new power-spectrum data from the SPT (Lueker et al. 2010) and ACT (Fowler et al. 2010) Collaborations were not yet available at the time of our analysis.

3.2.2. Hubble Constant and Angular Diameter Distances

There are two main astrophysical priors that we shall use in this paper: the Hubble constant and the angular diameter distances out to $z = 0.2$ and 0.35.

1. A Gaussian prior on the present-day Hubble constant, $H_0 = 74.2 \pm 3.6 \text{ km s}^{-1} \text{ Mpc}^{-1}$ (68% CL; Riess et al. 2009). The quoted error includes both statistical and systematic errors. This measurement of H_0 is obtained from

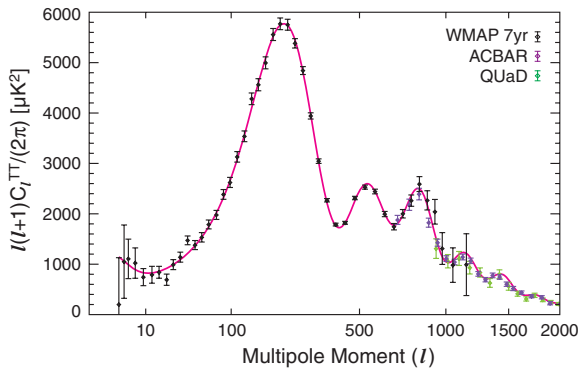


Figure 7. *WMAP* seven-year temperature power spectrum (Larson et al. 2011), along with the temperature power spectra from the ACBAR (Reichardt et al. 2009) and QUAO (Brown et al. 2009) experiments. We show the ACBAR and QUAO data only at $l \geq 690$, where the errors in the *WMAP* power spectrum are dominated by noise. We do not use the power spectrum at $l > 2000$ because of a potential contribution from the SZ effect and point sources. The solid line shows the best-fitting six-parameter flat Λ CDM model to the *WMAP* data alone (see the third column of Table 1 for the maximum likelihood parameters).

the magnitude–redshift relation of 240 low- z Type Ia supernovae at $z < 0.1$. The absolute magnitudes of supernovae are calibrated using new observations from *Hubble Space Telescope* (*HST*) of 240 Cepheid variables in six local Type Ia supernovae host galaxies and the maser galaxy NGC 4258. The systematic error is minimized by calibrating supernova luminosities directly using the geometric maser distance measurements. This is a significant improvement over the prior that we adopted for the five-year analysis, $H_0 = 72 \pm 8 \text{ km s}^{-1} \text{ Mpc}^{-1}$, which is from the Hubble Key Project final results (Freedman et al. 2001).

2. Gaussian priors on the distance ratios, $r_s/D_V(z = 0.2) = 0.1905 \pm 0.0061$ and $r_s/D_V(z = 0.35) = 0.1097 \pm 0.0036$, measured from the Two-Degree Field Galaxy Redshift Survey (2dFGRS) and the Sloan Digital Sky Survey Data Release 7 (SDSS DR7; Percival et al. 2010). The inverse covariance matrix is given by Equation (5) of Percival et al. (2010). These priors are improvements from those we adopted for the five-year analysis, $r_s/D_V(z = 0.2) = 0.1980 \pm 0.0058$ and $r_s/D_V(z = 0.35) = 0.1094 \pm 0.0033$ (Percival et al. 2007).

The above measurements can be translated into a measurement of $r_s/D_V(z)$ at a single, “pivot” redshift: $r_s/D_V(z = 0.275) = 0.1390 \pm 0.0037$ (Percival et al. 2010). Kazin et al. (2010) used the two-point correlation function of SDSS-DR7 LRGs to measure $r_s/D_V(z)$ at $z = 0.278$. They found $r_s/D_V(z = 0.278) = 0.1394 \pm 0.0049$, which is an excellent agreement with the above measurement by Percival et al. (2010) at a similar redshift. The excellent agreement between these two independent studies, which are based on very different methods, indicates that the systematic error in the derived values of $r_s/D_V(z)$ may be much smaller than the statistical error.

Here, r_s is the comoving sound horizon size at the baryon drag epoch z_d ,

$$r_s(z_d) = \frac{c}{\sqrt{3}} \int_0^{1/(1+z_d)} \frac{da}{a^2 H(a) \sqrt{1 + (3\Omega_b/4\Omega_\gamma)a}}. \quad (15)$$

For z_d , we use the fitting formula proposed by Eisenstein & Hu (1998). The effective distance measure, $D_V(z)$

(Eisenstein et al. 2005), is given by

$$D_V(z) \equiv \left[(1+z)^2 D_A^2(z) \frac{cz}{H(z)} \right]^{1/3}, \quad (16)$$

where $D_A(z)$ is the proper (not comoving) angular diameter distance:

$$D_A(z) = \frac{c}{H_0} \frac{f_k \left[H_0 \sqrt{|\Omega_k|} \int_0^z \frac{dz'}{H(z')} \right]}{(1+z) \sqrt{|\Omega_k|}}, \quad (17)$$

where $f_k[x] = \sin x$, x , and $\sinh x$ for $\Omega_k < 0$ ($k = 1$; positively curved), $\Omega_k = 0$ ($k = 0$; flat), and $\Omega_k > 0$ ($k = -1$; negatively curved), respectively. The Hubble expansion rate, which has contributions from baryons, cold dark matter, photons, massless and massive neutrinos, curvature, and dark energy, is given by Equation (27) in Section 3.3.

The cosmological parameters determined by combining the *WMAP* data, baryon acoustic oscillation (BAO), and H_0 will be called “*WMAP+BAO+H₀*,” and they constitute our best estimates of the cosmological parameters, unless noted otherwise.

Note that, when redshift is much less than unity, the effective distance approaches $D_V(z) \rightarrow cz/H_0$. Therefore, the effect of different cosmological models on $D_V(z)$ does not appear until one goes to higher redshifts. If redshift is very low, $D_V(z)$ is simply measuring the Hubble constant.

3.2.3. Power Spectrum of Luminous Red Galaxies

A combination of the *WMAP* data and the power spectrum of LRGs measured from the SDSS DR7 is a powerful probe of the total mass of neutrinos, $\sum m_\nu$, and the effective number of neutrino species, N_{eff} (Reid et al. 2010b, 2010a). We thus combine the LRG power spectrum (Reid et al. 2010b) with the *WMAP* seven-year data and the Hubble constant (Riess et al. 2009) to update the constraints on $\sum m_\nu$ and N_{eff} reported in Reid et al. (2010b). Note that BAO and the LRG power spectrum cannot be treated as independent data sets because a part of the measurement of BAO used LRGs as well.

3.2.4. Luminosity Distances

The luminosity distances out to high- z Type Ia supernovae have been the most powerful data for first discovering the existence of dark energy (Riess et al. 1998; Perlmutter et al. 1999) and then constraining the properties of dark energy, such as the equation of state parameter, w (see Frieman et al. 2008, for a recent review). With more than 400 Type Ia supernovae discovered, the constraints on the properties of dark energy inferred from Type Ia supernovae are now limited by systematic errors rather than by statistical errors.

There is an indication that the constraints on dark energy parameters are different when different methods are used to fit the light curves of Type Ia supernovae (Hicken et al. 2009a; Kessler et al. 2009). We also found that the parameters of the minimal six-parameter Λ CDM model derived from two compilations of Kessler et al. (2009) are different: one compilation uses the light curve fitter called SALT-II (Guy et al. 2007) while the other uses the light curve fitter called MLCS2K2 (Jha et al. 2007). For example, Ω_Λ derived from *WMAP+BAO+SALT-II* and *WMAP+BAO+MLCS2K2* are different by nearly 2σ , despite being derived from the same data sets (but processed with two different light curve fitters). If we allow the dark energy

equation of state parameter, w , to vary, we find that w derived from *WMAP*+BAO+SALT-II and *WMAP*+BAO+MLCS2K2 are different by $\sim 2.5\sigma$.

At the moment it is not obvious how to estimate systematic errors and properly incorporate them in the likelihood analysis, in order to reconcile different methods and data sets.

In this paper, we shall use one compilation of the supernova data called the “Constitution” samples (Hicken et al. 2009a). The reason for this choice over the others, such as the compilation by Kessler et al. (2009) that includes the latest data from the SDSS-II supernova survey, is that the Constitution samples are an extension of the “Union” samples (Kowalski et al. 2008) that we used for the five-year analysis (see Section 2.3 of Komatsu et al. 2009a). More specifically, the Constitution samples are the Union samples plus the latest samples of nearby Type Ia supernovae optical photometry from the Center for Astrophysics (CfA) supernova group (CfA3 sample; Hicken et al. 2009b). Therefore, the parameter constraints from a combination of the *WMAP* seven-year data, the latest BAO data described above (Percival et al. 2010), and the Constitution supernova data may be directly compared to the “*WMAP*+BAO+SN” parameters given in Tables 1 and 2 of Komatsu et al. (2009a). This is a useful comparison, as it shows how much the limits on parameters have improved by adding two more years of data.

However, given the scatter of results among different compilations of the supernova data, we have decided to choose the “*WMAP*+BAO+ H_0 ” (see Section 3.2.2) as our best data combination to constrain the cosmological parameters, except for dark energy parameters. For dark energy parameters, we compare the results from *WMAP*+BAO+ H_0 and *WMAP*+BAO+SN in Section 5. Note that we always marginalize over the absolute magnitudes of Type Ia supernovae with a uniform prior.

3.2.5. Time-delay Distance

Can we measure angular diameter distances out to higher redshifts? Measurements of gravitational lensing time delays offer a way to determine absolute distance scales (Refsdal 1964). When a foreground galaxy lenses a background variable source (e.g., quasars) and produces multiple images of the source, changes of the source luminosity due to variability appear on multiple images at different times.

The time delay at a given image position $\boldsymbol{\theta}$ for a given source position $\boldsymbol{\beta}$, $t(\boldsymbol{\theta}, \boldsymbol{\beta})$, depends on the angular diameter distances as (see, e.g., Schneider et al. 2006, for a review)

$$t(\boldsymbol{\theta}, \boldsymbol{\beta}) = \frac{1+z_l}{c} \frac{D_l D_s}{D_{ls}} \phi_F(\boldsymbol{\theta}, \boldsymbol{\beta}), \quad (18)$$

where D_l , D_s , and D_{ls} are the angular diameter distances out to a lens galaxy, to a source galaxy, and between them, respectively, and ϕ_F is the so-called Fermat potential, which depends on the path length of light rays and gravitational potential of the lens galaxy.

The biggest challenge for this method is to control systematic errors in our knowledge of ϕ_F , which requires a detailed modeling of mass distribution of the lens. One can, in principle, minimize this systematic error by finding a lens system where the mass distribution of lens is relatively simple.

The lens system B1608+656 is not a simple system, with two lens galaxies and dust extinction; however, it has one of the most precise time-delay measurements of quadruple lenses. The lens redshift of this system is relatively large, $z_l = 0.6304$ (Myers et al. 1995). The source redshift is $z_s = 1.394$ (Fassnacht

et al. 1996). This system has been used to determine H_0 to 10% accuracy (Koopmans et al. 2003).

Suyu et al. (2009) have obtained more data from the deep *HST* Advanced Camera for Surveys (ACS) observations of the asymmetric and spatially extended lensed images, and constrained the slope of mass distribution of the lens galaxies. They also obtained ancillary data (for stellar dynamics and lens environment studies) to control the systematics, particularly the so-called “mass-sheet degeneracy,” which the strong lensing data alone cannot break. By doing so, they were able to reduce the error in H_0 (including the systematic error) by a factor of two (Suyu et al. 2010). They find a constraint on the “time-delay distance,” $D_{\Delta t}$, as

$$D_{\Delta t} \equiv (1+z_l) \frac{D_l D_s}{D_{ls}} \simeq 5226 \pm 206 \text{ Mpc}, \quad (19)$$

where the number is found from a Gaussian fit to the likelihood of $D_{\Delta t}$ ¹⁶, however, the actual shape of the likelihood is slightly non-Gaussian. We thus use

1. Likelihood of $D_{\Delta t}$ out to the lens system B1608+656 given by Suyu et al. (2010),

$$P(D_{\Delta t}) = \frac{\exp[-(\ln(x - \lambda) - \mu)^2 / (2\sigma^2)]}{\sqrt{2\pi}(x - \lambda)\sigma}, \quad (20)$$

where $x = D_{\Delta t}/(1 \text{ Mpc})$, $\lambda = 4000$, $\mu = 7.053$, and $\sigma = 0.2282$. This likelihood includes systematic errors due to the mass-sheet degeneracy, which dominates the total error budget (see Section 6 of Suyu et al. 2010, for more details). Note that this is the only lens system for which $D_{\Delta t}$ (rather than H_0) has been constrained.¹⁷

3.3. Treating Massive Neutrinos in $H(a)$ Exactly

When we evaluate the likelihood of external astrophysical data sets, we often need to compute the Hubble expansion rate, $H(a)$. While we treated the effect of massive neutrinos on $H(a)$ approximately for the five-year analysis of the external data sets presented in Komatsu et al. (2009a), we treat it exactly for the seven-year analysis, as described below.

The total energy density of massive neutrino species, ρ_ν , is given by (in natural units)

$$\rho_\nu(a) = 2 \int \frac{d^3 p}{(2\pi)^3} \frac{1}{e^{p/T_\nu(a)} + 1} \sum_i \sqrt{p^2 + m_{v,i}^2}, \quad (21)$$

¹⁶ S. H. Suyu (2009, private communication).

¹⁷ As the time-delay distance, $D_{\Delta t}$, is the angular diameter distance to the lens, D_l , multiplied by the distance ratio, D_s/D_{ls} , the sensitivity of $D_{\Delta t}$ to cosmological parameters is somewhat limited compared to that of D_l (Fukugita et al. 1990). On the other hand, if the density profile of the lens galaxy is approximately given by $\rho \propto 1/r^2$, the observed Einstein radius and velocity dispersion of the lens galaxy can be used to infer the same distance ratio, D_s/D_{ls} , and thus one can use this property to constrain cosmological parameters as well (Futamase & Yoshida 2001; Yamamoto & Futamase 2001; Yamamoto et al. 2001; Ohyama et al. 2002; Dobke et al. 2009), up to uncertainties in the density profile (Chiba & Takahashi 2002). By combining measurements of the time-delay, Einstein ring, and velocity dispersion, one can in principle measure D_l directly, thereby turning strong gravitational lens systems into standard rulers (Paraficz & Hjorth 2009). While the accuracy of the current data for B1608+656 does not permit us to determine D_l precisely yet (S. H. Suyu & P. J. Marshall 2009, private communication), there seems to be exciting future prospects for this method. Future prospects of the time-delay method are also discussed in Oguri (2007) and Coe & Moustakas (2009).

where $m_{\nu,i}$ is the mass of each neutrino species. Using the comoving momentum, $q \equiv pa$, and the present-day neutrino temperature, $T_{v0} = (4/11)^{1/3} T_{\text{cmb}} = 1.945$ K, we write

$$\rho_\nu(a) = \frac{1}{a^4} \int \frac{q^2 dq}{\pi^2} \frac{1}{e^{q/T_{v0}} + 1} \sum_i \sqrt{q^2 + m_{\nu,i}^2 a^2}. \quad (22)$$

Throughout this paper, we shall assume that all massive neutrino species have the equal mass m_ν , i.e., $m_{\nu,i} = m_\nu$ for all i .¹⁸

When neutrinos are relativistic, one may relate ρ_ν to the photon energy density, ρ_γ , as

$$\rho_\nu(a) \rightarrow \frac{7}{8} \left(\frac{4}{11} \right)^{4/3} N_{\text{eff}} \rho_\gamma(a) \simeq 0.2271 N_{\text{eff}} \rho_\gamma(a), \quad (23)$$

where N_{eff} is the effective number of neutrino species. Note that $N_{\text{eff}} = 3.04$ for the standard neutrino species.¹⁹ This motivates our writing (Equation (22)) as

$$\rho_\nu(a) = 0.2271 N_{\text{eff}} \rho_\gamma(a) f(m_\nu a / T_{v0}), \quad (24)$$

where

$$f(y) \equiv \frac{120}{7\pi^4} \int_0^\infty dx \frac{x^2 \sqrt{x^2 + y^2}}{e^x + 1}. \quad (25)$$

The limits of this function are $f(y) \rightarrow 1$ for $y \rightarrow 0$, and $f(y) \rightarrow \frac{180\zeta(3)}{7\pi^4} y$ for $y \rightarrow \infty$, where $\zeta(3) \simeq 1.202$ is the Riemann zeta function. We find that $f(y)$ can be approximated by the following fitting formula:²⁰

$$f(y) \approx [1 + (Ay)^p]^{1/p}, \quad (26)$$

where $A = \frac{180\zeta(3)}{7\pi^4} \simeq 0.3173$ and $p = 1.83$. This fitting formula is constructed such that it reproduces the asymptotic limits in $y \rightarrow 0$ and $y \rightarrow \infty$ exactly. This fitting formula underestimates $f(y)$ by 0.1% at $y \simeq 2.5$ and overestimates by 0.35% at $y \simeq 10$. The errors are smaller than these values at other y 's.

Using this result, we write the Hubble expansion rate as

$$H(a) = H_0 \left\{ \frac{\Omega_c + \Omega_b}{a^3} + \frac{\Omega_\gamma}{a^4} [1 + 0.2271 N_{\text{eff}} f(m_\nu a / T_{v0})] + \frac{\Omega_k}{a^2} + \frac{\Omega_\Lambda}{a^{3(1+w_{\text{eff}}(a))}} \right\}^{1/2}, \quad (27)$$

where $\Omega_\gamma = 2.469 \times 10^{-5} h^{-2}$ for $T_{\text{cmb}} = 2.725$ K. Using the massive neutrino density parameter, $\Omega_\nu h^2 = \sum m_\nu / (94 \text{ eV})$, for the standard three neutrino species, we find

$$\frac{m_\nu a}{T_{v0}} = \frac{187}{1+z} \left(\frac{\Omega_\nu h^2}{10^{-3}} \right). \quad (28)$$

One can check that $(\Omega_\gamma/a^4)0.2271 N_{\text{eff}} f(m_\nu a / T_{v0}) \rightarrow \Omega_\nu/a^3$ for $a \rightarrow \infty$. One may compare Equation (27), which is exact

¹⁸ While the current cosmological data are not yet sensitive to the mass of individual neutrino species, that is, the mass hierarchy, this situation may change in the future, with high- z galaxy redshift surveys or weak lensing surveys (Takada et al. 2006; Slosar 2006; Hannestad & Wong 2007; Kitching et al. 2008; Abdalla & Rawlings 2007).

¹⁹ A recent estimate gives $N_{\text{eff}} = 3.046$ (Mangano et al. 2005).

²⁰ Also see Section 5 of Wright (2006), where ρ_ν is normalized by the density in the non-relativistic limit. Here, ρ_ν is normalized by the density in the relativistic limit. Both results agree with the same precision.

(if we compute $f(y)$ exactly), to Equation (7) of Komatsu et al. (2009a), which is approximate.

Throughout this paper, we shall use Ω_Λ to denote the dark energy density parameter at present: $\Omega_\Lambda \equiv \Omega_{de}(z=0)$. The function $w_{\text{eff}}(a)$ in Equation (28) is the effective equation of state of dark energy given by $w_{\text{eff}}(a) \equiv \frac{1}{\ln a} \int_0^{\ln a} d \ln a' w(a')$, and $w(a)$ is the usual dark energy equation of state, i.e., the dark energy pressure divided by the dark energy density: $w(a) \equiv P_{de}(a)/\rho_{de}(a)$. For vacuum energy (cosmological constant), w does not depend on time, and $w = -1$.

4. COSMOLOGICAL PARAMETERS UPDATE EXCEPT FOR DARK ENERGY

4.1. Primordial Spectral Index and Gravitational Waves

The seven-year *WMAP* data combined with BAO and H_0 exclude the scale-invariant spectrum by 99.5% CL, if we ignore tensor modes (gravitational waves).

For a power-law spectrum of primordial curvature perturbations \mathcal{R}_k , i.e.,

$$\Delta_{\mathcal{R}}^2(k) = \frac{k^3 \langle |\mathcal{R}_k|^2 \rangle}{2\pi^2} = \Delta_{\mathcal{R}}^2(k_0) \left(\frac{k}{k_0} \right)^{n_s - 1}, \quad (29)$$

where $k_0 = 0.002 \text{ Mpc}^{-1}$, we find

$$n_s = 0.968 \pm 0.012 (68\% \text{ CL}).$$

For comparison, the *WMAP* data-only limit is $n_s = 0.967 \pm 0.014$ (Larson et al. 2011), and the *WMAP* plus the small-scale CMB experiments ACBAR (Reichardt et al. 2009) and QUaD (Brown et al. 2009) is $n_s = 0.966^{+0.014}_{-0.013}$. As explained in Section 3.1.2 of Komatsu et al. (2009a), the small-scale CMB data do not reduce the error bar in n_s very much because of relatively large statistical errors, beam errors, and calibration errors.

How about tensor modes? While the B -mode polarization is a smoking gun for tensor modes (Seljak & Zaldarriaga 1997; Kamionkowski et al. 1997b), the *WMAP* data mainly constrain the amplitude of tensor modes by the low- l temperature power spectrum (see Section 3.2.3 of Komatsu et al. 2009a). Nevertheless, it is still useful to see how much constraint one can obtain from the seven-year polarization data.

We first fix the cosmological parameters at the five-year *WMAP* best-fit values of a power-law ΛCDM model. We then calculate the tensor mode contributions to the B -mode, E -mode, and TE power spectra as a function of one parameter: the amplitude, in the form of the tensor-to-scalar ratio, r , defined as

$$r \equiv \frac{\Delta_h^2(k_0)}{\Delta_{\mathcal{R}}^2(k_0)}, \quad (30)$$

where $\Delta_h^2(k)$ is the power spectrum of tensor metric perturbations, h_k , given by

$$\Delta_h^2(k) = \frac{4k^3 \langle |h_k|^2 \rangle}{2\pi^2} = \Delta_h^2(k_0) \left(\frac{k}{k_0} \right)^{n_t}. \quad (31)$$

In Figure 8, we show the limits on r from the B -mode power spectrum only ($r < 2.1$, 95% CL), from the B - and E -mode power spectra combined ($r < 1.6$), and from the B -mode, E -mode, and TE power spectra combined ($r < 0.93$). These limits are significantly better than those from the five-year data ($r < 4.7, 2.7$, and 1.6 , respectively), because of the smaller noise

Table 7
Primordial Tilt n_s , Running Index $dn_s/d \ln k$, and Tensor-to-scalar Ratio r

Section	Model	Parameter ^a	Seven-year WMAP ^b	WMAP+ACBAR+QUaD ^c	WMAP+BAO+ H_0
Section 4.1	Power-law ^d	n_s	0.967 ± 0.014	$0.966^{+0.014}_{-0.013}$	0.968 ± 0.012
Section 4.2	Running	n_s	$1.027^{+0.050}_{-0.051}$	$1.041^{+0.045}_{-0.046}$	1.008 ± 0.042^f
		$dn_s/d \ln k$	-0.034 ± 0.026	$-0.041^{+0.022}_{-0.023}$	-0.022 ± 0.020
Section 4.1	Tensor	n_s	$0.982^{+0.020}_{-0.019}$	$0.979^{+0.018}_{-0.019}$	0.973 ± 0.014
		r	<0.36 (95% CL)	<0.33 (95% CL)	<0.24 (95% CL)
Section 4.2	Running +tensor	n_s	1.076 ± 0.065		1.070 ± 0.060
		r	<0.49 (95% CL)	N/A	<0.49 (95% CL)
		$dn_s/d \ln k$	-0.048 ± 0.029		-0.042 ± 0.024

Notes.

^a Defined at $k_0 = 0.002 \text{ Mpc}^{-1}$.

^b Larson et al. (2011).

^c ACBAR (Reichardt et al. 2009); QUaD (Brown et al. 2009).

^d The parameters in this row are based on RECFAST version 1.5 (see Appendix A), while the parameters in all the other rows are based on RECFAST version 1.4.2.

^e At the pivot point for WMAP only, where n_s and $dn_s/d \ln k$ are uncorrelated, $n_s(k_{\text{pivot}}) = 0.964 \pm 0.014$. The “pivot wavenumber” may be defined in two ways: (1) $k_{\text{pivot}} = 0.0805 \text{ Mpc}^{-1}$ from $n_s(k_{\text{pivot}}) = n_s(k_0) + \frac{1}{2}(dn_s/d \ln k) \ln(k_{\text{pivot}}/k_0)$, or (2) $k_{\text{pivot}} = 0.0125 \text{ Mpc}^{-1}$ from $d \ln \Delta_R^2/d \ln k|_{k=k_{\text{pivot}}} = n_s(k_0) - 1 + (dn_s/d \ln k) \ln(k_{\text{pivot}}/k_0)$.

^f At the pivot point for WMAP+BAO+ H_0 , where n_s and $dn_s/d \ln k$ are uncorrelated, $n_s(k_{\text{pivot}}) = 0.964 \pm 0.013$. The “pivot wavenumber” may be defined in two ways: (1) $k_{\text{pivot}} = 0.106 \text{ Mpc}^{-1}$ from $n_s(k_{\text{pivot}}) = n_s(k_0) + \frac{1}{2}(dn_s/d \ln k) \ln(k_{\text{pivot}}/k_0)$, or (2) $k_{\text{pivot}} = 0.0155 \text{ Mpc}^{-1}$ from $d \ln \Delta_R^2/d \ln k|_{k=k_{\text{pivot}}} = n_s(k_0) - 1 + (dn_s/d \ln k) \ln(k_{\text{pivot}}/k_0)$.

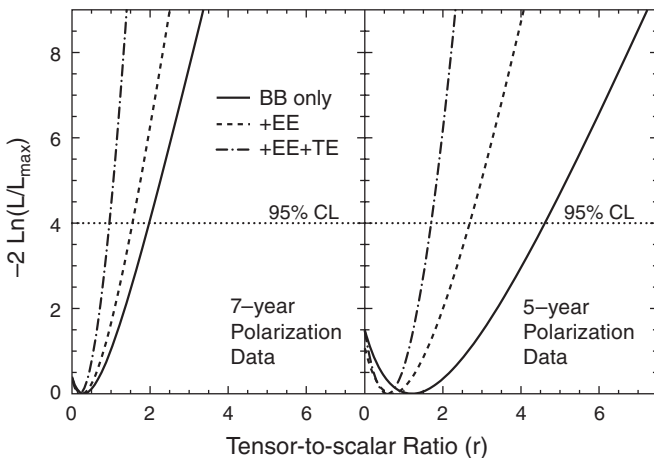


Figure 8. Limits on the tensor-to-scalar ratio, r , from the polarization data (BB, EE and TE) alone. All the other cosmological parameters, including the optical depth, are fixed at the five-year best-fit Λ CDM model (Dunkley et al. 2009). The vertical axis shows $-2 \ln(L/L_{\max})$, where L is the likelihood and L_{\max} is the maximum value. This quantity may be interpreted as the standard χ^2 , as the likelihood is approximately a Gaussian near the maximum; thus, $-2 \ln(L/L_{\max}) = 4$ corresponds to the 95.4% CL limit. The solid, dashed and dot-dashed lines show the likelihood as a function of r from the BB-only, BB+EE, and BB+EE+TE data. Left: the seven-year polarization data. We find $r < 2.1$, 1.6 , and 0.93 (95.4% CL) from the BB-only, BB+EE, and BB+EE+TE data, respectively. Right: the five-year polarization data. We find $r < 4.7$, 2.7 , and 1.6 (95.4% CL) from the BB-only, BB+EE, and BB+EE+TE data, respectively.

and shifts in the best-fitting values. For comparison, the B -mode power spectrum from the BICEP 2-year data gives $r < 0.73$ (95% CL; Chiang et al. 2010).

If we add the temperature power spectrum, but still fix all the other cosmological parameters including n_s , then we find $r < 0.15$ (95% CL) from both five-year and seven-year data; however, due to a strong correlation between n_s and r , this would be an underestimate of the error. For a 7-parameter model (a flat Λ CDM model with a tilted spectrum, tensor modes, and

$n_t = -r/8$), we find $r < 0.36$ (95% CL) from the WMAP data alone (Larson et al. 2011), $r < 0.33$ (95% CL) from WMAP plus ACBAR and QUaD,

$$r < 0.24 \text{ (95% CL)}$$

from WMAP+BAO+ H_0 , and $r < 0.20$ (95% CL) from WMAP+BAO+SN, where “SN” is the Constitution samples compiled by Hicken et al. (2009a; see Section 3.2.4).

We give a summary of these numbers in Table 7.

4.2. Running Spectral Index

Let us relax the assumption that the power spectrum is a pure power law, and add a “running index,” $dn_s/d \ln k$ as (Kosowsky & Turner 1995)

$$\Delta_R^2(k) = \Delta_R^2(k_0) \left(\frac{k}{k_0} \right)^{n_s(k_0) - 1 + \frac{1}{2} \ln(k/k_0) dn_s/d \ln k}. \quad (32)$$

Ignoring tensor modes again, we find

$$dn_s/d \ln k = -0.022 \pm 0.020 \text{ (68% CL)},$$

from WMAP+BAO+ H_0 . For comparison, the WMAP data-only limit is $dn_s/d \ln k = -0.034 \pm 0.026$ (Larson et al. 2011), and the WMAP+ACBAR+QUaD limit is $dn_s/d \ln k = -0.041^{+0.022}_{-0.023}$.

None of these data combinations require $dn_s/d \ln k$: improvements in a goodness-of-fit relative to a power-law model (Equation (29)) are $\Delta\chi^2 = -2 \ln(L_{\text{running}}/L_{\text{power-law}}) = -1.2$, -2.6 , and -0.72 for the WMAP-only, WMAP+ACBAR+QUaD, and WMAP+BAO+ H_0 , respectively. See Table 7 for the case where both r and $dn_s/d \ln k$ are allowed to vary.

A simple power-law primordial power spectrum without tensor modes continues to be an excellent fit to the data. While we have not done a non-parametric study of the shape of the power spectrum, recent studies after the five-year data release continue to show that there is no convincing deviation from a simple power-law spectrum (Peiris & Verde 2010; Ichiki et al. 2010; Hamann et al. 2010).

4.3. Spatial Curvature

While the *WMAP* data alone cannot constrain the spatial curvature parameter of the observable universe, Ω_k , very well, combining the *WMAP* data with other distance indicators such as H_0 , BAO, or supernovae can constrain Ω_k (e.g., Spergel et al. 2007).

Assuming a Λ CDM model ($w = -1$), we find

$$-0.0133 < \Omega_k < 0.0084 \text{ (95% CL)},$$

from *WMAP*+BAO+ H_0 .²¹ However, the limit weakens significantly if dark energy is allowed to be dynamical, $w \neq -1$, as this data combination, *WMAP*+BAO+ H_0 , cannot constrain w very well. We need additional information from Type Ia supernovae to constrain w and Ω_k simultaneously (see Section 5.3 of Komatsu et al. 2009a). We shall explore this possibility in Section 5.

4.4. Non-adiabaticity: Implications for Axions

Non-adiabatic fluctuations are a powerful probe of the origin of matter and the physics of inflation. Following Section 3.6 of Komatsu et al. (2009a), we focus on two physically motivated models for non-adiabatic fluctuations: axion type (Seckel & Turner 1985; Linde 1985, 1991; Turner & Wilczek 1991) and curvaton type (Linde & Mukhanov 1997; Lyth & Wands 2003; Moroi & Takahashi 2001, 2002; Bartolo & Liddle 2002).

For both cases, we consider non-adiabatic fluctuations between photons and cold dark matter:

$$\mathcal{S} = \frac{\delta\rho_c}{\rho_c} - \frac{3\delta\rho_\gamma}{4\rho_\gamma}, \quad (33)$$

and report limits on the ratio of the power spectrum of \mathcal{S} and that of the curvature perturbation \mathcal{R} (e.g., Bean et al. 2006):

$$\frac{\alpha(k_0)}{1 - \alpha(k_0)} = \frac{P_S(k_0)}{P_R(k_0)}, \quad (34)$$

where $k_0 = 0.002 \text{ Mpc}^{-1}$. We denote the limits on axion-type and curvaton-type by α_0 and α_{-1} , respectively.²²

We find no evidence for non-adiabatic fluctuations. The *WMAP* data-only limits are $\alpha_0 < 0.13$ (95% CL) and $\alpha_{-1} < 0.011$ (95% CL; Larson et al. 2011). With *WMAP*+BAO+ H_0 , we find

$$\alpha_0 < 0.077 \text{ (95% CL)} \text{ and } \alpha_{-1} < 0.0047 \text{ (95% CL)},$$

while with *WMAP*+BAO+SN, we find $\alpha_0 < 0.064$ (95% CL) and $\alpha_{-1} < 0.0037$ (95% CL).

The limit on α_0 has an important implication for axion dark matter. In particular, a limit on α_0 is related to a limit on the tensor-to-scalar ratio, r (Kain 2006; Beltran et al. 2007; Sikivie 2008; Kawasaki & Sekiguchi 2008). The explicit formula is

²¹ The 68% CL limit is $\Omega_k = -0.0023^{+0.0054}_{-0.0056}$.

²² The limits on α can also be converted into the numbers showing “how much the adiabatic relation ($\mathcal{S} = 0$) can be violated,” δ_{adi} , which can be calculated from

$$\delta_{\text{adi}} = \frac{\delta\rho_c/\rho_c - 3\delta\rho_\gamma/(4\rho_\gamma)}{\frac{1}{2}[\delta\rho_c/\rho_c + 3\delta\rho_\gamma/(4\rho_\gamma)]} \approx \frac{\sqrt{\alpha}}{3}. \quad (35)$$

for $\alpha \ll 1$ (Komatsu et al. 2009a).

given by Equation (48) of Komatsu et al. (2009a) as²³

$$r = \frac{4.7 \times 10^{-12}}{\theta_a^{10/7}} \left(\frac{\Omega_c h^2}{\gamma} \right)^{12/7} \left(\frac{\Omega_c}{\Omega_a} \right)^{2/7} \frac{\alpha_0}{1 - \alpha_0}, \quad (36)$$

where $\Omega_a \leq \Omega_c$ is the axion density parameter, θ_a is the phase of the Peccei–Quinn field within our observable universe, and $\gamma \leq 1$ is a “dilution factor” representing the amount by which the axion density parameter, $\Omega_a h^2$, would have been diluted due to a potential late-time entropy production by, e.g., decay of some (unspecified) heavy particles, between 200 MeV and the epoch of nucleosynthesis, 1 MeV.

Where does this formula come from? Within the context of the “misalignment” scenario of axion dark matter,²⁴ there are two observables one can use to place limits on the axion properties: the dark matter density and α_0 . They are given by (e.g., Kawasaki & Sekiguchi 2008, and references therein)

$$\frac{\alpha_0(k)}{1 - \alpha_0(k)} = \frac{\Omega_a^2}{\Omega_c^2} \frac{8\epsilon}{\theta_a^2 (f_a/M_{\text{pl}})^2}, \quad (37)$$

$$\Omega_a h^2 = 1.0 \times 10^{-3} \gamma \theta_a^2 \left(\frac{f_a}{10^{10} \text{ GeV}} \right)^{7/6}, \quad (38)$$

where f_a is the axion decay constant, and $\epsilon = -\dot{H}_{\text{inf}}/H_{\text{inf}}^2$ is the so-called slow-roll parameter (where H_{inf} is the Hubble expansion rate during inflation). For single-field inflation models, ϵ is related to r as $r = 16\epsilon$. By eliminating the axion decay constant, one obtains Equation (36).

In deriving the above formula for $\Omega_a h^2$ (Equation (38)), we have assumed that the axion field began to oscillate before the QCD phase transition.²⁵ This is true when $f_a < \mathcal{O}(10^{-2})M_{\text{pl}}$; however, when $f_a > \mathcal{O}(10^{-2})M_{\text{pl}}$, the axions are so light that the axion field would not start oscillating after the QCD phase transition.²⁶ In this limit, the formula for $\Omega_a h^2$ is given by

$$\Omega_a h^2 = 1.6 \times 10^5 \gamma \theta_a^2 \left(\frac{f_a}{10^{17} \text{ GeV}} \right)^{3/2}. \quad (39)$$

²³ This formula assumes that the axion field began to oscillate before the QCD phase transition. The formula in the other limit will be given later. We shall assume that the energy density of the universe was dominated by radiation when the axion field began to oscillate; however, this may not always be true (Kawasaki et al. 1996; Kawasaki & Takahashi 2005) when there was a significant amount of entropy production after the QCD phase transition, i.e., $\gamma \ll 1$.

²⁴ We make the following assumptions: the Peccei–Quinn symmetry was broken during inflation but before the fluctuations we observe today left the horizon, and was not restored before or after the end of inflation (reheating). That the Peccei–Quinn symmetry was not restored before reheating requires the expansion rate during inflation not to exceed the axion decay constant, $H_{\text{inf}} < f_a$ (Lyth & Stewart 1992). That the Peccei–Quinn symmetry was not restored after reheating requires the reheating temperature after inflation not to exceed f_a .

²⁵ Specifically, the temperature at which the axion field began to oscillate, T_1 , can be calculated from the condition $3H(T_1) = m_a(T_1)$, where $m_a(T) \approx 0.1m_{a0}(0.2\text{GeV}/T)^4$ is the mass of axions before the QCD phase transition, $T \gtrsim 0.2\text{GeV}$, and $m_{a0} = 13\text{MeV}(1\text{GeV}/f_a)$ is the mass of axions at the zero temperature. Here, we have used the pion decay constant of $F_\pi = 184\text{MeV}$ to calculate m_{a0} , following Equation (3.4.16) of Weinberg (2008). The Hubble expansion rate during radiation era is given by

$M_{\text{pl}}^2 H^2(T) = (\pi^2/90)g_* T^4$, where $M_{\text{pl}} = 2.4 \times 10^{18} \text{ GeV}$ is the reduced Planck mass and g_* is the number of relativistic degrees of freedom. Before the QCD phase transition, $g_* = 61.75$. After the QCD phase transition but before the electron–positron annihilation, $g_* = 10.75$.

²⁶ This dividing point, $f_a = \mathcal{O}(10^{-2})M_{\text{pl}}$, can be found from the condition $T_1 = 0.2\text{GeV}$ and $3H(T_1) = m_a(T_1)$. See Hertzberg et al. (2008) for more accurate numerical estimate. Note that Hertzberg et al. (2008) used $F_\pi = 93\text{MeV}$ for the pion decay constant when calculating the axion mass at the zero temperature.

By eliminating f_a from Equations (37) and (39), we obtain another formula for r :

$$r = \frac{4.0 \times 10^{-10}}{\theta_a^{2/3}} \left(\frac{\Omega_c h^2}{\gamma} \right)^{4/3} \left(\frac{\Omega_c}{\Omega_a} \right)^{2/3} \frac{\alpha_0}{1 - \alpha_0}. \quad (40)$$

Equations (36) and (40), combined with our limits on $\Omega_c h^2$ and α_0 , imply that the axion dark matter scenario in which axions account for most of the observed amount of dark matter, $\Omega_a \sim \Omega_c$, must satisfy

$$r < \frac{7.6 \times 10^{-15}}{\theta_a^{10/7} \gamma^{12/7}} \quad \text{for } f_a < \mathcal{O}(10^{-2}) M_{\text{pl}}, \quad (41)$$

$$r < \frac{1.5 \times 10^{-12}}{\theta_a^{2/3} \gamma^{4/3}} \quad \text{for } f_a > \mathcal{O}(10^{-2}) M_{\text{pl}}. \quad (42)$$

Alternatively, one can express this constraint as

$$\theta_a \gamma^{6/5} < 3.3 \times 10^{-9} \left(\frac{10^{-2}}{r} \right)^{7/10} \quad \text{for } f_a < \mathcal{O}(10^{-2}) M_{\text{pl}},$$

$$\theta_a \gamma^2 < 1.8 \times 10^{-15} \left(\frac{10^{-2}}{r} \right)^{3/2} \quad \text{for } f_a > \mathcal{O}(10^{-2}) M_{\text{pl}}.$$

Therefore, a future detection of tensor modes at the level of $r = 10^{-2}$ would imply a fine-tuning of θ_a or γ or both of these parameters (Komatsu et al. 2009a). If such fine-tunings are not permitted, axions cannot account for the observed abundance of dark matter (in the misalignment scenario that we have considered here).

Depending on one's interest, one may wish to eliminate the phase, leaving the axion decay constant in the formula (see Equation (B7) of Komatsu et al. 2009a):

$$r = (1.6 \times 10^{-12}) \left(\frac{\Omega_c h^2}{\gamma} \right) \left(\frac{\Omega_c}{\Omega_a} \right) \left(\frac{f_a}{10^{12} \text{GeV}} \right)^{5/6} \frac{\alpha_0}{1 - \alpha_0}, \quad (43)$$

for $f < \mathcal{O}(10^{-2}) M_{\text{pl}}$. This formula gives

$$f_a > 1.8 \times 10^{26} \text{GeV} \gamma^{6/5} \left(\frac{r}{10^{-2}} \right)^{6/5}, \quad (44)$$

which is inconsistent with the condition $f_a < \mathcal{O}(10^{-2}) M_{\text{pl}}$ (unless r is extremely small). The formula that is valid for $f > \mathcal{O}(10^{-2}) M_{\text{pl}}$ is

$$r = (2.2 \times 10^{-8}) \left(\frac{\Omega_c h^2}{\gamma} \right) \left(\frac{\Omega_c}{\Omega_a} \right) \left(\frac{f_a}{10^{17} \text{GeV}} \right)^{1/2} \frac{\alpha_0}{1 - \alpha_0}, \quad (45)$$

which gives

$$f_a > 3.2 \times 10^{32} \text{GeV} \gamma^2 \left(\frac{r}{10^{-2}} \right)^2. \quad (46)$$

Requiring $f_a < M_{\text{pl}} = 2.4 \times 10^{18} \text{GeV}$, we obtain

$$r < \frac{8.7 \times 10^{-10}}{\gamma}. \quad (47)$$

Thus, a future detection of tensor modes at the level of $r = 10^{-2}$ implies a significant amount of entropy production, $\gamma \ll 1$, or a super-Planckian axion decay constant, $f_a \gg M_{\text{pl}}$, or both. Also see Hertzberg et al. (2008), Mack (2009), and Mack & Steinhardt (2009) for similar studies.

For the implications of α_{-1} for curvaton dark matter, see Section 3.6.4 of Komatsu et al. (2009a).

4.5. Parity Violation

While the TB and EB correlations vanish in a parity-conserving universe, they may not vanish when global parity symmetry is broken on cosmological scales (Lue et al. 1999; Carroll 1998). In pixel space, they would show up as a non-vanishing $\langle U_r \rangle$. As we showed already in Section 2.4, the WMAP seven-year $\langle U_r \rangle$ data are consistent with noise. What can we learn from this?

It is now a routine work of CMB experiments to deliver the TB and EB data, and constrain a rotation angle of the polarization plane due to a parity-violating effect (or a rotation due to some systematic error). Specifically, a rotation of the polarization plane by an angle $\Delta\alpha$ gives the following five transformations:

$$C_l^{\text{TE,obs}} = C_l^{\text{TE}} \cos(2\Delta\alpha), \quad (48)$$

$$C_l^{\text{TB,obs}} = C_l^{\text{TE}} \sin(2\Delta\alpha), \quad (49)$$

$$C_l^{\text{EE,obs}} = C_l^{\text{EE}} \cos^2(2\Delta\alpha), \quad (50)$$

$$C_l^{\text{BB,obs}} = C_l^{\text{EE}} \sin^2(2\Delta\alpha), \quad (51)$$

$$C_l^{\text{EB,obs}} = \frac{1}{2} C_l^{\text{EE}} \sin(4\Delta\alpha), \quad (52)$$

where C_l 's on the right-hand side are the primordial power spectra in the absence of rotation, while C_l^{obs} 's on the left-hand side are what we would observe in the presence of rotation.

Note that these equations are not exact but valid only when the primordial B -mode polarization is negligible compared to the E -mode polarization, i.e., $C_l^{\text{BB}} \ll C_l^{\text{EE}}$. For the full expression including C_l^{BB} , see Lue et al. (1999) and Feng et al. (2005).

Roughly speaking, when the polarization data are still dominated by noise rather than by the cosmic signal, the uncertainty in $\Delta\alpha$ is given by a half of the inverse of the signal-to-noise ratio of TE or EE, i.e.,

$$\text{Err}[\Delta\alpha^{\text{TB}}] \simeq \frac{1}{2(S/N)^{\text{TE}}},$$

$$\text{Err}[\Delta\alpha^{\text{EB}}] \simeq \frac{1}{2(S/N)^{\text{EE}}}.$$

(Note that we use the full likelihood code to find the best-fitting values and error bars. These equations should only be used to provide an intuitive feel of how the errors scale with signal-to-noise.) As we mentioned in the last paragraph of Section 2.4, with the seven-year polarization data we detect the TE power spectrum at 21σ from $l = 24$ to 800. We thus expect $\text{Err}[\Delta\alpha^{\text{TB}}] \simeq 1/42 \simeq 0.024 \text{ rad} \simeq 1.4^\circ$, which is significantly better than the five-year value, 2.2° (Komatsu et al. 2009a). On the other hand, we detect the EE power spectrum at $l \geq 24$ only at a few σ level, and thus $\text{Err}[\Delta\alpha^{\text{EB}}] \gg \text{Err}[\Delta\alpha^{\text{TB}}]$, implying that we may ignore the high- l EB data.

The magnitude of polarization rotation angle, $\Delta\alpha$, depends on the path length over which photons experienced a parity-violating interaction. As pointed out by Liu et al. (2006), this leads to the polarization angle that depends on l . We can divide this l -dependence in two regimes: (1) $l \lesssim 20$: the polarization signal was generated during reionization (Zaldarriaga 1997). We are sensitive only to the polarization rotation between the reionization epoch and present epoch. (2) $l \gtrsim 20$: the polarization signal was generated at the decoupling epoch. We are sensitive to the polarization rotation between the decoupling epoch and present epoch; thus, we have the largest path length in this case.

Using the high- l TB data from $l = 24$ to 800, we find $\Delta\alpha = -0.9 \pm 1.4$, which is a significant improvement over the five-year high- l result, $\Delta\alpha = -1.2 \pm 2.2$ (Komatsu et al. 2009a).

Let us turn our attention to lower multipoles, $l \leq 23$. Here, with the seven-year polarization data, the EE power spectrum is detected at 5.1σ , whereas the TE power spectrum is only marginally seen (1.9σ). (The overall significance level of detection of the E -model polarization at $l \leq 23$, including EE and TE, is 5.5σ .) We therefore use both the TB and EB data at $l \leq 23$. We find $\Delta\alpha = -3.8 \pm 5.2$, which is also a good improvement over the five-year low- l value, $\Delta\alpha = -7.5 \pm 7.3$.

Combining the low- l TB/EB and high- l TB data, we find $\Delta\alpha = -1.1 \pm 1.4$ (the five-year combined limit was $\Delta\alpha = -1.7 \pm 2.1$), where the quoted error is purely statistical; however, the *WMAP* instrument can measure the polarization angle to within ± 1.5 of the design orientation (Page et al. 2003, 2007). We thus add 1.5 as an estimate of a potential systematic error. Our final seven-year limit is

$$\Delta\alpha = -1.1 \pm 1.4(\text{stat.}) \pm 1.5(\text{syst.})(68\% \text{ CL}),$$

or $-5.0 < \Delta\alpha < 2.8$ (95% CL), for which we have added the statistical and systematic errors in quadrature (which may be an underestimate of the total error). The statistical error and systematic error are now comparable.

Several research groups have obtained limits on $\Delta\alpha$ from various data sets (Feng et al. 2006; Kostelecký & Mewes 2007; Cabella et al. 2007; Xia et al. 2008a; Xia et al. 2008c; Wu et al. 2009; Gubitosi et al. 2009). Recently, the BOOMERanG Collaboration (Pagano et al. 2009) revisited a limit on $\Delta\alpha$ from their 2003 flight (B2K), taking into account the effect of systematic errors rotating the polarization angle by -0.9 ± 0.7 . By removing this, they find $\Delta\alpha = -4.3 \pm 4.1$ (68% CL). The QUA Collaboration used their final data set to find $\Delta\alpha = 0.64 \pm 0.50(\text{stat.}) \pm 0.50(\text{syst.})$ (68% CL; Brown et al. 2009). Xia et al. (2010) used the BICEP 2-year data (Chiang et al. 2010) to find $\Delta\alpha = -2.6 \pm 1.0$ (68% CL statistical); however, a systematic error of ± 0.7 needs to be added to this error budget (see “Polarization orientation uncertainty” in Table 3 of Takahashi et al. 2010). Therefore, basically the systematic errors in recent measurements of $\Delta\alpha$ from *WMAP* seven-year, QUA final, and BICEP 2-year data are comparable to the statistical errors.

Adding the statistical and systematic errors in quadrature and averaging over *WMAP*, QUA and BICEP with the inverse variance weighting, we find $\Delta\alpha = -0.25 \pm 0.58$ (68% CL), or $-1.41 < \Delta\alpha < 0.91$ (95% CL). We therefore conclude that the microwave background data are comfortably consistent with a parity-conserving universe. See, e.g., Kostelecký & Mewes (2008), Arvanitaki et al. (2010), and references therein for implications of this result for potential violations of Lorentz invariance and CPT symmetry.

4.6. Neutrino Mass

Following Section 6.1 of Komatsu et al. (2009a; also see references therein), we constrain the total mass of neutrinos, $\sum m_\nu = 94 \text{ eV}(\Omega_\nu h^2)$, mainly from the seven-year *WMAP* data combined with the distance information. A new component in the analysis is the exact treatment of massive neutrinos when calculating the likelihood of the BAO data, as described in Section 3.3 (also see Wright 2006).

For a flat Λ CDM model, i.e., $w = -1$ and $\Omega_k = 0$, the *WMAP*-only limit is $\sum m_\nu < 1.3$ eV (95% CL), while the

WMAP+BAO+ H_0 limit is

$$\sum m_\nu < 0.58 \text{ eV} (95\% \text{ CL}) \quad (\text{for } w = -1).$$

The latter is the best upper limit on $\sum m_\nu$ without information on the growth of structure, which is achieved by a better measurement of the early Integrated Sachs–Wolfe (ISW) effect through the third acoustic peak of the seven-year temperature power spectrum (Larson et al. 2011), as well as by a better determination of H_0 from Riess et al. (2009). For explanations of this effect, see Ichikawa et al. (2005) or Section 6.1.3 of Komatsu et al. (2009a).

Sekiguchi et al. (2010) combined the five-year version of *WMAP*+BAO+ H_0 with the small-scale CMB data to find $\sum m_\nu < 0.66$ eV (95% CL). Therefore, the improvement from this value to our seven-year limit, $\sum m_\nu < 0.58$ eV, indeed comes from a better determination of the amplitude of the third acoustic peak in the seven-year temperature data.

The limit improves when information on the growth of structure is added. For example, with *WMAP*+ H_0 and the power spectrum of LRGs (Reid et al. 2010b; see Section 3.2.3) combined, we find $\sum m_\nu < 0.44$ eV (95% CL) for $w = -1$.

The *WMAP*+BAO+ H_0 limit on the neutrino mass weakens significantly to $\sum m_\nu < 1.3$ eV (95% CL) for $w \neq -1$ because we do not use information of Type Ia supernovae here to constrain w . This is driven by w being too negative: there is an anti-correlation between w and $\sum m_\nu$ (Hannestad 2005). The best-fitting value of w in this case is $w = -1.44 \pm 0.27$ (68% CL).²⁷ For *WMAP*+LRG+ H_0 , we find $\sum m_\nu < 0.71$ eV (95% CL) for $w \neq -1$. When the Constitution supernova data are included (*WMAP*+BAO+SN), we find $\sum m_\nu < 0.71$ ²⁸ and 0.91 eV (95% CL) for $w = -1$ and $w \neq -1$, respectively.

Recent studies after the five-year data release combined the *WMAP* five-year data with information on the growth of structure to find various improved limits. Vikhlinin et al. (2009b) added the abundance of X-ray-selected clusters of galaxies, which were found in the *ROSAT* All Sky Survey and followed up by the *Chandra* X-ray Observatory (their cluster catalog is described in Vikhlinin et al. 2009a), to the *WMAP* five-year data, the BAO measurement from Eisenstein et al. (2005), and the Type Ia supernova data from Davis et al. (2007), to find $\sum m_\nu < 0.33$ eV (95% CL) for $w \neq -1$. Mantz et al. (2010b) added a different cluster catalog, also derived from the *ROSAT* All Sky Survey and followed up by the *Chandra* X-ray Observatory (their cluster catalog is described in Mantz et al. 2010a), and the measurement of the gas mass fraction of relaxed clusters (Allen et al. 2008) to the *WMAP* five-year data, the BAO measurement from Percival et al. (2007), and the “Union” Type Ia supernova samples from Kowalski et al. (2008) (all of which constitute the five-year “*WMAP*+BAO+SN” set in Komatsu et al. 2009a), to find $\sum m_\nu < 0.33$ and 0.43 eV (95% CL) for $w = -1$ and $w \neq -1$, respectively.

Reid et al. (2010a) added a prior on the amplitude of matter density fluctuations, $\sigma_8(\Omega_m/0.25)^{0.41} = 0.832 \pm 0.033$ (68% CL; Rozo et al. 2010), which was derived from the abundance of optically selected clusters of galaxies called the

²⁷ That the neutrino mass and w are anti-correlated implies that the neutrino mass limit would improve if we impose a prior on w as $w \geq -1$.

²⁸ The seven-year *WMAP*+BAO+SN limit for $w = -1$ is slightly weaker than the five-year *WMAP*+BAO+SN limit, 0.67 eV. The five-year limit was derived using an approximate treatment of the effect of massive neutrinos on $r_s/D_V(z)$. The seven-year limit we quote here, which uses the exact treatment of massive neutrinos (Section 3.3), is more reliable.

Table 8
Improvements in N_{eff} : Seven Year Versus Five Year

Parameter	Year	WMAP Only	WMAP+BAO+SN+HST	WMAP+BAO+ H_0	WMAP+LRG+ H_0
z_{eq}	5	3141^{+154}_{-157}	3240^{+99}_{-97}	3209^{+85}_{-89}	3240 ± 90
	7	3145^{+140}_{-139}			
$\Omega_m h^2$	5	$0.178^{+0.044}_{-0.041}$	0.160 ± 0.025	0.157 ± 0.016	$0.157^{+0.013}_{-0.014}$
	7	$0.184^{+0.041}_{-0.038}$			
N_{eff}	5	>2.3 (95% CL)	4.4 ± 1.5	$4.34^{+0.86}_{-0.88}$	$4.25^{+0.76}_{-0.80}$
	7	>2.7 (95% CL)			

“maxBCG cluster catalog” (Koester et al. 2007), to the five-year WMAP+BAO+SN, and found $\sum m_v < 0.35$ and 0.52 eV (95% CL) for $w = -1$ and $w \neq -1$, respectively. Thomas et al. (2010) added the angular power spectra of photometrically selected samples of LRGs called “MegaZ” to the five-year WMAP+BAO+SN, and found $\sum m_v < 0.325$ eV (95% CL) for $w = -1$. Wang et al. (2005) pointed out that the limit on $\sum m_v$ from galaxy clusters would improve significantly by not only using the abundance but also the power spectrum of clusters.

In order to exploit the full information contained in the growth of structure, it is essential to understand the effects of massive neutrinos on the nonlinear growth. All of the work to date (including WMAP+LRG+ H_0 presented above) included the effects of massive neutrinos on the *linear* growth, while ignoring their nonlinear effects. The widely used phenomenological calculation of the nonlinear matter power spectrum called the HALOFIT (Smith et al. 2003) has not been calibrated for models with massive neutrinos. Consistent treatments of massive neutrinos in the nonlinear structure formation using cosmological perturbation theory (Saito et al. 2008, 2009; Wong 2008; Lesgourgues et al. 2009; Shoji & Komatsu 2009) and numerical simulations (Brandbyge et al. 2008; Brandbyge & Hannestad 2009) have just begun to be explored. More work along these lines would be necessary to exploit the information on the growth structure to constrain the mass of neutrinos.

4.7. Relativistic Species

How many relativistic species are there in the universe after the matter-radiation equality epoch? We parameterize the relativistic dof using the effective number of neutrino species, N_{eff} , given in Equation (23). This quantity can be written in terms of the matter density, $\Omega_m h^2$, and the redshift of matter-radiation equality, z_{eq} , as (see Equation (84) of Komatsu et al. 2009a)

$$N_{\text{eff}} = 3.04 + 7.44 \left(\frac{\Omega_m h^2}{0.1308} \frac{3139}{1+z_{\text{eq}}} - 1 \right). \quad (53)$$

(Here, $\Omega_m h^2 = 0.1308$ and $z_{\text{eq}} = 3138$ are the five-year maximum likelihood values from the simplest Λ CDM model.) This formula suggests that the variation in N_{eff} is given by

$$\frac{\delta N_{\text{eff}}}{N_{\text{eff}}} \simeq 2.45 \frac{\delta(\Omega_m h^2)}{\Omega_m h^2} - 2.45 \frac{\delta z_{\text{eq}}}{1+z_{\text{eq}}}. \quad (54)$$

The equality redshift is one of the direct observables from the temperature power spectrum. The WMAP data constrain z_{eq} mainly from the ratio of the first peak to the third peak. As the seven-year temperature power spectrum has a better determination of the amplitude of the third peak (Larson et al.

2011), we expect a better limit on z_{eq} compared to the five-year one. For models where N_{eff} is different from 3.04, we find $z_{\text{eq}} = 3145^{+140}_{-139}$ (68% CL) from the WMAP data only,²⁹ which is better than the five-year limit by more than 10% (see Table 8).

However, the fractional error in $\Omega_m h^2$ is much larger, and thus we need to determine $\Omega_m h^2$ using external data. The BAO data provide one constraint. We also find that $\Omega_m h^2$ and H_0 are strongly correlated in the models with $N_{\text{eff}} \neq 3.04$ (see Figure 9). Therefore, an improved measurement of H_0 from Riess et al. (2009) would help reduce the error in $\Omega_m h^2$, thereby reducing the error in N_{eff} . The limit on $\Omega_m h^2$ from the seven-year WMAP+BAO+ H_0 combination is better than the five-year “WMAP+BAO+SN+HST” limit by 36%.

We find that the WMAP+BAO+ H_0 limit on N_{eff} is

$$N_{\text{eff}} = 4.34^{+0.86}_{-0.88} \text{ (68% CL)},$$

while the WMAP+LRG+ H_0 limit is $N_{\text{eff}} = 4.25^{+0.76}_{-0.80}$ (68% CL), which are significantly better than the five-year WMAP+BAO+SN+HST limit, $N_{\text{eff}} = 4.4 \pm 1.5$ (68% CL).

Reid et al. (2010a) added the maxBCG prior, $\sigma_8(\Omega_m/0.25)^{0.41} = 0.832 \pm 0.033$ (68% CL; Rozo et al. 2010), to the five-year WMAP+BAO+SN+HST, and found $N_{\text{eff}} = 3.5 \pm 0.9$ (68% CL). They also added the above prior to the five-year version of WMAP+LRG+ H_0 , finding $N_{\text{eff}} = 3.77 \pm 0.67$ (68% CL).

The constraint on N_{eff} can also be interpreted as an upper bound on the energy density in primordial gravitational waves with frequencies $>10^{-15}$ Hz. Many cosmological mechanisms for the generation of stochastic gravitational waves exist, such as certain inflationary models, electroweak phase transitions, and cosmic strings. At low frequencies (10^{-17} – 10^{-16} Hz), the background is constrained by the limit on tensor fluctuations described in Section 4.1. Constraints at higher frequencies come from pulsar timing measurements at $\sim 10^{-8}$ Hz (Jenet et al. 2006), recent data from the Laser Interferometer Gravitational Wave Observatory (LIGO) at 100 Hz (with limits of $\Omega_{\text{gw}} < 6.9 \times 10^{-6}$ Abbott et al. 2009), and at frequencies $>10^{-10}$ Hz from measurements of light-element abundances. A large gravitational wave energy density at nucleosynthesis would alter the predicted abundances, and observations imply an upper bound of $\Omega_{\text{gw}} h^2 < 7.8 \times 10^{-6}$ (Cyburt et al. 2005).

The CMB provides a limit that reaches down to 10^{-15} Hz, corresponding to the comoving horizon at recombination. The gravitational wave background within the horizon behaves as free-streaming massless particles, so affects the CMB and matter power spectra in the same way as massless neutrinos (Smith et al. 2006). The density contributed by N_{gw} massless neutrino species is $\Omega_{\text{gw}} h^2 = 5.6 \times 10^{-6} N_{\text{gw}}$. Constraints have been found

²⁹ For models with $N_{\text{eff}} = 3.04$, we find $z_{\text{eq}} = 3196^{+134}_{-133}$ (68% CL).

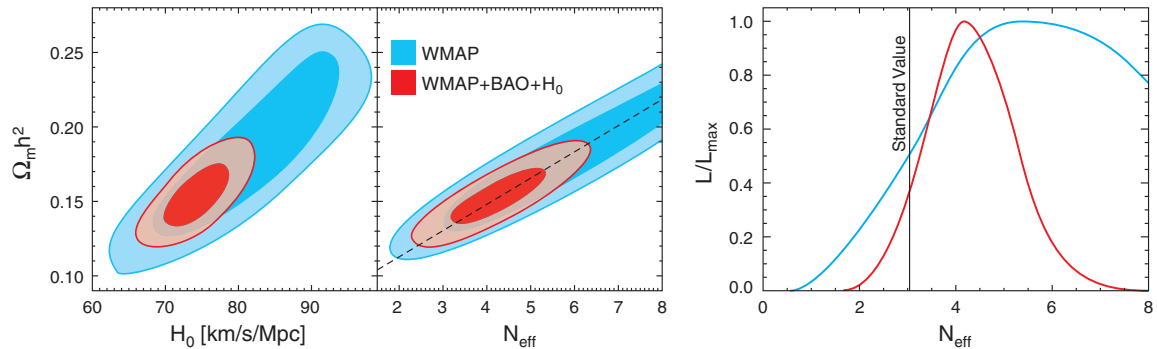


Figure 9. Constraint on the effective number of neutrino species, N_{eff} . Left: joint two-dimensional marginalized distribution (68% and 95% CL), showing how a better determination of H_0 improves a limit on $\Omega_m h^2$. Middle: a correlation between N_{eff} and $\Omega_m h^2$. The dashed line shows the line of correlation given by Equation (53). A better determination of H_0 improves a limit on $\Omega_m h^2$ which, in turn, improves a limit on N_{eff} . Right: one-dimensional marginalized distribution of N_{eff} from WMAP-only and WMAP+BAO+ H_0 . $N_{\text{eff}} = 4.34^{+0.86}_{-0.88}$, is consistent with the standard value, 3.04, which is shown by the vertical line.

using the WMAP three-year data combined with additional cosmological probes by Smith et al. (2006), for both adiabatic and homogeneous initial conditions for the tensor perturbations. With the current WMAP+BAO+ H_0 data combination, we define $N_{\text{gw}} = N_{\text{eff}} - 3.04$, and find limits of

$$N_{\text{gw}} < 2.85, \quad \Omega_{\text{gw}} h^2 < 1.60 \times 10^{-5} \text{ (95% CL)}$$

for adiabatic initial conditions, imposing an $N_{\text{eff}} \geq 3.04$ prior. Adiabatic conditions might be expected if the gravitational waves were generated by the appearance of cusps in cosmic strings (Damour & Vilenkin 2000, 2001; Siemens et al. 2006). For the WMAP+LRG+ H_0 data, we find $N_{\text{gw}} < 2.64$, or $\Omega_{\text{gw}} h^2 < 1.48 \times 10^{-5}$ at 95% CL. Given a particular string model, these bounds can be used to constrain the cosmic string tension (e.g., Siemens et al. 2007; Copeland & Kibble 2009).

4.8. Primordial Helium Abundance

A change in the primordial helium abundance affects the shape of the temperature power spectrum (Hu et al. 1995). The most dominant effect is a suppression of the power spectrum at $l \gtrsim 500$ due to an enhanced Silk damping effect.

For a given mass density of baryons (protons and helium nuclei), the number density of electrons, n_e , can be related to the primordial helium abundance. When both hydrogen and helium were ionized, $n_e = (1 - Y_p/2)\rho_b/m_p$. However, most of the helium recombines by $z \sim 1800$ (see Switzer & Hirata 2008, and references therein), much earlier than the photon decoupling epoch, $z = 1090$. As a result, the number density of free electrons at around the decoupling epoch is given by $n_e = (1 - Y_p)\rho_b/m_p \propto (1 - Y_p)\Omega_b h^2$ (Hu et al. 1995). The larger Y_p is, the smaller n_e becomes. If the number of electrons is reduced, photons can free-stream longer (the mean free path of photons, $1/(\sigma_T n_e)$, gets larger), wiping out more temperature anisotropy. Therefore, a larger Y_p results in a greater suppression of power on small angular scales.

Ichikawa et al. (2008; also see Ichikawa & Takahashi 2006) show that a 100% change in Y_p changes the heights of the second, third, and fourth peaks by $\approx 1\%$, 3% , and 3% , respectively. Therefore, one expects that a combination of the WMAP data and small-scale CMB experiments such as ACBAR (Reichardt et al. 2009) and QUaD (Brown et al. 2009) would be a powerful probe of the primordial helium abundance.

In Figure 10, we compare the WMAP, ACBAR, and QUaD data with the temperature power spectrum with the nominal

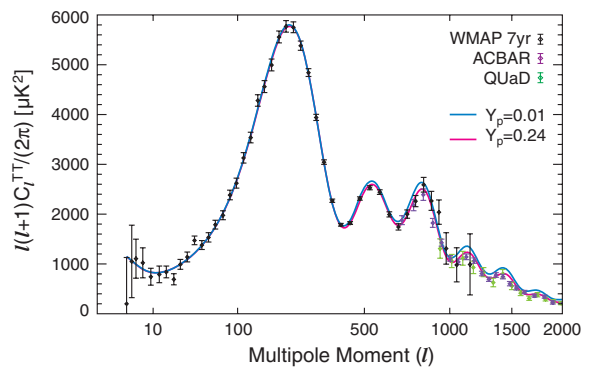


Figure 10. Primordial helium abundance and the temperature power spectrum. The data points are the same as those in Figure 7. The lower (pink) solid line (which is the same as the solid line in Figure 7) shows the power spectrum with the nominal helium abundance, $Y_p = 0.24$, while the upper (blue) solid line shows that with a tiny helium abundance, $Y_p = 0.01$. The larger the helium abundance is, the smaller the number density of electrons during recombination becomes, which enhances the Silk damping of the power spectrum on small angular scales, $l \gtrsim 500$.

value of the primordial helium abundance, $Y_p = 0.24$ (pink line), and that with a tiny amount of helium, $Y_p = 0.01$ (blue line). There is too much power in the case of $Y_p = 0.01$, making it possible to detect the primordial helium effect using the CMB data alone.

However, one must be careful about a potential degeneracy between the effect of helium and those of the other cosmological parameters. First, as the number density of electrons is given by $n_e = (1 - Y_p)n_b \propto (1 - Y_p)\Omega_b h^2$, Y_p and $\Omega_b h^2$ may be correlated. Second, a scale-dependent suppression of power such as this may be correlated with the effect of tilt, n_s (Trotta & Hansen 2004).

In the left panel of Figure 11, we show that $\Omega_b h^2$ and Y_p are essentially uncorrelated: the baryon density is determined by the first-to-second peak ratio relative to the first-to-third peak ratio, which is now well measured by the WMAP data. Therefore, the current WMAP data allow $\Omega_b h^2$ to be measured regardless of Y_p .

In the middle panel of Figure 11, we show that there is a slight positive correlation between n_s and Y_p : an enhanced Silk damping produced by a larger Y_p can be partially canceled by a larger n_s (Trotta & Hansen 2004).

We find a 95% CL upper limit of $Y_p < 0.51$ from the WMAP data alone. When we add the ACBAR and QUaD data, we find a

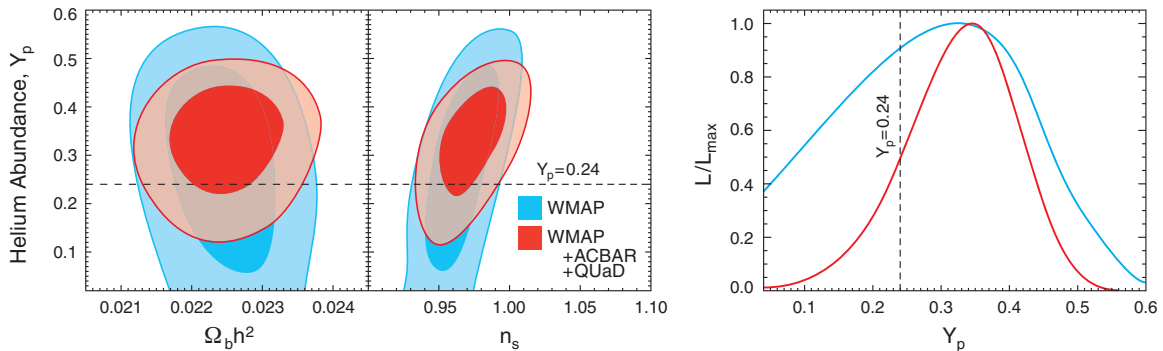


Figure 11. Constraint on the primordial helium abundance, Y_p . Left: joint two-dimensional marginalized distribution (68% and 95% CL), showing that Y_p and $\Omega_b h^2$ are essentially uncorrelated. Middle: a slight correlation exists between Y_p and n_s ; an enhanced Silk damping produced by a larger Y_p can be partially canceled by a larger n_s . Right: one-dimensional marginalized distribution of Y_p from *WMAP*-only and *WMAP*+ACBAR+QUaD. The 68% interval from *WMAP*+ACBAR+QUaD, $Y_p = 0.326 \pm 0.075$ is consistent with the nominal value, 0.24, which is shown by the vertical line.

significant detection of the effect of primordial helium by more than 3σ (see the right panel of Figure 11),

$$Y_p = 0.326 \pm 0.075 \text{ (68% CL)}.$$

The 95% CL limit is $0.16 < Y_p < 0.46$. The 99% CL lower limit is $Y_p > 0.11$. This value is broadly consistent with the helium abundances estimated from observations of low-metallicity extragalactic ionized (H II) regions, $Y_p \simeq 0.24\text{--}0.25$ (Gruenwald et al. 2002; Izotov & Thuan 2004; Olive & Skillman 2004; Fukugita & Kawasaki 2006; Peimbert et al. 2007). See Steigman (2007) for a review.

We can improve this limit by imposing an *upper limit* on Y_p from these astrophysical measurements. As the helium is created by nuclear fusion in stars, the helium abundances measured from stars (e.g., the Sun; see Asplund et al. 2009, for a recent review) and H II regions are, in general, larger than the primordial abundance. On the other hand, as we have just shown, the CMB data provide a *lower limit* on Y_p . Even with a very conservative hard prior, $Y_p < 0.3$, we find $0.23 < Y_p < 0.3$ (68% CL)³⁰. Therefore, a combination of the CMB and the solar constraints on Y_p offers a new way for testing the predictions of theory of the big bang nucleosynthesis (BBN). For example, the BBN predicts that the helium abundance is related to the baryon-to-photon ratio, η , and the number of additional neutrino species (or any other additional relativistic dof) during the BBN epoch, $\Delta N_\nu \equiv N_\nu - 3$, as (see Equation (11) of Steigman 2008)

$$Y_p = 0.2485 + 0.0016[(\eta_{10} - 6) + 100(S - 1)], \quad (55)$$

where $S \equiv \sqrt{1 + (7/43)\Delta N_\nu} \simeq 1 + 0.081\Delta N_\nu$ and $\eta_{10} \equiv 10^{10}\eta = 273.9(\Omega_b h^2) = 6.19 \pm 0.15$ (68% CL; *WMAP*+BAO+ H_0). (See Simha & Steigman 2008, for more discussion on this method.) For $\Delta N_\nu = 1$, the helium abundance changes by $\Delta Y_p = 0.013$, which is much smaller than our error bar, but is comparable to the expected error bar from *Planck* (Ichikawa et al. 2008).

There have been several attempts to measure Y_p from the CMB data (Trotta & Hansen 2004; Huey et al. 2004; Ichikawa & Takahashi 2006; Ichikawa et al. 2008; Dunkley et al. 2009). The previous best-limit is $Y_p = 0.25^{+0.10(+0.15)}_{-0.07(-0.17)}$ at 68% CL

³⁰ The upper limit is set by the hard prior. The 68% lower limit, $Y_{p,\min} = 0.23$, is found such that the integral of the posterior likelihood of Y_p in $Y_{p,\min} \leq Y_p < 0.3$ is 68% of the integral in $0 \leq Y_p < 0.3$. Similarly, the 95% CL lower limit is $Y_p > 0.14$ and the 99% CL lower limit is $Y_p > 0.065$.

(95% CL), which was obtained by Ichikawa et al. (2008) from the *WMAP* five-year data combined with ACBAR (Reichardt et al. 2009), BOOMERanG (Jones et al. 2006; Piacentini et al. 2006; Montroy et al. 2006), and Cosmic Background Imager (CBI; Sievers et al. 2007). Note that the likelihood function of Y_p is non-Gaussian, with a tail extending to $Y_p = 0$; thus, the level of significance of detection was less than 3σ .

5. CONSTRAINTS ON PROPERTIES OF DARK ENERGY

In this section, we provide limits on the properties of dark energy, characterized by the equation of state parameter, w . We first focus on constant (time independent) equation of state in a flat universe (Section 5.1) and a curved universe (Section 5.2). We then constrain a time-dependent w given by $w(a) = w_0 + w_a(1 - a)$, where $a = 1/(1 + z)$ is the scale factor, in Section 5.3. Next, we provide the seven-year “*WMAP* normalization prior” in Section 5.4, which is useful for constraining w (as well as the mass of neutrinos) from the growth of cosmic density fluctuations. (See, e.g., Vikhlinin et al. 2009b, for an application of the five-year normalization prior to the X-ray cluster abundance data.) In Section 5.5, we provide the seven-year “*WMAP* distance prior,” which is useful for constraining a variety of time-dependent w models for which the Markov Chain Monte Carlo exploration of the parameter space may not be available. (See, e.g., Li et al. 2008; Wang 2008, 2009; Vikhlinin et al. 2009b, for applications of the five-year distance prior.)

We give a summary of our limits on dark energy parameters in Table 4.

5.1. Constant Equation of State: Flat Universe

In a flat universe, $\Omega_k = 0$, an accurate determination of H_0 helps improve a limit on a constant equation of state, w (Spergel et al. 2003; Hu 2005). Using *WMAP*+BAO+ H_0 , we find

$$w = -1.10 \pm 0.14 \text{ (68% CL)},$$

which improves to $w = -1.08 \pm 0.13$ (68% CL) if we add the time-delay distance out to the lens system B1608+656 (Suyu et al. 2010, see Section 3.2.5). These limits are independent of high- z Type Ia supernova data.

The high- z supernova data provide the most stringent limit on w . Using *WMAP*+BAO+SN, we find $w = -0.980 \pm 0.053$ (68% CL). The error does not include systematic errors in supernovae, which are comparable to the statistical error

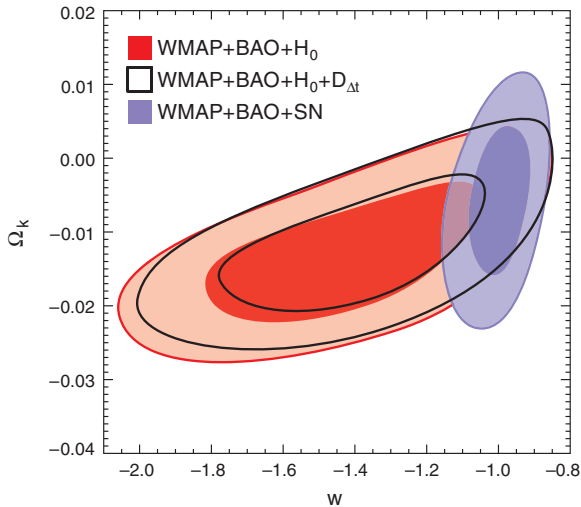


Figure 12. Joint two-dimensional marginalized constraint on the time-independent (constant) dark energy equation of state, w , and the curvature parameter, Ω_k . The contours show the 68% and 95% CL from $WMAP+BAO+H_0$ (red), $WMAP+BAO+H_0+D_{\Delta t}$ (black), and $WMAP+BAO+SN$ (purple).

(Kessler et al. 2009; Hicken et al. 2009a); thus, the error in w from $WMAP+BAO+SN$ is about a half of that from $WMAP+BAO+H_0$ or $WMAP+BAO+H_0+D_{\Delta t}$.

The cluster abundance data are sensitive to w via the co-moving volume element, angular diameter distance, and growth of matter density fluctuations (Haiman et al. 2001). By combining the cluster abundance data and the five-year $WMAP$ data, Vikhlinin et al. (2009b) found $w = -1.08 \pm 0.15(\text{stat}) \pm 0.025(\text{syst})$ (68% CL) for a flat universe. By adding BAO of Eisenstein et al. (2005) and the supernova data of Davis et al. (2007), they found $w = -0.991 \pm 0.045(\text{stat}) \pm 0.039(\text{syst})$ (68% CL). These results using the cluster abundance data (also see Mantz et al. 2010c) agree well with our corresponding $WMAP+BAO+H_0$ and $WMAP+BAO+SN$ limits.

5.2. Constant Equation of State: Curved Universe

When $\Omega_k \neq 0$, limits on w significantly weaken, with a tail extending to large negative values of w , unless supernova data are added.

In Figure 12, we show that $WMAP+BAO+H_0$ allows for $w \lesssim -2$, which can be excluded by adding information on the time-delay distance. In both cases, the spatial curvature is well constrained: we find $\Omega_k = -0.0125^{+0.0064}_{-0.0067}$ from $WMAP+BAO+H_0$, and $-0.0111^{+0.0060}_{-0.0063}$ (68% CL) from $WMAP+BAO+H_0+D_{\Delta t}$, whose errors are comparable to that of the $WMAP+BAO+H_0$ limit on Ω_k with $w = -1$, $\Omega_k = -0.0023^{+0.0054}_{-0.0056}$ (68% CL; see Section 4.3).

However, w is poorly constrained: we find $w = -1.44 \pm 0.27$ from $WMAP+BAO+H_0$, and -1.40 ± 0.25 (68% CL) from $WMAP+BAO+H_0+D_{\Delta t}$.

Among the data combinations that do not use the information on the growth of structure, the most powerful combination for constraining Ω_k and w simultaneously is a combination of the $WMAP$ data, BAO (or $D_{\Delta t}$), and supernovae, as $WMAP+BAO$ (or $D_{\Delta t}$) primarily constrains Ω_k , and $WMAP+SN$ primarily constrains w . With $WMAP+BAO+SN$, we find $w = -0.999^{+0.057}_{-0.056}$ and $\Omega_k = -0.0057^{+0.0066}_{-0.0068}$ (68% CL). Note that the error in the curvature is essentially the same as that from $WMAP+BAO+H_0$, while the error in w is ~ 4 times smaller.

Vikhlinin et al. (2009b) combined their cluster abundance data with the five-year $WMAP+BAO+SN$ to find $w = -1.03 \pm 0.06$ (68% CL) for a curved universe. Reid et al. (2010b) combined their LRG power spectrum with the five-year $WMAP$ data and the Union supernova data to find $w = -0.99 \pm 0.11$ and $\Omega_k = -0.0109 \pm 0.0088$ (68% CL). These results are in good agreement with our seven-year $WMAP+BAO+SN$ limit.

5.3. Time-dependent Equation of State

As for a time-dependent equation of state, we shall find constraints on the present-day value of the equation of state and its derivative using a linear form, $w(a) = w_0 + w_a(1-a)$ (Chevallier & Polarski 2001; Linder 2003). We assume a flat universe, $\Omega_k = 0$. (For recent limits on $w(a)$ with $\Omega_k \neq 0$, see Wang 2009, and references therein.) While we have constrained this model using the $WMAP$ distance prior in the five-year analysis (see Section 5.4.2 of Komatsu et al. 2009a), in the seven-year analysis we shall present the full Markov Chain Monte Carlo exploration of this model.

For a time-dependent equation of state, one must be careful about the treatment of perturbations in dark energy when w crosses -1 . We use the “parameterized post-Friedmann” (PPF) approach, implemented in the CAMB code following Fang et al. (2008).³¹

In Figure 13, we show the seven-year constraints on w_0 and w_a from $WMAP+H_0+SN$ (red), $WMAP+BAO+H_0+SN$ (blue), and $WMAP+BAO+H_0+D_{\Delta t}+SN$ (black). The angular diameter distances measured from BAO and $D_{\Delta t}$ help exclude models with large negative values of w_a . We find that the current data are consistent with a cosmological constant, even when w is allowed to depend on time. However, a large range of values of (w_0, w_a) are still allowed by the data: we find

$$w_0 = -0.93 \pm 0.13 \text{ and } w_a = -0.41^{+0.72}_{-0.71} \text{ (68% CL),}$$

from $WMAP+BAO+H_0+SN$. When the time-delay distance information is added, the limits improve to $w_0 = -0.93 \pm 0.12$ and $w_a = -0.38^{+0.66}_{-0.65}$ (68% CL).

Vikhlinin et al. (2009b) combined their cluster abundance data with the five-year $WMAP+BAO+SN$ to find a limit on a linear combination of the parameters, $w_a + 3.64(1+w_0) = 0.05 \pm 0.17$ (68% CL). Our data combination is sensitive to a different linear combination: we find $w_a + 5.14(1+w_0) = -0.05 \pm 0.32$ (68% CL) for the seven-year $WMAP+BAO+H_0+SN$ combination.

The current data are consistent with a flat universe dominated by a cosmological constant.

5.4. WMAP Normalization Prior

The growth of cosmological density fluctuations is a powerful probe of dark energy, modified gravity, and massive neutrinos. The $WMAP$ data provide a useful normalization of the cosmological perturbation at the decoupling epoch, $z = 1090$. By comparing this normalization with the amplitude of matter density fluctuations in a low redshift universe, one may distinguish between dark energy and modified gravity (Ishak et al. 2006; Koyama & Maartens 2006; Amarzguioui et al. 2006; Doré et al. 2007; Linder & Cahn 2007; Upadhye 2007; Zhang et al. 2007; Yamamoto et al. 2007; Chiba & Takahashi 2007; Bean et al. 2007; Hu & Sawicki 2007; Song et al. 2007; Starobinsky 2007;

³¹ Zhao et al. (2005) used a multi-scalar-field model to treat w crossing -1 . The constraints on w_0 and w_a have been obtained using this model and the previous years of $WMAP$ data (Xia et al. 2006, 2008b; Zhao et al. 2007).

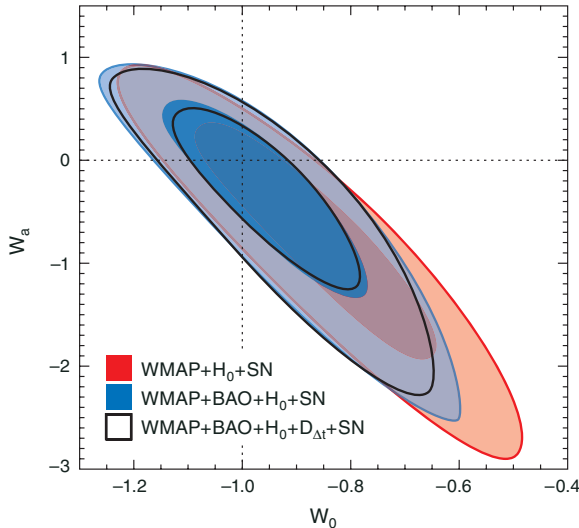


Figure 13. Joint two-dimensional marginalized constraint on the linear evolution model of dark energy equation of state, $w(a) = w_0 + w_a(1 - a)$. The contours show the 68% and 95% CL from $WMAP+H_0+SN$ (red), $WMAP+BAO+H_0+SN$ (blue), and $WMAP+BAO+H_0+D_{\Delta t}+SN$ (black), for a flat universe.

Daniel et al. 2008; Jain & Zhang 2008; Bertschinger & Zukin 2008; Amin et al. 2008; Hu 2008) and determine the mass of neutrinos (Hu et al. 1998; Lesgourgues & Pastor 2006).

In Section 5.5 of Komatsu et al. (2009a), we provided a “*WMAP* normalization prior,” which is a constraint on the power spectrum of curvature perturbation, $\Delta_{\mathcal{R}}^2$. Vikhlinin et al. (2009b) combined this with the number density of clusters of galaxies to constrain the dark energy equation of state, w , and the amplitude of matter density fluctuations, σ_8 .

The matter density fluctuation in Fourier space, $\delta_{m,\mathbf{k}}$, is related to $\mathcal{R}_{\mathbf{k}}$ as $\delta_{m,\mathbf{k}}(z) = \frac{2k^3}{5H_0^2\Omega_m}\mathcal{R}_{\mathbf{k}}T(k)D(k,z)$, where $D(k,z)$ and $T(k)$ are the linear growth rate and the matter transfer function normalized such that $T(k) \rightarrow 1$ as $k \rightarrow 0$, and $(1+z)D(k,z) \rightarrow 1$ as $k \rightarrow 0$ during the matter era, respectively. Ignoring the mass of neutrinos and modifications to gravity, one can obtain the growth rate by solving a single differential equation (Wang & Steinhardt 1998; Linder & Jenkins 2003).³²

The seven-year normalization prior is

$$\Delta_{\mathcal{R}}^2(k_{WMAP}) = (2.208 \pm 0.078) \times 10^{-9} \text{ (68% CL)},$$

where $k_{WMAP} = 0.027 \text{ Mpc}^{-1}$. For comparison, the five-year normalization prior was $\Delta_{\mathcal{R}}^2(0.02 \text{ Mpc}^{-1}) = (2.21 \pm 0.09) \times 10^{-9}$. This normalization prior is valid for models with $\Omega_k \neq 0$, $w \neq -1$, or $m_v > 0$. However, these normalizations cannot be used for the models that have the tensor modes, $r > 0$, or the running index, $dn_s/d\ln k \neq 0$.

5.5. WMAP Distance Prior

The temperature power spectrum of CMB is sensitive to the physics at the decoupling epoch, $z = 1090$, as well as the physics between now and the decoupling epoch. The former primarily affects the amplitude of acoustic peaks, i.e., the ratios of the peak heights and the Silk damping. The latter changes the locations of peaks via the angular diameter distance out to the

³² See, e.g., Equation (80) of Komatsu et al. (2009a). Note that there is a typo in that equation: $w_{\text{eff}}(a)$ needs to be replaced by $w(a)$.

Table 9
WMAP Distance Priors Obtained from the *WMAP* Seven-year Fit to Models with Spatial Curvature and Dark Energy

d_i	Seven-year ML ^a	Seven-year Mean ^b	Error, σ
l_A	302.09	302.69	0.76
R	1.725	1.726	0.018
z_*	1091.3	1091.36	0.91

Notes. The correlation coefficients are $r_{l_A,R} = 0.1956$, $r_{l_A,z_*} = 0.4595$, and $r_{R,z_*} = 0.7357$.

^a Maximum likelihood values (recommended).

^b Mean of the likelihood.

decoupling epoch. One can quantify this by (1) the “acoustic scale,” l_A ,

$$l_A = (1 + z_*) \frac{\pi D_A(z_*)}{r_s(z_*)}, \quad (56)$$

where z_* is the redshift of decoupling, for which we use the fitting formula of Hu & Sugiyama (1996), as well as by (2) the “shift parameter,” R (Bond et al. 1997),

$$R = \frac{\sqrt{\Omega_m H_0^2}}{c} (1 + z_*) D_A(z_*). \quad (57)$$

These two parameters capture most of the constraining power of the *WMAP* data for dark energy properties (Wang & Mukherjee 2007; Wright 2007; Elgarøy & Multamäki 2007; Corasaniti & Melchiorri 2008), with one important difference. The distance prior does not capture the information on the growth of structure probed by the late-time ISW effect. As a result, the dark energy constraints derived from the distance prior are similar to, but weaker than, those derived from the full analysis (Komatsu et al. 2009a; Li et al. 2008).

We must understand the limitation of this method. Namely, the distance prior is applicable only when the model in question is based on

1. the standard Friedmann–Lemaitre–Robertson–Walker universe with matter, radiation, dark energy, as well as spatial curvature,
2. neutrinos with the effective number of neutrinos equal to 3.04, and the minimal mass ($m_\nu \sim 0.05 \text{ eV}$), and
3. nearly power-law primordial power spectrum of curvature perturbations, $|dn_s/d\ln k| \ll 0.01$, negligible primordial gravitational waves relative to the curvature perturbations, $r \ll 0.1$, and negligible entropy fluctuations relative to the curvature perturbations, $\alpha \ll 0.1$.

In Tables 9 and 10, we provide the seven-year distance prior. The errors in l_A , R , and z_* have improved from the five-year values by 12%, 5%, and 2%, respectively. To compute the likelihood, use

$$-2 \ln L = \sum_{ij} (x_i - d_i)(C^{-1})_{ij}(x_j - d_j), \quad (58)$$

where $x_i = (l_A, R, z_*)$ is the values predicted by a model in question, $d_i = (l_A^{WMAP}, R^{WMAP}, z_*^{WMAP})$ is the data given in Table 9, and C_{ij}^{-1} is the inverse covariance matrix given in Table 10. Also see Section 5.4.1 of Komatsu et al. (2009a) for more information.

Table 10
Inverse Covariance Matrix for the WMAP Distance Priors

	l_A	R	z_*
l_A	2.305	29.698	-1.333
R		6825.270	-113.180
z_*			3.414

6. PRIMORDIAL NON-GAUSSIANITY

6.1. Motivation and Background

During the period of cosmic inflation (Starobinskiĭ 1979; Starobinsky 1982; Guth 1981; Sato 1981; Linde 1982; Albrecht & Steinhardt 1982), quantum fluctuations were generated and became the seeds for the cosmic structures that we observe today (Mukhanov & Chibisov 1981; Hawking 1982; Starobinsky 1982; Guth & Pi 1982; Bardeen et al. 1983). (Also see Linde 2008, 1990, Mukhanov et al. 1992, Liddle & Lyth 2000, 2009, Bassett et al. 2006 for reviews.)

Inflation predicts that the statistical distribution of primordial fluctuations is nearly a Gaussian distribution with random phases. Measuring deviations from a Gaussian distribution, i.e., *non-Gaussian* correlations in primordial fluctuations, is a powerful test of inflation, as how precisely the distribution is (non-)Gaussian depends on the detailed physics of inflation (see Bartolo et al. 2004; Komatsu et al. 2009b, for reviews).

In this paper, we constrain the amplitude of non-Gaussian correlations using the angular bispectrum of CMB temperature anisotropy, the harmonic transform of the three-point correlation function (see Komatsu 2001, for a review). The observed angular bispectrum is related to the three-dimensional bispectrum of primordial curvature perturbations, $\langle \zeta_{\mathbf{k}_1} \zeta_{\mathbf{k}_2} \zeta_{\mathbf{k}_3} \rangle = (2\pi)^3 \delta^D(\mathbf{k}_1 + \mathbf{k}_2 + \mathbf{k}_3) B_\zeta(k_1, k_2, k_3)$. In the linear order, the primordial curvature perturbation is related to Bardeen's curvature perturbation (Bardeen 1980) in the matter-dominated era, Φ , by $\zeta = \frac{5}{3}\Phi$ (e.g., Kodama & Sasaki 1984). The CMB temperature anisotropy in the Sachs–Wolfe limit (Sachs & Wolfe 1967) is given by $\Delta T/T = -\frac{1}{3}\Phi = -\frac{1}{5}\zeta$. We write the bispectrum of Φ as

$$\langle \Phi_{\mathbf{k}_1} \Phi_{\mathbf{k}_2} \Phi_{\mathbf{k}_3} \rangle = (2\pi)^3 \delta^D(\mathbf{k}_1 + \mathbf{k}_2 + \mathbf{k}_3) F(k_1, k_2, k_3). \quad (59)$$

We shall explore three different shapes of the primordial bispectrum: “local,” “equilateral,” and “orthogonal.” They are defined as follows:

1. **Local form.** The local form bispectrum is given by (Gangui et al. 1994; Verde et al. 2000; Komatsu & Spergel 2001)

$$\begin{aligned} F_{\text{local}}(k_1, k_2, k_3) &= 2f_{NL}^{\text{local}} [P_\Phi(k_1)P_\Phi(k_2) + P_\Phi(k_2)P_\Phi(k_3) \\ &\quad + P_\Phi(k_3)P_\Phi(k_1)] \\ &= 2A^2 f_{NL}^{\text{local}} \left[\frac{1}{k_1^{4-n_s} k_2^{4-n_s}} + (\text{2 perm.}) \right], \end{aligned} \quad (60)$$

where $P_\Phi = A/k^{4-n_s}$ is the power spectrum of Φ with a normalization factor A . This form is called the local form, as this bispectrum can arise from the curvature perturbation in the form of $\Phi = \Phi_L + f_{NL}^{\text{local}} \Phi_L^2$, where both sides are evaluated at the same location in space (Φ_L is a linear

Gaussian fluctuation).³³ Equation (60) peaks at the so-called squeezed triangle for which $k_3 \ll k_2 \approx k_1$ (Babich et al. 2004). In this limit, we obtain

$$F_{\text{local}}(k_1, k_1, k_3 \rightarrow 0) = 4f_{NL}^{\text{local}} P_\Phi(k_1) P_\Phi(k_3). \quad (61)$$

How large is f_{NL}^{local} from inflation? The earlier calculations showed that f_{NL}^{local} from single-field slow-roll inflation would be of order the slow-roll parameter, $\epsilon \sim 10^{-2}$ (Salopek & Bond 1990; Falk et al. 1993; Gangui et al. 1994). More recently, Maldacena (2003) and Acquaviva et al. (2003) found that the coefficient of $P_\Phi(k_1) P_\Phi(k_3)$ from the simplest single-field slow-roll inflation with the canonical kinetic term in the squeezed limit is given by

$$F_{\text{local}}(k_1, k_1, k_3 \rightarrow 0) = \frac{5}{3}(1 - n_s) P_\Phi(k_1) P_\Phi(k_3). \quad (62)$$

Comparing this result with the form predicted by the f_{NL}^{local} model, one obtains $f_{NL}^{\text{local}} = (5/12)(1 - n_s)$, which gives $f_{NL}^{\text{local}} = 0.015$ for $n_s = 0.963$.

2. **Equilateral form.** The equilateral form bispectrum is given by (Creminelli et al. 2006)

$$\begin{aligned} F_{\text{equil}}(k_1, k_2, k_3) &= 6A^2 f_{NL}^{\text{equil}} \left\{ -\frac{1}{k_1^{4-n_s} k_2^{4-n_s}} - \frac{1}{k_2^{4-n_s} k_3^{4-n_s}} \right. \\ &\quad - \frac{1}{k_3^{4-n_s} k_1^{4-n_s}} - \frac{2}{(k_1 k_2 k_3)^{2(4-n_s)/3}} \\ &\quad \left. + \left[\frac{1}{k_1^{(4-n_s)/3} k_2^{2(4-n_s)/3} k_3^{4-n_s}} + (\text{5 perm.}) \right] \right\}. \end{aligned} \quad (63)$$

This function approximates the bispectrum forms that arise from a class of inflation models in which scalar fields have non-canonical kinetic terms. One example is the so-called Dirac–Born–Infeld inflation (Silverstein & Tong 2004; Alishahiha et al. 2004), which gives $f_{NL}^{\text{equil}} \propto -1/c_s^2$ in the limit of $c_s \ll 1$, where c_s is the effective sound speed at which scalar field fluctuations propagate. There are various other models that can produce f_{NL}^{equil} (Arkani-Hamed et al. 2004; Seery & Lidsey 2005; Chen et al. 2007; Cheung et al. 2008; Li et al. 2008). The local and equilateral forms are nearly orthogonal to each other, which means that both can be measured nearly independently.

3. **Orthogonal form.** The orthogonal form, which is constructed such that it is nearly orthogonal to both the local and equilateral forms, is given by (Senatore et al. 2010)

³³ However, $\Phi = \Phi_L + f_{NL}^{\text{local}} \Phi_L^2$ is not the only way to produce this type of bispectrum. One can also produce this form from multi-scalar field inflation models where scalar field fluctuations are nearly scale invariant (Lyth & Rodriguez 2005); multi-scalar models called “curvaton” scenarios (Linde & Mukhanov 1997; Lyth et al. 2003); multi-field models in which one field modulates the decay rate of inflaton field (Dvali et al. 2004a, 2004b; Zaldarriaga 2004); multi-field models in which a violent production of particles and nonlinear reheating, called “preheating,” occur due to parametric resonances (Engquist et al. 2005; Jokinen & Mazumdar 2006; Chambers & Rajantie 2008; Bond et al. 2009); models in which the universe contracts first and then bounces (see Lehners 2008, for a review).

$$F_{\text{orthog}}(k_1, k_2, k_3) = 6A^2 f_{NL}^{\text{orthog}} \left\{ -\frac{3}{k_1^{4-n_s} k_2^{4-n_s}} - \frac{3}{k_2^{4-n_s} k_3^{4-n_s}} \right. \\ \left. - \frac{3}{k_3^{4-n_s} k_1^{4-n_s}} - \frac{8}{(k_1 k_2 k_3)^{2(4-n_s)/3}} \right. \\ \left. + \left[\frac{3}{k_1^{(4-n_s)/3} k_2^{2(4-n_s)/3} k_3^{4-n_s}} + (5 \text{ perm.}) \right] \right\}. \quad (64)$$

This form approximates the forms that arise from a linear combination of higher-derivative scalar-field interaction terms, each of which yields forms similar to the equilateral shape. Senatore et al. (2010) found that, using the “effective field theory of inflation” approach (Cheung et al. 2008), a certain linear combination of similarly equilateral shapes can yield a distinct shape which is orthogonal to both the local and equilateral forms.

Note that these are not the most general forms one can write down, and there are other forms which would probe different aspects of the physics of inflation (Moss & Xiong 2007; Moss & Graham 2007; Chen et al. 2007; Holman & Tolley 2008; Chen & Wang 2010; Chen & Wang 2010).

Of these forms, the local form bispectrum has special significance. Creminelli & Zaldarriaga (2004) showed that not only models with the canonical kinetic term, but *all* single-inflation models predict the bispectrum in the squeezed limit given by Equation (62), regardless of the form of potential, kinetic term, slow-roll, or initial vacuum state (also see Seery & Lidsey 2005; Chen et al. 2007; Cheung et al. 2008). This means that a convincing detection of f_{NL}^{local} would rule out *all* single-field inflation models.

6.2. Analysis Method and Results

The first limit on f_{NL}^{local} was obtained from the *COBE* 4-year data (Bennett et al. 1996) by Komatsu et al. (2002), using the angular bispectrum. The limit was improved by an order of magnitude when the *WMAP* first year data were used to constrain f_{NL}^{local} (Komatsu et al. 2003). Since then the limits have improved steadily as *WMAP* collect more years of data and the bispectrum method for estimating f_{NL}^{local} has improved (Komatsu et al. 2005; Creminelli et al. 2006, 2007; Spergel et al. 2007; Yadav & Wandelt 2008; Komatsu et al. 2009a; Smith et al. 2009).³⁴

In this paper, we shall adopt the optimal estimator (developed by Babich 2005; Creminelli et al. 2006, 2007; Smith & Zaldarriaga 2006; Yadav et al. 2008), which builds on and significantly improves the original bispectrum estimator proposed by Komatsu et al. (2005), especially when the spatial distribution of instrumental noise is not uniform. For details of the method, see Appendix A of Smith et al. (2009) for f_{NL}^{local} , and Section 4.1 of Senatore et al. (2010) for f_{NL}^{equil} and f_{NL}^{orthog} . To construct the optimal estimators, we need to specify the cosmological parameters. We use the five-year ΛCDM parameters from *WMAP*+BAO+SN, for which $n_s = 0.96$.

³⁴ For references to other methods for estimating f_{NL}^{local} , which do not use the bispectrum directly, see Section 3.5 of Komatsu et al. (2009a). Recently, the “skewness power spectrum” has been proposed as a new way to measure f_{NL}^{local} and other non-Gaussian components such as the secondary anisotropies and point sources (Munshi & Heavens 2010; Smidt et al. 2009; Munshi et al. 2009; Calabrese et al. 2010). In the limit that noise is uniform, their estimator is equivalent to that of Komatsu et al. (2005), which also allows for simultaneous estimations of multiple sources of non-Gaussianity (see Appendix A of Komatsu et al. 2009a). The skewness power spectrum method provides a means to visualize the shape of various bispectra as a function of multipoles.

Table 11

Estimates^a and the Corresponding 68% Intervals of the Primordial non-Gaussianity Parameters (f_{NL}^{local} , f_{NL}^{equil} , f_{NL}^{orthog}) and the Point-source Bispectrum Amplitude, b_{src} (in units of $10^{-5} \mu\text{K}^3 \text{sr}^2$), from the *WMAP* Seven-year Temperature Maps

Band	Foreground ^b	f_{NL}^{local}	f_{NL}^{equil}	f_{NL}^{orthog}	b_{src}
V + W	Raw	59 ± 21	33 ± 140	-199 ± 104	N/A
V + W	Clean	42 ± 21	29 ± 140	-198 ± 104	N/A
V + W	Marg. ^c	32 ± 21	26 ± 140	-202 ± 104	-0.08 ± 0.12
V	Marg.	43 ± 24	64 ± 150	-98 ± 115	0.32 ± 0.23
W	Marg.	39 ± 24	36 ± 154	-257 ± 117	-0.13 ± 0.19

Notes.

^a The values quoted for “V + W” and “Marg.” are our best estimates from the *WMAP* seven-year data. In all cases, the full-resolution temperature maps at HEALPix $N_{\text{side}} = 1024$ are used.

^b In all cases, the KQ75y7 mask is used.

^c “Marg.” means that the foreground templates (synchrotron, free-free, and dust) have been marginalized over. When the foreground templates are marginalized over, the raw and clean maps yield the same f_{NL} values.

We also constrain the bispectrum due to residual (unresolved) point sources, b_{src} . The optimal estimator for b_{src} is constructed by replacing a_{lm}/C_l in Equation (A24) of Komatsu et al. (2009a) with $(C^{-1}a)_{lm}$, and using their Equations (A17) and (A5). The C^{-1} matrix is computed by the multigrid-based algorithm of Smith et al. (2007).

We use the V- and W-band maps at the HEALPix resolution $N_{\text{side}} = 1024$. As the optimal estimator weights the data optimally at all multipoles, we no longer need to choose the maximum multipole used in the analysis, i.e., we use all the data. We use both the raw maps (before cleaning foreground) and foreground-reduced (clean) maps to quantify the foreground contamination of f_{NL} parameters. For all cases, we find the best limits on f_{NL} parameters by combining the V- and W-band maps, and marginalizing over the synchrotron, free-free, and dust foreground templates (Gold et al. 2011). As for the mask, we always use the KQ75y7 mask (Gold et al. 2011).

In Table 11, we summarize our results.

1. **Local form results.** The seven-year best estimate of f_{NL}^{local} is

$$f_{NL}^{\text{local}} = 32 \pm 21 (68\% \text{ CL}).$$

The 95% limit is $-10 < f_{NL}^{\text{local}} < 74$. When the raw maps are used, we find $f_{NL}^{\text{local}} = 59 \pm 21$ (68% CL). When the clean maps are used, but foreground templates are not marginalized over, we find $f_{NL}^{\text{local}} = 42 \pm 21$ (68% CL). These results (in particular the clean-map versus the foreground marginalized) indicate that the foreground emission makes a difference at the level of $\Delta f_{NL}^{\text{local}} \sim 10$.³⁵ We find that the V + W result is lower than the V-band or W-band results. This is possible, as the V + W result contains contributions from the cross-correlations of V and W such as $\langle \text{VVW} \rangle$ and $\langle \text{VWW} \rangle$.

2. **Equilateral form results.** The seven-year best estimate of f_{NL}^{equil} is

$$f_{NL}^{\text{equil}} = 26 \pm 140 (68\% \text{ CL}).$$

³⁵ The effect of the foreground marginalization depends on an estimator. Using the needlet bispectrum, Cabella et al. (2010) found $f_{NL}^{\text{local}} = 35 \pm 42$ and 38 ± 47 (68% CL) with and without the foreground marginalization, respectively.

The 95% limit is $-214 < f_{NL}^{\text{equil}} < 266$. For f_{NL}^{equil} , the foreground marginalization does not shift the central values very much, $\Delta f_{NL}^{\text{equil}} = -3$. This makes sense, as the equilateral bispectrum does not couple small-scale modes to very large-scale modes $l \lesssim 10$, which are sensitive to the foreground emission. On the other hand, the local form bispectrum is dominated by the squeezed triangles, which do couple large- and small-scale modes.

3. Orthogonal form results. The seven-year best estimate of f_{NL}^{orthog} is

$$f_{NL}^{\text{orthog}} = -202 \pm 104 \text{ (68\% CL).}$$

The 95% limit is $-410 < f_{NL}^{\text{orthog}} < 6$. The foreground marginalization has little effect, $\Delta f_{NL}^{\text{orthog}} = -4$.

As for the point-source bispectrum, we do not detect b_{src} in V, W, or V + W. In Komatsu et al. (2009a), we estimated that the residual sources could bias f_{NL}^{local} by a small positive amount and applied corrections using Monte Carlo simulations. In this paper, we do not attempt to make such corrections, but we note that sources could give $\Delta f_{NL}^{\text{local}} \sim 2$ (note that the simulations used by Komatsu et al. (2009a) likely overestimated the effect of sources by a factor of two). As the estimator has changed from that used by Komatsu et al. (2009a), extrapolating the previous results is not trivial. Source corrections to f_{NL}^{equil} and f_{NL}^{orthog} could be larger (Komatsu et al. 2009a), but we have not estimated the magnitude of the effect for the seven-year data.

We used the linear perturbation theory to calculate the angular bispectrum of primordial non-Gaussianity (Komatsu & Spergel 2001). Second-order effects (Pyne & Carroll 1996; Mollerach & Matarrese 1997; Bartolo et al. 2006, 2007; Pitrou 2009, 2010) are expected to give $f_{NL}^{\text{local}} \sim 1$ (Nitta et al. 2009; Senatore et al. 2009a, 2009b; Khatri & Wandelt 2009, 2010; Boubekeur et al. 2009; Pitrou et al. 2008) and are negligible given the noise level of the *WMAP* seven-year data.

Among various sources of secondary non-Gaussianities which might contaminate measurements of primordial non-Gaussianity (in particular f_{NL}^{local}), a coupling between the ISW effect and the weak gravitational lensing is the most dominant source of confusion for f_{NL}^{local} (Goldberg & Spergel 1999; Verde & Spergel 2002; Smith & Zaldarriaga 2006; Serra & Cooray 2008; Hanson et al. 2009; Mangilli & Verde 2009). While this contribution is expected to be detectable and bias the measurement of f_{NL}^{local} for *Planck*, it is expected to be negligible for *WMAP*: using the method of Hanson et al. (2009), we estimate that the expected signal-to-noise ratio of this term in the *WMAP* seven-year data is about 0.8. We also estimate that this term can give f_{NL}^{local} a potential positive bias of $\Delta f_{NL}^{\text{local}} \sim 2.7$. Calabrese et al. (2010) used the skewness power spectrum method of Munshi et al. (2009) to search for this term in the *WMAP* five-year data and found a null result. If we subtract $\Delta f_{NL}^{\text{local}}$ estimated above (for the residual source and the ISW-lensing coupling) from the measured value, $\Delta f_{NL}^{\text{local}}$ becomes more consistent with zero.

From these results, we conclude that the *WMAP* seven-year data are consistent with Gaussian primordial fluctuations to within 95% CL. When combined with the limit on f_{NL}^{local} from SDSS, $-29 < f_{NL}^{\text{local}} < 70$ (95% CL Slosar et al. 2008), we find $-5 < f_{NL}^{\text{local}} < 59$ (95% CL).

7. SUNYAEV-ZEL'DOVICH EFFECT

We review the basics of the SZ effect in Section 7.1. In Section 7.2, we shall test our optimal estimator for extracting the SZ signal from the *WMAP* data using the brightest SZ source on the sky: the Coma cluster. We also present an improved measurement of the SZ effect toward the Coma cluster (3.6σ).

The most significant result from Section 7.3 is the discovery of the thermal/dynamical effect of clusters on the SZ effect. We shall present the measurements of the SZ effects toward nearby ($z \leq 0.09$) galaxy clusters in Vikhlinin et al.'s sample (Vikhlinin et al. 2009a), which were used to infer the cosmological parameters (Vikhlinin et al. 2009b). We then compare the measured SZ flux to the expected flux from the X-ray data on the individual clusters, finding a good agreement. Significance of detection (from merely 11 clusters, excluding Coma) is 6.5σ . By dividing the sample into cooling-flow and non-cooling-flow clusters (or relaxed and non-relaxed clusters), we find a significant difference in the SZ effect between these subsamples.

In Section 7.4, we shall report a significant ($\sim 8\sigma$) statistical detection of the SZ effect at hundreds of positions of the known clusters. We then compare the measured SZ flux to theoretical models as well as to an X-ray-calibrated empirical model, and discuss implications of our measurement, especially a recent measurement of the lower-than-theoretically-expected SZ power spectrum by the SPT Collaboration.

Note that the analyses presented in Sections 7.3 and 7.4 are similar but different in one important aspect: the former uses a handful (29) of clusters with well-measured *Chandra* X-ray data, while the latter uses hundreds of clusters without detailed X-ray data. Therefore, while the latter results have smaller statistical errors (and much larger systematic errors), the former results have much smaller systematic errors (and larger statistical errors).

7.1. Motivation and Background

When CMB photons encounter hot electrons in clusters of galaxies, the temperature of CMB changes due to the inverse Compton scattering by these electrons. This effect, known as the thermal SZ effect (Zel'dovich & Sunyaev 1969; Sunyaev & Zel'dovich 1972), is a source of significant additional (secondary) anisotropies in the microwave sky (see Rephaeli 1995; Birkinshaw 1999; Carlstrom et al. 2002, for reviews).

The temperature change due to the SZ effect in units of thermodynamic temperature, ΔT_{SZ} , depends on frequency, ν , and is given by (for a spherically symmetric distribution of gas):

$$\frac{\Delta T_{\text{SZ}}(\theta)}{T_{\text{cmb}}} = g_{\nu} \frac{\sigma_T}{m_e c^2} \int_{-l_{\text{out}}}^{l_{\text{out}}} dl P_e(\sqrt{l^2 + \theta^2 D_A^2}), \quad (65)$$

where θ is the angular distance from the center of a cluster of galaxies on the sky, D_A is the proper (not comoving) angular diameter distance to the cluster center, l is the radial coordinates from the cluster center along the line of sight, $P_e(r)$ is the electron pressure profile, σ_T is the Thomson cross section, m_e is the electron mass, c is the speed of light, and g_{ν} is the spectral function given by

$$g_{\nu} \equiv x \coth\left(\frac{x}{2}\right) - 4, \quad (66)$$

where $x \equiv h\nu/(k_B T_{\text{cmb}}) \simeq \nu/(56.78 \text{ GHz})$ for $T_{\text{cmb}} = 2.725 \text{ K}$. In the Rayleigh-Jeans limit, $\nu \rightarrow 0$, one finds

$g_v \rightarrow -2$. At the *WMAP* frequencies, $g_v = -1.97, -1.94, -1.91, -1.81$, and -1.56 at $23, 33, 41, 61$, and 94 GHz, respectively. The integration boundary, l_{out} , will be given later.

The thermal SZ effect (when relativistic corrections are ignored) vanishes at $\simeq 217$ GHz. One then finds $g_v > 0$ at higher frequencies; thus, the thermal SZ effect produces a temperature decrement at $\nu < 217$ GHz, vanishes at 217 GHz, and produces a temperature increment at $\nu > 217$ GHz.

The angular power spectrum of temperature anisotropy caused by the SZ effect is sensitive to both the gas distribution in clusters (Atrio-Barandela & Mücke 1999; Komatsu & Kitayama 1999) and the amplitude of matter density fluctuations, i.e., σ_8 (Komatsu & Kitayama 1999; Komatsu & Seljak 2002; Bond et al. 2005). While we have not detected the SZ power spectrum in the *WMAP* data, we have detected the SZ signal from the Coma cluster (Abell 1656) in the one-year (Bennett et al. 2003c) and three-year (Hinshaw et al. 2007) data.

We have also made a statistical detection of the SZ effect by cross-correlating the *WMAP* data with the locations of known clusters in the X-ray Brightest Abell-type Cluster (XBAC; Ebeling et al. 1996) catalog (Bennett et al. 2003c; Hinshaw et al. 2007). In addition, there have been a number of statistical detections of the SZ effect reported by many groups using various methods (Fosalba et al. 2003; Hernández-Monteagudo & Rubiño-Martín 2004; Hernández-Monteagudo et al. 2004; Myers et al. 2004; Afshordi et al. 2005; Lieu et al. 2006; Bielby & Shanks 2007; Afshordi et al. 2007; Atrio-Barandela et al. 2008; Kashlinsky et al. 2008; Diego & Partridge 2010; Melin et al. 2010).

7.2. Coma Cluster

The Coma cluster (Abell 1656) is a nearby ($z = 0.0231$) massive cluster located near the north Galactic pole (l, b) = (56°75, 88°05). The angular diameter distance to Coma, calculated from $z = 0.0231$ and $(\Omega_m, \Omega_\Lambda) = (0.277, 0.723)$, is $D_A = 67 h^{-1}$ Mpc; thus, 10 arcmin on the sky corresponds to the physical distance of $0.195 h^{-1}$ Mpc at the redshift of Coma.

To extract the SZ signal from the *WMAP* temperature map, we use the optimal method described in Appendix C: we write down the likelihood function that contains CMB, noise, and the SZ effect, and marginalize it over CMB. From the resulting likelihood function for the SZ effect, which is given by Equation (C7), we find the optimal estimator for the SZ effect in a given angular bin α , \hat{p}_α , as

$$\hat{p}_\alpha = F_{\alpha\beta}^{-1}(t_\beta)_{v'p'}[N_{\text{pix}} + \tilde{C}_{v'p',vp}^{-1}d_{vp}], \quad (67)$$

where the repeated symbols are summed. Here, d_{vp} is the measured temperature at a pixel p in a frequency band v , $(t_\alpha)_{vp}$ is a map of an annulus corresponding to a given angular bin α , which has been convolved with the beam and scaled by the frequency dependence of the SZ effect, $N_{\text{pix},vp,v'p'}$ is the noise covariance matrix (which is taken to be diagonal in pixel space and v , i.e., $N_{\text{pix},vp,v'p'} = \sigma_{vp}^2 \delta_{vv'} \delta_{pp'}$), and $\tilde{C}_{v'p',vp} \equiv \sum_{lm} C_l b_{vl} b_{v'l} Y_{lm,p} Y_{lm,p'}^*$ is the signal covariance matrix of CMB convolved with the beam (C_l and b_{vl} are the CMB power spectrum and the beam transfer function, respectively). A matrix $F_{\alpha\beta}$ gives the 1σ error of \hat{p}_α as $\sqrt{(F^{-1})_{\alpha\alpha}}$, and is given by

$$F_{\alpha\beta} = (t_\alpha)_{v'p'}[N_{\text{pix}} + \tilde{C}_{v'p',vp}^{-1}(t_\beta)_{vp}]. \quad (68)$$

For d_{vp} , we use the foreground-cleaned V- and W-band temperature maps at the HEALPix resolution of $N_{\text{side}} = 1024$,

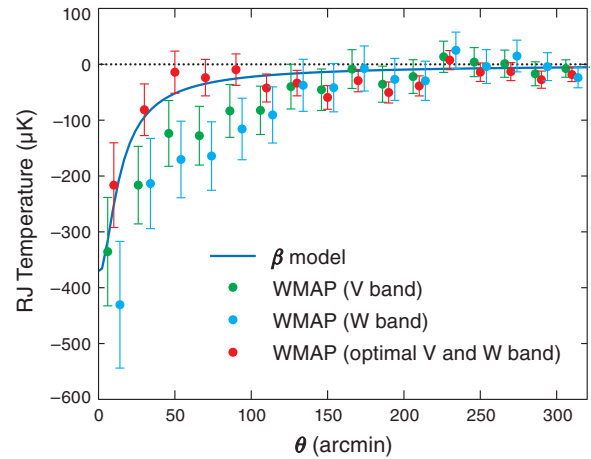


Figure 14. Angular radial profile of the SZ effect toward the Coma cluster, in units of the Rayleigh–Jeans (RJ) temperature (μK). While the V- (green) and W-band (blue) measurements are contaminated by the CMB fluctuations around Coma, our optimal estimator can separate the SZ effect and CMB when the V- and W-band measurements are combined (red). The solid line shows the best-fitting spherical β model with the core radius of $\theta_c = 10.5$ arcmin and $\beta = 0.75$. The best-fitting central temperature decrement (fit to a β model) is $T_{\text{SZ,RJ}}(0) = -377 \pm 105 \mu\text{K}$. Note that 10 arcmin corresponds to the physical distance of $0.195 h^{-1}$ Mpc at the location of Coma. The radius within which the mean overdensity is 500 times the critical density of the universe, r_{500} , corresponds to about 50 arcmin.

masked by the KQ75y7 mask. Note that the KQ75y7 mask includes the seven-year source mask, which removes a potential bias in the reconstructed profile due to any sources which are bright enough to be resolved by *WMAP*, as well as the sources found by other surveys. Specifically, the seven-year point-source mask includes sources in the seven-year *WMAP* source catalog (Gold et al. 2011); sources from Stickel et al. (1994); sources with 22 GHz fluxes ≥ 0.5 Jy from Hirabayashi et al. (2000); flat spectrum objects from Teräsranta et al. (2001); and sources from the blazar survey of Perlman et al. (1998) and Landt et al. (2001).

In Figure 14, we show the measured angular radial profiles of Coma in 16 angular bins (separated by $\Delta\theta = 20$ arcmin), in units of the Rayleigh–Jeans temperature, for the V- and W-band data, as well as for the V + W combined data. The error bar at a given angular bin is given by $\sqrt{(F^{-1})_{\alpha\alpha}}$.

We find that all of these measurements agree well at $\theta \geq 130$ arcmin; however, at smaller angular scales, $\theta \leq 110$ arcmin, the V + W result shows less SZ than both the V- and W-only results. Does this make sense? As described in Appendix C, our optimal estimator uses both the C^{-1} -weighted V + W map and the N^{-1} -weighted V – W map. While the latter map vanishes for CMB, it does not vanish for the SZ effect. Therefore, the latter map can be used to separate CMB and SZ effectively.

This explains why the V + W result and the other results are different only at small angular scales: at $\theta \geq 130$ arcmin, the measured signal is $|\Delta T| \lesssim 50 \mu\text{K}$. If this was due to SZ, the difference map, V – W, would give $|\Delta T| \lesssim (1 - 1.56/1.81) \times 50 \mu\text{K} \simeq 7 \mu\text{K}$, which is smaller than the noise level in the difference map, and thus would not show up. In other words, our estimator cannot distinguish between CMB and SZ at $\theta \geq 130$ arcmin.

On the other hand, at $\theta \leq 110$ arcmin, each of the V- and W-band data shows much bigger signals, $|\Delta T| \gtrsim 100 \mu\text{K}$. If this was due to SZ, the difference map would give $|\Delta T| \gtrsim 14 \mu\text{K}$, which is comparable to or greater than the noise level in the

difference map, and thus would be visible. We find that the difference map does not detect signals in $50 \leq \theta \leq 110$ arcmin, which suggests that the measured signal, $-100 \mu\text{K}$, is *not* due to SZ, but due to CMB. As a result, the V + W result shows less SZ than the V- and W-only results.

In order to quantify a statistical significance of detection and interpret the result, we model the SZ profile using a spherical β model (Cavaliere & Fusco-Femiano 1976):

$$\Delta T_{\text{SZ}}(\theta) = \Delta T_{\text{SZ}}(0)[1 + (\theta/\theta_c)^2]^{(1-3\beta)/2}. \quad (69)$$

To make our analysis consistent with previous measurements described later, we fix the core radius, θ_c , and the slope parameter, β , at $\theta_c = 10.5$ arcmin and $\beta = 0.75$ (Briel et al. 1992), and vary only the central decrement, $\Delta T_{\text{SZ}}(0)$. In this case, the optimal estimator is

$$\Delta T_{\text{SZ}}(0) = \frac{1}{F} t_{v'p'} [N_{\text{pix}} + \tilde{C}]_{v'p', vp}^{-1} d_{vp}, \quad (70)$$

where t_{vp} is a map of the above β model with $\Delta T_{\text{SZ}}(0) = 1$, and

$$F = t_{v'p'} [N_{\text{pix}} + \tilde{C}]_{v'p', vp}^{-1} t_{vp}, \quad (71)$$

gives the 1σ error as $1/\sqrt{F}$.

For V + W, we find

$$\Delta T_{\text{SZ,RJ}}(0) = -377 \pm 105 \mu\text{K} (68\% \text{ CL}),$$

which is a 3.6σ measurement of the SZ effect toward Coma. In terms of the Compton y -parameter at the center, we find

$$\begin{aligned} y_{\text{WMAP}}(0) &= \frac{-1}{2} \frac{\Delta T_{\text{SZ,RJ}}(0)}{T_{\text{cmb}}} \\ &= (6.9 \pm 1.9) \times 10^{-5} (68\% \text{ CL}). \end{aligned}$$

Let us compare this measurement with the previous measurements. Herbig et al. (1995) used the 5.5 m telescope at the Owens Valley Radio Observatory (OVRO) to observe Coma at 32 GHz. Using the same θ_c and β as above, they found the central decrement of $\Delta T_{\text{SZ,RJ}}(0) = -505 \pm 92 \mu\text{K}$ (68% CL), after subtracting $38 \mu\text{K}$ due to point sources (5C4.81 and 5C4.85). These sources have been masked by our point-source mask, and thus we do not need to correct for point sources.

While our estimate of $\Delta T_{\text{SZ,RJ}}(0)$ is different from that of Herbig et al. (1995) only by 1.2σ , and thus is statistically consistent, we note that Herbig et al. (1995) did not correct for the CMB fluctuation in the direction of Coma. As the above results indicate that the CMB fluctuation in the direction of Coma is on the order of $-100 \mu\text{K}$, it is plausible that the OVRO measurement implies $\Delta T_{\text{SZ,RJ}}(0) \sim -400 \text{ K}$, which is an excellent agreement with the WMAP measurement.

The Coma cluster has been observed also by the Millimetre and Infrared Testagrigia Observatory (MITO) experiment (De Petris et al. 2002). Using the same θ_c and β as above, Battistelli et al. (2003) found $\Delta T_{\text{SZ}}(0) = -184 \pm 39$, -32 ± 79 , and $+172 \pm 36 \mu\text{K}$ (68% CL) at 143, 214, and 272 GHz, respectively, in units of thermodynamic temperatures. As MITO has three frequencies, they were able to separate SZ, CMB, and the atmospheric fluctuation. By fitting these three data points to the SZ spectrum, $\Delta T_{\text{SZ}}/T_{\text{cmb}} = g_v y$, we find $y_{\text{MITO}}(0) = (6.8 \pm 1.0 \pm 0.7) \times 10^{-5}$, which is an excellent agreement with the WMAP measurement. The first error is statistical and the second error is systematic due to 10% calibration error of MITO.

The calibration error of the WMAP data (0.2%; Jarosik et al. 2011) is negligible.

Finally, one may try to fit the multi-wavelength data of $T_{\text{SZ}}(0)$ to separate the SZ effect and CMB. For this purpose, we fit the WMAP data in V- and W-band to the β model without correcting for the CMB fluctuation. We find $-381 \pm 126 \mu\text{K}$ and $-523 \pm 127 \mu\text{K}$ in thermodynamic units (68% CL). The OVRO measurement, $T_{\text{SZ,RJ}}(0) = -505 \pm 92 \mu\text{K}$ (Herbig et al. 1995), has been scaled to the Rayleigh-Jeans temperature with the SZ spectral dependence correction, and thus we use this measurement at $v = 0$. Fitting the WMAP and OVRO data to the SZ effect plus CMB, and the MITO data only to the SZ effect (because the CMB was already removed from MITO using their multi-band data), we find $y(0) = (6.8 \pm 1.0) \times 10^{-5}$ and $\Delta T_{\text{cmb}}(0) = -136 \pm 82 \mu\text{K}$ (68% CL). This result is consistent with our interpretation that the y -parameter of the center of Coma is 7×10^{-5} and the CMB fluctuation is on the order of $-100 \mu\text{K}$.

The analysis presented here shows that our optimal estimator is an excellent tool for extracting the SZ effect from multi-frequency data.

7.3. Nearby Clusters: Vikhlinin et al.'s Low- z sample

The Coma cluster is the brightest SZ cluster on the sky. There are other clusters that are bright enough to be seen by WMAP.

7.3.1. Sample of Nearby ($z < 0.1$) Clusters

In order to select candidates, we use the sample of 49 nearby clusters compiled by Vikhlinin et al. (2009a), which are used by the cosmological analysis given in Vikhlinin et al. (2009b). These clusters are selected from the ROSAT All-sky Survey and have detailed follow-up observations by *Chandra*. The latter property is especially important, as it allows us to directly compare the measured SZ effect in the WMAP data and the expected one from the X-ray data on a cluster-by-cluster basis, without relying on any scaling relations.³⁶

Not all nearby clusters in Vikhlinin et al. (2009a) are suitable for our purpose, as some clusters are too small to be resolved by the WMAP beam. We thus select the clusters that have the radius greater than $14'$ on the sky: specifically, we use the clusters whose $\theta_{500} \equiv r_{500}/D_A(z)$ is greater than $14'$. Here, r_{500} is the radius within which the mean overdensity is 500 times the critical density of the universe. We find that 38 clusters satisfy this condition. (Note that the Coma cluster is not included in this sample.)

Of these, five clusters have $M_{500} \geq 6 \times 10^{14} h^{-1} M_\odot$, 7 clusters have $4 \times 10^{14} h^{-1} M_\odot \leq M_{500} < 6 \times 10^{14} h^{-1} M_\odot$, 13 clusters have $2 \times 10^{14} h^{-1} M_\odot \leq M_{500} < 4 \times 10^{14} h^{-1} M_\odot$, and 13 clusters have $1 \times 10^{14} h^{-1} M_\odot \leq M_{500} < 2 \times 10^{14} h^{-1} M_\odot$. Here, M_{500} is the mass enclosed within r_{500} , i.e., $M_{500} \equiv M(r \leq r_{500})$.

Finally, we remove the clusters that lie within the KQ75y7 mask (including the diffuse and the source mask), leaving 29 clusters for our analysis. (One cluster (A478) in $4 \times 10^{14} h^{-1} M_\odot \leq M_{500} < 6 \times 10^{14} h^{-1} M_\odot$, four clusters in $2 \times 10^{14} h^{-1} M_\odot \leq M_{500} < 4 \times 10^{14} h^{-1} M_\odot$, and four clusters in $1 \times 10^{14} h^{-1} M_\odot \leq M_{500} < 2 \times 10^{14} h^{-1} M_\odot$ are masked, mostly by the point-source mask.) The highest redshift of this sample is $z = 0.0904$ (A2142).

³⁶ For this reason, the analysis given in this section is “cleaner” than the one given in Section 7.4, which uses a larger number of clusters but relies on scaling relations. Nevertheless, the results obtained from the analysis in this section and those in Section 7.4 are in good agreement.

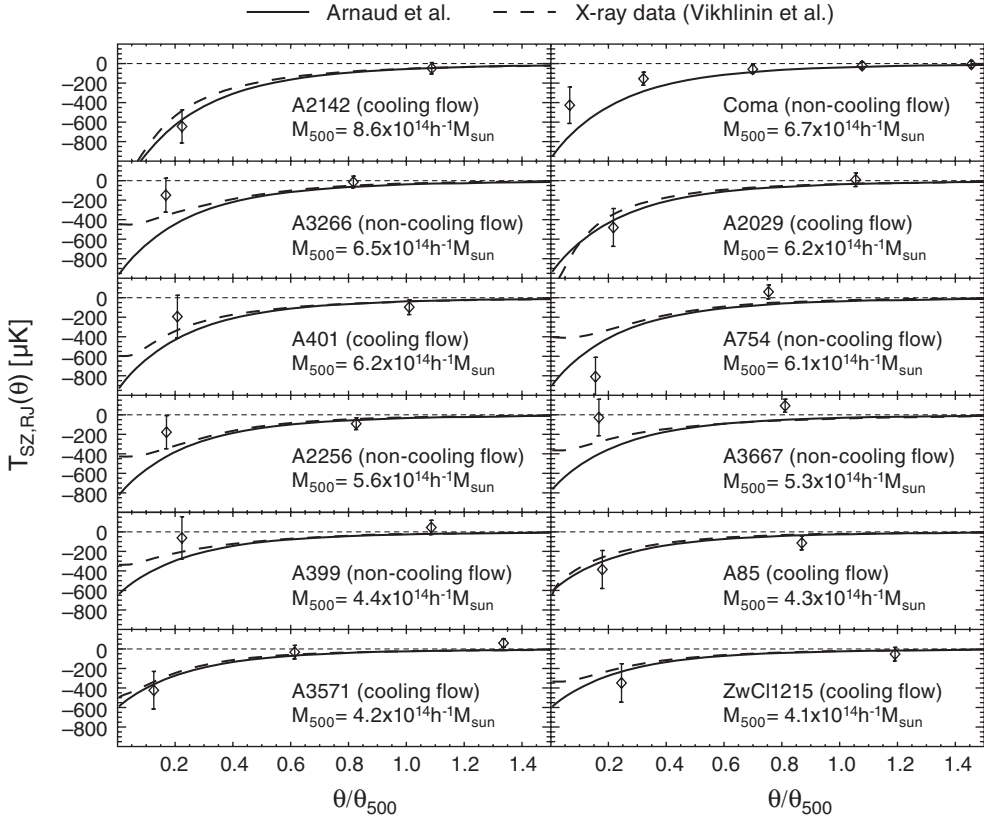


Figure 15. Angular radial profiles of the SZ effect toward nearby massive clusters (with $M_{500} \geq 4 \times 10^{14} h^{-1} M_\odot$ and $z \leq 0.09$), in units of the Rayleigh–Jeans (RJ) temperature (μK). The V- and W-band data are combined optimally to separate the CMB and the SZ effect. All of these clusters have $\theta_{500} \geq 14'$, i.e., resolved by the *WMAP* beam. The masses, M_{500} , are M_Y given in the sixth column of Table 2 in Vikhlinin et al. (2009a), times $h_{\text{vikhlinin}} = 0.72$ used by them, except for Coma. For Coma, we estimate M_{500} using the mass–temperature relation given in Vikhlinin et al. (2009a) with the temperature of 8.45 keV (Wik et al. 2009). The dashed lines show the expected SZ effect from the X-ray data on the individual clusters, whereas the solid lines show the prediction from the average pressure profile found by Arnaud et al. (2010). Note that Coma is not included in the sample of Vikhlinin et al. (2009a), and thus the X-ray data are not shown. We find that Arnaud et al.’s profiles overpredict the gas pressure (hence the SZ effect) of non-cooling flow clusters. Note that all cooling-flow clusters are “relaxed,” and all non-cooling-flow clusters are “non-relaxed” (i.e., morphologically disturbed), according to the criterion of Vikhlinin et al. (2009a).

7.3.2. WMAP Versus X-ray: Cluster-by-cluster Comparison

In Figure 15, we show the measured SZ effect in the symbols with error bars, as well as the expected SZ from the X-ray data in the dashed lines.

To compute the expected SZ, we use Equation (65) with $P_e = n_e k_B T_e$, where n_e and T_e are fits to the X-ray data. Specifically, we use (see Equations (3) and (8) of Vikhlinin et al. 2006)³⁷

$$n_e^2(r) = n_0^2 \frac{(r/r_c)^{-\alpha}}{(1+r^2/r_c^2)^{3\beta-\alpha/2}} \frac{1}{(1+r^\gamma/r_s^\gamma)^{\epsilon/\gamma}} + \frac{n_{02}^2}{(1+r^2/r_{c2}^2)^{3\beta_2}}, \quad (72)$$

$$\frac{T_e(r)}{T_{mg}} = 1.35 \frac{(x/0.045)^{1.9} + 0.45}{(x/0.045)^{1.9} + 1} \frac{1}{[1 + (x/0.6)^2]^{0.45}}, \quad (73)$$

where $x \equiv r/r_{500}$. The parameters in the above equations are found from the *Chandra* X-ray data, and kindly made available to us by A. Vikhlinin.

For a given pressure profile, $P_e(r)$, we compute the SZ temperature profile as

$$\Delta T_{\text{SZ}}(\theta) = g_v T_{\text{cmb}} \frac{\sigma_T}{m_e c^2} P_e^{2d}(\theta) \simeq 273 \mu\text{K} g_v \left[\frac{P_e^{2d}(\theta)}{25 \text{ eV cm}^{-3} \text{ Mpc}} \right], \quad (74)$$

where $P_e^{2d}(\theta)$ is the projected electron pressure profile on the sky:

$$P_e^{2d}(\theta) = \int_{-\sqrt{r_{\text{out}}^2 - \theta^2 D_A^2}}^{\sqrt{r_{\text{out}}^2 - \theta^2 D_A^2}} dl P_e(\sqrt{l^2 + \theta^2 D_A^2}). \quad (75)$$

Here, we truncate the pressure profile at r_{out} . We take this to be $r_{\text{out}} = 6r_{500}$. While the choice of the boundary is somewhat arbitrary, the results are not sensitive to the exact value because the pressure profile declines fast enough.

We find a good agreement between the measured and expected SZ signals (see Figure 15), except for A754: A754 is a merging cluster with a highly disturbed X-ray morphology, and thus the expected SZ profile, which is derived assuming spherical symmetry (Equation (74)), may be different from the observed one.

To make the comparison quantitative, we select clusters within a given mass bin, and fit the expected SZ profiles

³⁷ With a typo in Equation (8) corrected (A. Vikhlinin 2010, private communication).

Table 12Best-fitting Amplitude for the SZ Effect in the *WMAP* Seven-year data

Mass Range ^a	Number of Clusters	Vikhlinin et al. ^b	Arnaud et al. ^c
$6 \leq M_{500} < 9$	5	0.90 ± 0.16	0.73 ± 0.13
$4 \leq M_{500} < 6$	6	0.73 ± 0.21	0.60 ± 0.17
$2 \leq M_{500} < 4$	9	0.71 ± 0.31	0.53 ± 0.25
$1 \leq M_{500} < 2$	9	-0.15 ± 0.55	-0.12 ± 0.47
$4 \leq M_{500} < 9$	11	0.84 ± 0.13	0.68 ± 0.10
$1 \leq M_{500} < 4$	18	0.50 ± 0.27	0.39 ± 0.22
$4 \leq M_{500} < 9$	5	1.06 ± 0.18	0.89 ± 0.15
Cooling flow ^d	6	0.61 ± 0.18	0.48 ± 0.15
$2 \leq M_{500} < 9$	20	0.82 ± 0.12	0.660 ± 0.095
$1 \leq M_{500} < 9$	29	0.78 ± 0.12	0.629 ± 0.094

Notes.

^a In units of $10^{14} h^{-1} M_{\odot}$. Coma is not included. The masses are derived from the mass– Y_X relation, and are given in the sixth column of Table 2 in Vikhlinin et al. (2009a), times $h_{\text{Vikhlinin}} = 0.72$.

^b Derived from the X-ray data on the individual clusters (Vikhlinin et al. 2009a).

^c The “universal pressure profile” given by Arnaud et al. (2010).

^d Definition of “cooling flow” follows that of Vikhlinin et al. (2007). All of cooling-flow clusters here are also “relaxed,” according to the criterion of Vikhlinin et al. (2009a).

^e Definition of “non-cooling flow” follows that of Vikhlinin et al. (2007). All of non-cooling-flow clusters here are also “non-relaxed” (or mergers or morphologically disturbed), according to the criterion of Vikhlinin et al. (2009a).

to the *WMAP* data with a single amplitude, a , treated as a free parameter. The optimal estimator for the normalization of pressure, a , is

$$a = \frac{1}{F} t_{vp'} [N_{\text{pix}} + \tilde{C}]_{vp', vp}^{-1} d_{vp}, \quad (76)$$

where t_{vp} is a map containing the predicted SZ profiles around clusters, and the 1σ error is $1/\sqrt{F}$ where F is given by Equation (71).

We summarize the results in the second column of Table 12. We find that the amplitudes of *all* mass bins are consistent with unity ($a = 1$) to within 2σ (except for the “non-cooling flow” case, for which a is less than unity at 2.2σ ; we shall come back to this important point in the next section). The agreement is especially good for the highest mass bin ($M_{500} \geq 6 \times 10^{14} h^{-1} M_{\odot}$), $a = 0.90 \pm 0.16$ (68% CL).

Note that this is a 5.6σ detection of the SZ effect, just from stacking five clusters. By stacking 11 clusters with $M_{500} \geq 4 \times 10^{14} h^{-1} M_{\odot}$ (i.e., all clusters in Figure 15 but Coma), we find $a = 0.84 \pm 0.13$ (68% CL), a 6.5σ detection. In other words, one does not need to stack many tens or hundreds of clusters to see the SZ effect in the *WMAP* data, contrary to what is commonly done in the literature (Fosalba et al. 2003; Hernández-Monteagudo & Rubiño-Martín 2004; Hernández-Monteagudo et al. 2004; Myers et al. 2004; Afshordi et al. 2005; Lieu et al. 2006; Bielby & Shanks 2007; Afshordi et al. 2007; Atrio-Barandela et al. 2008; Kashlinsky et al. 2008; Diego & Partridge 2010; Melin et al. 2010).

From this study, we conclude that the *WMAP* data and the expectation from the X-ray data are in good agreement.

7.3.3. WMAP Versus a “Universal Pressure Profile” of Arnaud et al.: Effect of Recent Mergers

Recently, Arnaud et al. (2010) derived pressure profiles of 33 clusters from the X-ray follow-up observations of the REX-

CESS clusters using *XMM-Newton*. The REXCESS sample contains clusters selected from the *ROSAT* All-sky Survey (Böhringer et al. 2007). By scaling the pressure profiles appropriately by mass and redshift and taking the median of the scaled profiles, they produced a “universal pressure profile.” We describe this profile in Appendix D.1.

We show the predicted $\Delta T_{\text{SZ}}(\theta)$ from Arnaud et al.’s pressure profile in Figure 15 (solid lines). In order to compute their profile, we need the mass of clusters, M_{500} . We take M_{500} from the sixth column of Table 2 in Vikhlinin et al. (2009a), which are derived from the so-called mass– Y_X relation, the most precise mass proxy known to date with a scatter of about 5%.³⁸ Again, we take the outer boundary of the pressure to be $r_{\text{out}} = 6r_{500}$.

We fit Arnaud et al.’s profiles to the *WMAP* data of 29 clusters. We find that, in all but one of the mass bins, the best-fitting normalization, a , is less than unity by more than 2σ . By stacking 11 clusters with $M_{500} \geq 4 \times 10^{14} h^{-1} M_{\odot}$, we find $a = 0.68 \pm 0.10$ (68% CL). This measurement rules out $a = 1$ by 3.2σ . The universal pressure profile overestimates the SZ effect by $\sim 30\%$.

What causes the discrepancy? The thermal/dynamical state of gas in clusters may be the culprit. From Figure 15, we find that the X-ray data (hence the SZ effect) and the universal profile agree well for “cooling flow” clusters, but do not agree for non-cooling flow clusters.

The cooling flow clusters have *cool cores*, in which the cooling time (due to bremsstrahlung) is shorter than the Hubble time (Fabian 1994). The clusters shown in Figure 15 are classified as either “cooling flow” or “non-cooling flow” clusters, following the definition of Vikhlinin et al. (2007).

We find that Arnaud et al.’s profiles agree with the X-ray data on the individual clusters well at $\theta \gtrsim 0.3\theta_{500}$. This agrees with Figure 8 of Arnaud et al. (2010). The profiles differ significantly in the inner parts of clusters, which is also in good agreement with the conclusion of Arnaud et al. (2010): they find that cool-core clusters show much steeper inner profiles than non-cool-core clusters (their Figures 2 and 5).

For cooling-flow clusters, the agreement between the *WMAP* data and Arnaud et al.’s profile is good: $a = 0.89 \pm 0.15$ (68% CL). However, for non-cooling-flow clusters, we find a very low amplitude, $a = 0.48 \pm 0.15$ (68% CL), which rules out Arnaud et al.’s profile by 3.5σ . A similar trend is also observed for the individual X-ray data of Vikhlinin et al.: $a = 1.06 \pm 0.18$ and 0.61 ± 0.18 (68% CL) for cooling-flow and non-cooling-flow clusters, respectively; however, statistical significance is not large enough to exclude $a = 1$.

Based on this study, we conclude that one must distinguish between cool-core (cooling flow) and non-cool-core clusters when interpreting the observed profile of the SZ effect. It is clear (at the 3.2σ level) that Arnaud et al.’s profile is inconsistent with the individual X-ray data and the SZ data taken by *WMAP*, and (at the 3.5σ level) one must distinguish between the cool-core and non-cool-core clusters.

Interestingly, *all* of cooling-flow clusters are “relaxed” clusters, and *all* of non-cooling-flow clusters are “non-relaxed” (i.e., morphologically disturbed) clusters, according to the criterion of Vikhlinin et al. (2009a). If we interpret this as non-cooling-

³⁸ The exception is Coma, which is not included in the nearby sample of Vikhlinin et al. (2009a). Therefore, we use the mass–temperature relation of Vikhlinin et al. (2009a) (the first row of Table 3) for this cluster:

$M_{500} = (3.02 \pm 0.11) \times 10^{14} h^{-1} M_{\odot} (T_X / 5 \text{ keV})^{1.53 \pm 0.08} / E(z)$, with $E(z) = 1.01$ for Coma’s redshift, $z = 0.023$. We use the X-ray temperature of $T_X = 8.45 \pm 0.06$ keV (Wik et al. 2009).

flow clusters having undergone recent mergers, then we may conclude that we are finding the effect of mergers on the SZ effect.

While our conclusion is still based on a limited number of clusters, it may be valid for a much larger sample of clusters, as we shall show in Section 7.5.4.

Finally, we note that the current generation of hydrodynamical simulations predict the pressure profiles that are even steeper than Arnard et al.’s profile (see Figure 7 of Arnaud et al. 2010). Therefore, the simulations also overpredict the amount of pressure in clusters relative to the *WMAP* data. We shall come back to this point in Section 7.5.5.

7.4. Statistical Detection of the SZ Effect

To explore the SZ effect in a large number of clusters, we use a galaxy cluster catalog consisting of the *ROSAT*-ESO flux-limited X-ray (REFLEX) galaxy cluster survey (Böhringer et al. 2004) in the southern hemisphere above the Galactic plane ($\delta < 2.5^\circ$ and $|b| > 20^\circ$) and the extended Brightest Cluster Sample (eBCS; Ebeling et al. 1998, 2000) in the northern hemisphere above the Galactic plane ($\delta > 0^\circ$ and $|b| > 20^\circ$). Some clusters are contained in both samples. Eliminating the overlap, this catalog contains 742 clusters of galaxies. Of these, 400, 228, and 114 clusters lie in the redshift ranges of $z \leq 0.1$, $0.1 < z \leq 0.2$, and $0.2 < z \leq 0.45$, respectively.

We use the foreground-reduced V- and W-band maps at the HEALPix resolution of $N_{\text{side}} = 1024$, masked by the KQ75y7 mask, which eliminates the entire Virgo cluster. Note that this mask also includes the point-source mask, which masks sources at the locations of some clusters (such as Coma). After applying the mask, we have 361, 214, and 109 clusters in $z \leq 0.1$, $0.1 < z \leq 0.2$, and $0.2 < z \leq 0.45$, respectively.

We again use Equation (67) to find the angular radial profile in four angular bins. For this analysis, $(t_\alpha)_{vp}$ is a map containing many annuli (one annulus around each cluster) corresponding to a given angular bin α , convolved with the beam and scaled by the frequency dependence of the SZ effect.

We show the measured profile in the top panel of Figure 16. We have done this analysis using three different choices of the maximum redshift, z_{max} , to select clusters: $z_{\text{max}} = 0.1$, 0.2, and 0.45. We find that the results are not sensitive to z_{max} . As expected, the results for $z_{\text{max}} = 0.1$ have the largest error bars. The error bars for $z_{\text{max}} = 0.2$ and 0.45 are similar, indicating that we do not gain much more information from $z > 0.2$. The error bars have contributions from instrumental noise and CMB fluctuations. The latter contribution correlates the errors at different angular bins.

The top panel shows a decrement of $-3.6 \pm 1.4 \mu\text{K}$ at a very large angular distance from the center, $\theta = 63$ arcmin, for $z_{\text{max}} = 0.2$. As we do not expect to have such an extended gas distribution around clusters, one may wonder if this result implies that we have a bias in the zero level. In order to check for a potential systematic bias, we perform the following null test: instead of measuring the SZ signals from the locations of clusters, we measure them from random locations in the *WMAP* data. In the middle panel of Figure 16, we show that our method passes a null test. We find that the measured profiles are consistent with zero; thus, our method does not introduce a bias.

Is this signal at a degree scale real? For example, are there nearby massive clusters (such as Coma) which give a significant SZ effect at a degree scale? While the Virgo cluster has the largest angular size on the sky, the KQ75y7 mask eliminates

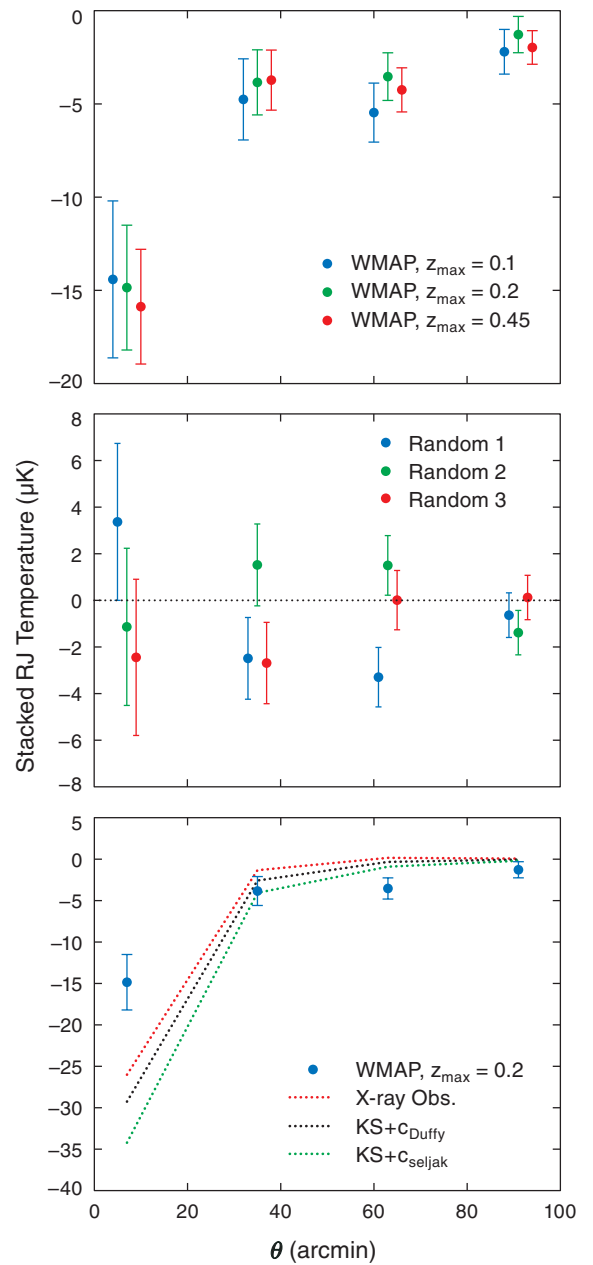


Figure 16. Average temperature profile of the SZ effect from the stacking analysis, in units of the Rayleigh-Jeans (RJ) temperature (μK), at $\theta = 7, 35, 63$, and 91 arcmin. The V- and W-band data are combined using the optimal estimator. Top: the SZ effect measured from the locations of clusters of galaxies. The results with three different maximum redshifts, $z_{\text{max}} = 0.1$ (blue; left), 0.2 (green; middle), and 0.45 (red; right), are shown. The error bars include noise due to the CMB fluctuation, and thus are correlated (see Equation (77) for the correlation matrix). Middle: a null test showing profiles measured from random locations on the sky (for $z_{\text{max}} = 0.2$; the number of random locations is the same as the number of clusters used in the top panel). Three random realizations are shown. Our method does not produce biased results. Bottom: the measured profile ($z_{\text{max}} = 0.2$) is compared with the model profiles derived from the median of 33 clusters in the REXCESS sample (Arnaud et al. 2010) and theoretically calculated from hydrostatic equilibrium (Komatsu & Seljak 2001) with two different concentration parameters. Note that the model profiles are calculated also for $z_{\text{max}} = 0.2$ but have not been multiplied by the best-fitting normalization factors given in Table 13. The theoretical profiles are processed in the same manner that the data are processed, using Equation (68).

Virgo. In order to see if other nearby clusters give significant contributions, we remove all clusters at $z \leq 0.03$ (where there are 57 clusters) and remeasure the SZ profile. We find that

the changes are small, less than $1 \mu\text{K}$ at all angular bins. At $\theta = 63$ arcmin, the change is especially small, $\sim 0.1 \mu\text{K}$, and thus nearby clusters do not make much contribution to this bin.

The apparent decrement at $\theta = 63$ arcmin is probably due to a statistical fluctuation. The angular bins are correlated with the following correlation matrix:

$$\begin{pmatrix} 1 & 0.5242 & 0.0552 & 0.0446 \\ 0.5242 & 1 & 0.4170 & 0.0638 \\ 0.0552 & 0.4170 & 1 & 0.4402 \\ 0.0446 & 0.0638 & 0.4402 & 1 \end{pmatrix}, \quad (77)$$

where the columns correspond to $\theta = 7, 35, 63$, and 91 arcmin, respectively. The decrements at the first two bins (at $\theta = 7$ and 35 arcmin) can drive the third bin at $\theta = 63$ arcmin to be more negative. Note also that one of the realizations shown in the bottom panel (“Random 1” in the middle panel of Figure 16) shows $\sim -3.5 \mu\text{K}$ at $\theta = 63$ arcmin. The second bin is also negative with a similar amplitude. On the other hand, “Random 2” shows both positive temperatures at the second and third bins, which is also consistent with a positive correlation between these bins.

Finally, in the bottom panel of Figure 16, we compare the measured SZ profile with the expected profiles from various cluster gas models (described in Section 7.5). None of them show a significant signal at $\theta = 63$ arcmin, which is also consistent with our interpretation that it is a statistical fluctuation.

7.5. Interpretations

7.5.1. General Idea

In order to interpret the measured SZ profile, we need a model for the electron pressure profile, $P_e(r)$ (see Equation (65)). For fully ionized gas, the electron pressure is related to the *gas* (baryonic) pressure, $P_{\text{gas}}(r)$, by

$$P_e(r) = \left(\frac{2+2X}{3+5X} \right) P_{\text{gas}}(r), \quad (78)$$

where X is the abundance of hydrogen in clusters. For $X = 0.76$, one finds $P_e(r) = 0.518 P_{\text{gas}}(r)$.

We explore three possibilities: (1) Arnaud et al.’s profile that we have used in Section 7.3, (2) theoretical profiles derived by assuming that the gas pressure is in hydrostatic equilibrium with gravitational potential given by a Navarro–Frenk–White (NFW; Navarro et al. 1997) mass density profile (Komatsu & Seljak 2001), and (3) theoretical profiles from hydrodynamical simulations of clusters of galaxies with and without gas cooling and star formation (Nagai et al. 2007).

Case (2) is relevant because this profile is used in the calculation of the SZ power spectrum (Komatsu & Seljak 2002) that has been used as a template to marginalize over in the cosmological parameter estimation since the three-year analysis (Spergel et al. 2007; Dunkley et al. 2009; Larson et al. 2011). Analytical models and hydrodynamical simulations for the SZ signal are also the basis for planned efforts to use the SZ signal to constrain cosmological models.

As we have shown in the previous section using 29 nearby clusters, Arnaud et al.’s pressure profile overpredicts the SZ effect in the *WMAP* data by $\sim 30\%$. An interesting question is whether this trend extends to a larger number of clusters.

7.5.2. Komatsu–Seljak Profile

The normalization of the KS profile has been fixed by assuming that the gas density at the virial radius is equal

to the cosmic mean baryon fraction, Ω_b/Ω_m , times the total mass density at the virial radius. This is an upper limit: for example, star formation turns gas into stars, reducing the amount of gas. KS also assumes that the gas is virialized and in thermal equilibrium (i.e., electrons and protons share the same temperature) everywhere in a cluster, that virialization converts potential energy of the cluster into thermal energy only, and that the pressure contributed by bulk flows, cosmic rays, and magnetic fields are unimportant.

We give details of the gas pressure profiles in Appendix D. In the top left panel of Figure 17, we show Arnaud et al.’s pressure profiles (see Appendix D.1) in the solid lines, and the KS profiles (see Appendix D.2) in the dotted and dashed lines. One of the inputs for the KS profile is the so-called concentration parameter of the NFW profile. The dotted line is for the concentration parameter of $c = 10(M_{\text{vir}}/3.42 \times 10^{12} h^{-1} M_\odot)^{-0.2}/(1+z)$ (Seljak 2000), which was used by Komatsu & Seljak (2002) for their calculation of the SZ power spectrum. Here, M_{vir} is the virial mass, i.e., mass enclosed within the virial radius. The dashed line is for $c = 7.85(M_{\text{vir}}/2 \times 10^{12} h^{-1} M_\odot)^{-0.081}/(1+z)^{0.71}$, which was found from recent *N*-body simulations with the *WMAP* five-year cosmological parameters (Duffy et al. 2008).

We find that the KS profiles and Arnaud et al.’s profiles generally agree. The agreement is quite good especially for the KS profile with the concentration parameter of Duffy et al. (2008). The KS profiles tend to overestimate the gas pressure relative to Arnaud et al.’s one for low-mass clusters ($M_\odot \lesssim 10^{14} h^{-1} M_\odot$). Can we explain this trend by a smaller gas mass fraction in clusters than the cosmic mean? To answer this, we compute the gas mass fraction by integrating the gas density profile:

$$f_{\text{gas}} \equiv \frac{M_{\text{gas},500}}{M_{500}} = \frac{4\pi \int_0^{r_{500}} r^2 dr \rho_{\text{gas}}(r)}{M_{500}}, \quad (79)$$

where M_{500} and $M_{\text{gas},500}$ are the total mass and gas mass contained within r_{500} , respectively.

In Figure 18, we show f_{gas} from X-ray observations (Vikhlinin et al. 2009a):

$$f_{\text{gas}}(h/0.72)^{3/2} = 0.125 + 0.037 \log_{10}(M_{500}/10^{15} h^{-1} M_\odot), \quad (80)$$

for $h = 0.7$, and f_{gas} from the KS profiles with the concentration parameters of Seljak (2000) and Duffy et al. (2008). We find that the KS predictions, $f_{\text{gas}} \simeq 0.12$, are always much smaller than the cosmic mean baryon fraction, $\Omega_b/\Omega_m = 0.167$, and are nearly independent of mass. A slight dependence on mass is due to the dependence of the concentration parameters on mass. While the KS profile is normalized such that the gas density at the virial radius is Ω_b/Ω_m times the total mass density, the gas mass within r_{500} is much smaller than Ω_b/Ω_m times M_{500} , as the gas density and total matter density profiles are very different near the center: while the gas density profile has a constant-density core, the total matter density, which is dominated by dark matter, increases as $\rho_m \propto 1/r$ near the center.

However, the behavior of f_{gas} measured from X-ray observations is very different. It has a much steeper dependence on mass than predicted by KS. The reason for such a steep dependence on mass is not yet understood. It could be due to star formation occurring more effectively in lower mass clusters. In any case, for $M_{500} = 3 \times 10^{14} h^{-1} M_\odot$, the observed gas mass fraction is $f_{\text{gas}} \simeq 0.11$, which is only 10% smaller than the KS value, 0.12. For $M_{500} = 3 \times 10^{13} h^{-1} M_\odot$, the observed gas mass fraction, 0.08, is about 30% smaller than the KS value. This is consistent

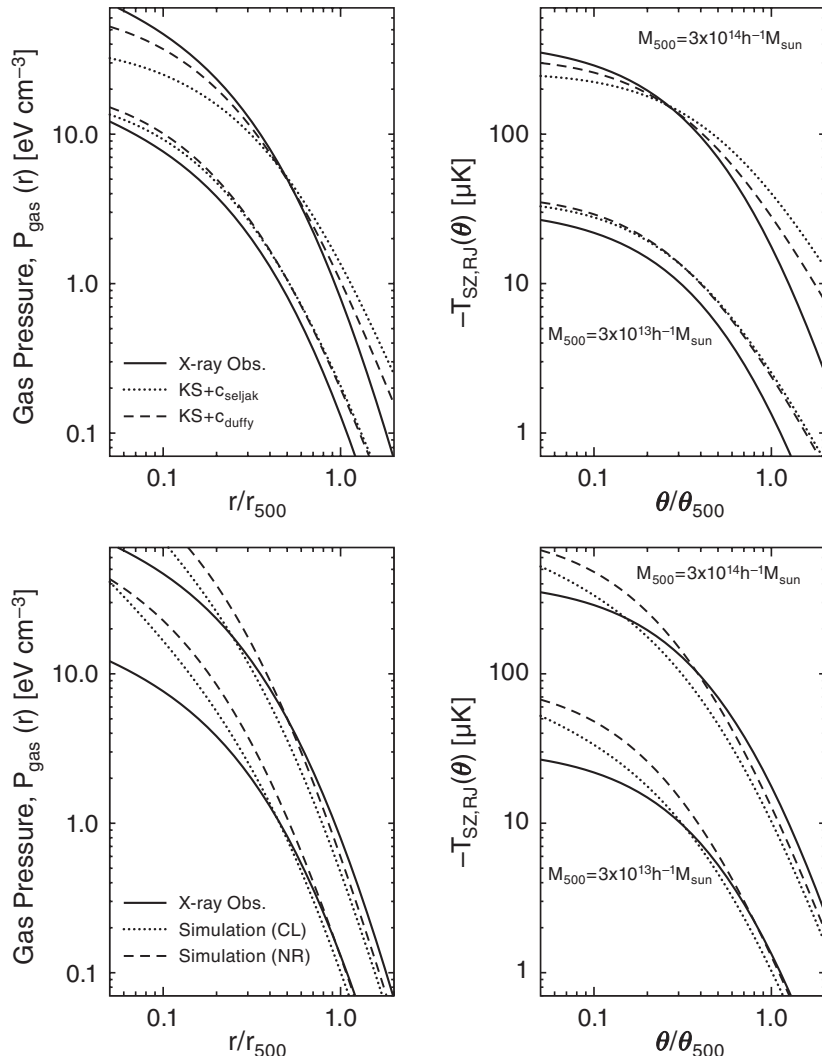


Figure 17. Gas pressure profiles of clusters of galaxies, $P_{\text{gas}}(r)$, at $z = 0.1$, and the projected profiles of the SZ effect, $\Delta T_{\text{SZ}}(\theta)$ (Rayleigh–Jeans temperature in μK). Top left: the gas pressure profiles. The upper and bottom set of curves show $M_{500} = 3 \times 10^{14}$ and $3 \times 10^{13} h^{-1} M_\odot$, respectively. The horizontal axis shows radii scaled by the corresponding $r_{500} = 0.78$ and $0.36 h^{-1} \text{Mpc}$, respectively. The solid lines show $P_{\text{gas}}(r) = P_e(r)/0.518$ derived from X-ray observations (Arnaud et al. 2010), while the dotted and dashed lines show $P_{\text{gas}}(r)$ predicted from hydrostatic equilibrium (Komatsu & Seljak 2001) with NFW concentration parameters of Seljak (2000) and Duffy et al. (2008), respectively. Top right: the projected SZ profiles computed from the corresponding curves in the top left panel and Equation (74). The horizontal axis shows angular radii scaled by $\theta_{500} = r_{500}/D_A$, which is 10 and 4.7 arcmin for $M_{500} = 3 \times 10^{14}$ and $3 \times 10^{13} h^{-1} M_\odot$, respectively. Bottom left: same as the top left panel, but the dotted and dashed lines show $P_{\text{gas}}(r)$ predicted from “Cooling+Star Formation” and “Non-radiative” simulation runs by Nagai et al. (2007). Bottom right: same as the top right panel, but the dotted and dashed lines are computed from the corresponding curves in the bottom left panel and Equation (74).

with the difference between the KS and Arnaud et al.’s pressure profiles that we see in Figure 17; thus, once the observed mass dependence of f_{gas} is taken into account, these profiles agree well.

To calibrate the amplitude of gas pressure, we shall use the KS pressure profile (without any modification to f_{gas}) as a template, and find its normalization, a , from the *WMAP* data using the estimator given in Equation (76). We shall present the results for hydrodynamical simulations later.

For a given gas pressure profile, $P_{\text{gas}}(r)$, we compute the electron pressure as $P_e = 0.518P_{\text{gas}}$ (see Equation (78)). We then use Equation (74) to calculate the expected SZ profile, $\Delta T_{\text{SZ}}(\theta)$. We take the outer boundary of the pressure to be three times the virial radius, $r_{\text{out}} = 3r_{\text{vir}}$, which is the same as the parameter used by Komatsu & Seljak (2002). In the right panels of Figure 17, we show the predicted $\Delta T_{\text{SZ}}(\theta)$, which will be used as templates, i.e., t_{vp} .

7.5.3. Luminosity–Size Relation

Now, in order to compute the expected pressure profiles from each cluster in the catalog, we need to know r_{500} . We calculate r_{500} from the observed X-ray luminosity in *ROSAT*’s 0.1–2.4 keV band, L_X , as

$$r_{500} = \frac{(0.753 \pm 0.063) h^{-1} \text{Mpc}}{E(z)} \times \left(\frac{L_X}{10^{44} h^{-2} \text{erg s}^{-1}} \right)^{0.228 \pm 0.015}, \quad (81)$$

where $E(z) \equiv H(z)/H_0 = [\Omega_m(1+z)^3 + \Omega_\Lambda]^{1/2}$ for a ΛCDM model. This is an empirical relation found from X-ray observations (see Equation (2) of Böhringer et al. 2007) based upon the temperature– L_X relation from Ikebe et al. (2002) and the r_{500} –temperature relation from Arnaud et al. (2005). The

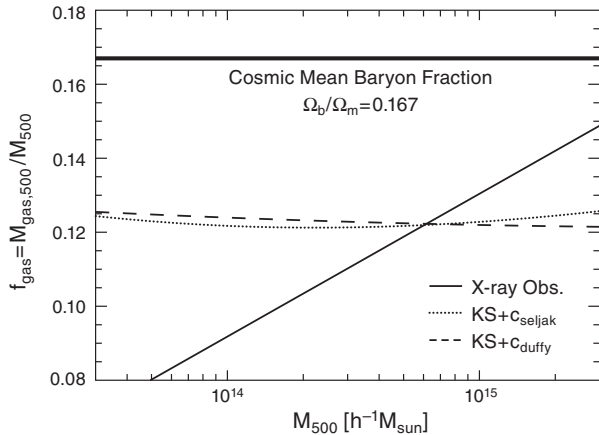


Figure 18. Gas mass fraction as a function of M_{500} . The thick horizontal line shows the cosmic mean baryon fraction, $\Omega_b/\Omega_m = 0.167$. The solid line shows the gas mass fraction, $f_{\text{gas}} = M_{\text{gas},500}/M_{500}$, derived from X-ray observations (Vikhlinin et al. 2009a), while the dotted and dashed lines show f_{gas} predicted from hydrostatic equilibrium (Komatsu & Seljak 2001) with NFW concentration parameters of Seljak (2000) and Duffy et al. (2008), respectively.

error bars have been calculated by propagating the errors in the temperature– L_X and r_{500} –temperature relations. Admittedly, there is a significant scatter around this relation, which is the most dominant source of systematic error in this type of analysis. (The results presented in Section 7.3 do not suffer from this systematic error, as they do not rely on L_X – r_{500} relations.) As $M_{500} \propto r_{500}^3$, a $\approx 10\%$ error in the predicted values of r_{500} gives the mass calibration error of $\approx 30\%$. Moreover, the SZ effect is given by M_{500} times the gas temperature, the latter being proportional to $M_{500}^{2/3}$ according to the virial theorem. Therefore, the total calibration error can be as big as $\approx 50\%$.

In order to quantify this systematic error, we repeat our analysis for three different size–luminosity relations: (1) the central values, (2) the normalization and slope shifted up by 1σ to 0.816 and 0.243, and (3) the normalization and slope shifted down by 1σ to 0.690 and 0.213. We adopt this as an estimate for the systematic error in our results due to the size–luminosity calibration error. For how this error would affect our conclusions, see Section 7.7.

Note that this estimate of the systematic error is conservative, as we allowed *all* clusters to deviate from the best-fit scaling relation at once by $\pm 1\sigma$. In reality, the nature of this error is random, and thus the actual error caused by the scatter in the scaling relation would probably be smaller. Melin et al. (2010) performed such an analysis and found that the systematic error is sub-dominant compared to the statistical error.

Nevertheless, we shall adopt our conservative estimate of the systematic error, as the mean scaling relation also varies from authors to authors. The mean scaling relations used by Melin et al. (2010) are within the error bar of the scaling relation that we use (Equation (81)).

In Figure 19, we show the distribution of M_{500} estimated from clusters in the catalog using the measured values of L_X and Equations (81) and (D2). The distribution peaks at $M_{500} \sim 3 \times 10^{14} h^{-1} M_\odot$ for $z_{\text{max}} = 0.2$ and 0.45, while it peaks at $M_{500} \sim 1.5 \times 10^{14} h^{-1} M_\odot$ for $z_{\text{max}} = 0.1$.

7.5.4. Results: Arnaud et al.’s Profile

For Arnaud et al.’s pressure profile, we find the best-fitting amplitudes of $a = 0.64 \pm 0.09$ and 0.59 ± 0.07 (68% CL) for $z_{\text{max}} = 0.1$ and 0.2, respectively. The former result is

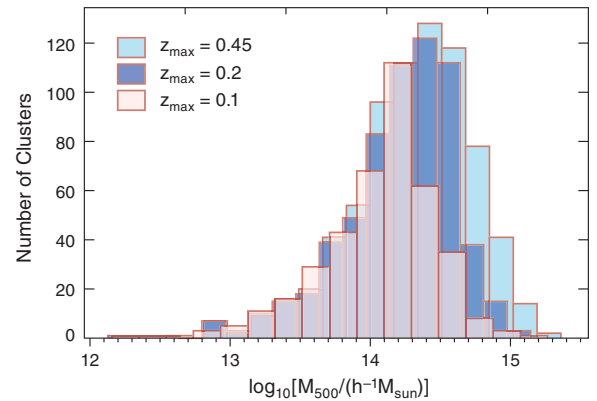


Figure 19. Distribution of M_{500} estimated from clusters in the catalog using the measured X-ray luminosities in 0.1–2.4 keV band, L_X , and Equations (81) and (D2). The light blue, dark blue, and pink histograms show $z_{\text{max}} = 0.45$, 0.2, and 0.1, respectively.

fully consistent with what we find from the nearby clusters in Section 7.3: $a = 0.63 \pm 0.09$ (68% CL; for $1 \times 10^{14} h^{-1} M_\odot \leq M_{500} < 9 \times 10^{14} h^{-1} M_\odot$ and $z \leq 0.09$).

The significance level of statistical detection of the SZ effect is about 8σ for $z_{\text{max}} = 0.2$. With the systematic error included, we find $a = 0.59 \pm 0.07^{+0.38}_{-0.23}$ for $z_{\text{max}} = 0.2$; however, the above agreement may suggest that the fiducial scaling relation (Equation (81)) is, in fact, a good one.

As we have shown in Section 7.3, the measured SZ effects and the predictions from the X-ray data agree on a cluster-by-cluster basis. A plausible explanation for the discrepancy between the *WMAP* data and Arnaud et al.’s profile is that Arnaud et al.’s profile does not distinguish between cooling-flow and non-cooling-flow clusters.

Nevertheless, this result, which shows that the SZ effect seen in the *WMAP* data is *less* than the average “expectation” from X-ray observations, agrees qualitatively with some of the previous work (Lieu et al. 2006; Bielby & Shanks 2007; Diego & Partridge 2010). The other work showed that the SZ effect seen in the *WMAP* data is consistent with expectations from X-ray observations (Afshordi et al. 2007; Melin et al. 2010).

These authors used widely different methods and cluster catalogs. Lieu et al. (2006) were the first to claim that the SZ effect seen in the *WMAP* data is significantly less than expected from X-ray data, by using 31 clusters compiled by Bonamente et al. (2002). Bielby & Shanks (2007) extended the analysis of Lieu et al. (2006) by using 38 clusters compiled by Bonamente et al. (2006), for which the observational data of the SZ effect from OVRO and Berkeley Illinois Maryland Association (BIMA) are available. They did not use scaling relations, but used a spherical isothermal β model to fit the X-ray surface brightness profile of each cluster in the catalog, and calculated the expected SZ signals, assuming that the intracluster gas is isothermal. Lieu et al. (2006) found that the measured signal is smaller than expected from X-ray data by a factor of 3–4, and Bielby & Shanks (2007) found a similar result for the cluster catalog of Bonamente et al. (2006).

Diego & Partridge (2010) used the same cluster catalog that we use (REFLEX+eBCS), but used a different scaling relation: they related the cluster core radius to the X-ray luminosity (we relate r_{500} to the X-ray luminosity). They found a large discrepancy (similar to Lieu et al. 2006; Bielby & Shanks 2007) when a spherical isothermal β model was used to predict the

SZ signal, while they found a smaller discrepancy (similar to our results) when more realistic gas models were used. Afshordi et al. (2007) used 193 clusters selected from the XBAC catalog. Their catalog consisted of the clusters that have measured X-ray temperatures (>3 keV). They then used a scaling relation between r_{200} and the X-ray temperature. They found that the measured SZ signal and X-ray data are consistent.

Melin et al. (2010) used the five-year *WMAP* data and a bigger sample of 893 clusters and a scaling relation between r_{500} and the X-ray luminosity taken from Pratt et al. (2009) and Arnaud et al. (2010). They compared the measured integrated pressure from the *WMAP* data to the expectation from Arnaud et al.’s profile, and concluded that they agree very well. (The normalization is consistent with unity within the statistical uncertainty.) We find, on the other hand, that the normalization is significantly less than unity compared to the statistical uncertainty. How can we reconcile these results?

One possibility would be the difference in the scaling relations. The scaling relation shifted down by 1σ would make the predicted SZ signals smaller, which would then increase the best-fitting amplitude. Given the size of the systematic error, $a = 0.59 \pm 0.07^{+0.38}_{-0.23}$, $a \approx 1$ may not be inconsistent with the data. Specifically, they used two scaling relations:

$$\begin{aligned} 1. \quad r_{500} &= \frac{0.717 h^{-1} \text{Mpc}}{E^{1.19}(z)} [L_{500}/(10^{44} h^{-2} \text{erg s}^{-1})]^{0.222}, \\ 2. \quad r_{500} &= \frac{0.745 h^{-1} \text{Mpc}}{E^{1.15}(z)} [L_{500}/(10^{44} h^{-2} \text{erg s}^{-1})]^{0.207}, \end{aligned}$$

where the relations 1 and 2 correspond to the “REXCESS” and “intrinsic” relations in Melin et al. (2010), respectively. Here, L_{500} is the X-ray luminosity measured within r_{500} , which is calculated from L_X . While we do not have the conversion factors they used, a typical magnitude of the conversion factors is about 10%, according to Melin et al. (2010). A 10% change in L_X gives a 2% change in r_{500} , which is negligible compared to the other uncertainties; thus, we shall assume that L_X and L_{500} are the same, and repeat our analysis using these scaling relations. We find the amplitudes of $a = 0.78 \pm 0.09$ and 0.69 ± 0.08 ($z_{\max} = 0.2$; 68% CL) for the relations 1 and 2, respectively; thus, while these scaling relations give larger amplitudes, they cannot completely explain the difference between the results of Melin et al. (2010; $a \approx 1$) and our results. However, we find that the discrepancy is much less for high X-ray luminosity clusters; see Section 7.6.

While the method of Melin et al. (2010) and our method are similar, they are different in details. We compare the predicted angular radial profiles of the SZ effect to the *WMAP* data to find the best-fitting amplitude. Melin et al. (2010) measured the *integrated* pressure within five times r_{500} , and converted it to the integrated pressure within r_{500} , Y_{r500} , assuming the distribution of pressure beyond r_{500} is described by the profile of Arnaud et al. (2010). Whether the difference in methodology can account for the difference between our results and their results is unclear, and requires further investigation.³⁹

³⁹ There are also differences in the estimators used. In Melin et al. (2010), a “matched-filter estimator” proposed by Herranz et al. (2002) was used for estimating the normalization of the Arnaud et al. profile. Their estimator is essentially the same as the optimal estimator we derive in Appendix C, with some differences in details of the implementation. Their estimator is given by, in our notation,

$$\hat{p} = \frac{1}{F} \int d^2 \tilde{\mathbf{l}}_{v'1} (P^{-1})_{v'1,v1} \tilde{d}_{v1}, \quad (82)$$

where

$$F \equiv \int d^2 \tilde{\mathbf{l}}_{v'1} (P^{-1})_{v'1,v1} \tilde{d}_{v1}. \quad (83)$$

In any case, we emphasize once again that the SZ effect measured by the *WMAP* and the predictions from X-ray data agree well, when the actual X-ray profile of individual clusters, rather than the average (or median) profile, is used, and there is a reason why Arnaud et al.’s profile would overpredict the pressure (i.e., cooling flows; see Section 7.3). Therefore, it is likely that the difference between our results and Melin et al. (2010) simply points to the fundamental limitation of the analysis using many clusters (with little or no X-ray data) and scaling relations.

7.5.5. Results: KS Profile and Hydrodynamical Simulation

Let us turn our attention to the analytical KS profile. For the KS profile with the concentration parameter of Seljak (2000), we find the best-fitting amplitudes of $a = 0.59 \pm 0.09$ and $0.46 \pm 0.06^{+0.31}_{-0.18}$ (68% CL) for $z_{\max} = 0.1$ and 0.2 , respectively. For the KS profile with the concentration parameter of Duffy et al. (2008), we find $a = 0.67 \pm 0.09$ and $0.58 \pm 0.07^{+0.33}_{-0.20}$ (68% CL) for $z_{\max} = 0.1$ and 0.2 , respectively. These results are consistent with those for Arnaud et al.’s pressure profiles.

Recently, the SPT Collaboration detected the SZ power spectrum at $l \gtrsim 3000$. By fitting their SZ power spectrum data to the theoretical model of Komatsu & Seljak (2002), they found the best-fitting amplitude of $A_{\text{SZ}} = 0.37 \pm 0.17$ (68% CL; Lueker et al. 2010). The calculation of Komatsu & Seljak (2002) is based on the KS gas pressure profile. As the amplitude of SZ power spectrum is proportional to the gas pressure squared, i.e., $A_{\text{SZ}} \propto a^2$, our result for the KS profiles, $a \approx 0.5\text{--}0.7$, is consistent with $A_{\text{SZ}} = 0.37 \pm 0.17$ found from SPT. The ACT Collaboration placed an upper limit of $A_{\text{SZ}} < 1.63$ (95% CL; Fowler et al. 2010), which is consistent with the SPT result.

What do hydrodynamical simulations tell us? As the analytical calculations such as Komatsu & Seljak (2001) are limited, we also fit the pressure profiles derived from hydrodynamical simulations of Nagai et al. (2007) to the *WMAP* data. In the bottom panels of Figure 17, we show the gas pressure profiles from “Non-radiative” and “Cooling+Star Formation (SF)” runs.

By fitting the SZ templates constructed from these simulated profiles to the *WMAP* data, we find the best-fitting amplitudes of $0.50 \pm 0.06^{+0.28}_{-0.18}$ and $0.67 \pm 0.08^{+0.37}_{-0.23}$ (68% CL) for non-radiative and cooling+SF runs, respectively, which are consistent with the amplitudes found for the KS profiles and Arnaud et al.’s profiles. See Table 13 for a summary of the best-fitting amplitudes.

That the KS, simulation, and Arnaud et al.’s profiles yield similar results indicates that *all* of these profiles overpredict the

Here, \tilde{t} and \tilde{d} are the two-dimensional Fourier transforms of a template map, t , and the data map, d , respectively, and $P_{v'1,v1}$ is the power spectrum of the CMB signal plus instrumental noise, both of which are assumed to be diagonal in Fourier space. The summation over the repeated indices is understood. For comparison, our estimator for the same quantity is given by

$$\hat{p} = \frac{1}{F} t_{v'p'} \left(C_{\text{tot}}^{-1} \right)_{v'p',vp} d_{vp}, \quad (84)$$

where $C_{\text{tot}} = N_{\text{pix}} + A S_{\text{harm}} A^T$ is the pixel-space covariance matrix of the CMB signal plus instrumental noise (see Equation (C9)), and

$$F = t_{v'p'} \left(C_{\text{tot}}^{-1} \right)_{v'p',vp} t_{vp}. \quad (85)$$

There are two differences in the implementation: (1) Melin et al. (2010) re-project the *WMAP* data onto 504 square ($10^\circ \times 10^\circ$) tangential overlapping flat patches and calculate the above two-dimensional Fourier transform on each flat patch. We perform the analysis on the full sky by calculating the covariance matrix with the spherical harmonics. (2) Melin et al. (2010) calculate P from the data. We calculate C from the best-fitting Λ CDM model for the CMB signal and the noise model.

Table 13
Best-fitting Amplitude of Gas Pressure Profile^a

Gas Pressure Profile	Type	$z_{\max} = 0.1$	$z_{\max} = 0.2$	High L_X^b	Low L_X^c
Arnaud et al. (2010)	X-ray Obs. (Fid.) ^d	0.64 ± 0.09	$0.59 \pm 0.07^{+0.38}_{-0.23}$	0.67 ± 0.09	0.43 ± 0.12
Arnaud et al. (2010)	REXCESS scaling ^e	N/A	0.78 ± 0.09	0.90 ± 0.12	0.55 ± 0.16
Arnaud et al. (2010)	Intrinsic scaling ^f	N/A	0.69 ± 0.08	0.84 ± 0.11	0.46 ± 0.13
Arnaud et al. (2010)	$r_{\text{out}} = 2r_{500}^g$	N/A	0.59 ± 0.07	0.67 ± 0.09	0.43 ± 0.12
Arnaud et al. (2010)	$r_{\text{out}} = r_{500}^h$	N/A	0.65 ± 0.08	0.74 ± 0.09	0.44 ± 0.14
Komatsu & Seljak (2001)	Equation (D16)	0.59 ± 0.09	$0.46 \pm 0.06^{+0.31}_{-0.18}$	0.49 ± 0.08	0.40 ± 0.11
Komatsu & Seljak (2001)	Equation (D17)	0.67 ± 0.09	$0.58 \pm 0.07^{+0.33}_{-0.20}$	0.66 ± 0.09	0.43 ± 0.12
Nagai et al. (2007)	Non-radiative	N/A	$0.50 \pm 0.06^{+0.28}_{-0.18}$	0.60 ± 0.08	0.33 ± 0.10
Nagai et al. (2007)	Cooling+SF	N/A	$0.67 \pm 0.08^{+0.37}_{-0.23}$	0.79 ± 0.10	0.45 ± 0.14

Notes.

^a The quoted error bars show 68% CL. The first error is statistical, while the second error is systematic. The systematic error is caused by the calibration error in the size–luminosity relation (r_{500} – L_X relation; see Equation (81) and discussion below it). While we quote the systematic error in the amplitudes only for $z_{\max} = 0.2$, the amplitudes for $z_{\max} = 0.1$ also have similar levels of the systematic error. Due to a potential contamination from unresolved radio sources, the best-fitting amplitudes could also be underestimated by ≈ 5 to 10%. This is not included in the systematic error budget because it is sub-dominant. See Section 7.7 for discussion on the point-source contamination.

^b “High L_X ” uses clusters with $4.5 < L_X/(10^{44}\text{ergs}^{-1}) < 45$ and $z \leq 0.2$. Before masking, there are 82 clusters. The quoted errors are statistical.

^c “Low L_X ” uses clusters with $0.45 < L_X/(10^{44}\text{ergs}^{-1}) < 4.5$ and $z \leq 0.2$. Before masking, there are 417 clusters. Clusters less luminous than these (129 clusters are fainter than $0.45 \times 10^{44}\text{ergs}^{-1}$) do not yield a statistically significant detection. The quoted errors are statistical.

^d With the fiducial scaling relation between r_{500} and L_X , $r_{500} = \frac{0.753 h^{-1} \text{Mpc}}{E(z)} [L_X/(10^{44} h^{-2} \text{erg s}^{-1})]^{0.228}$ (Böhringer et al. 2007). For this scaling relation, $L_X = 4.5 \times 10^{44}\text{ergs}^{-1}$ corresponds to $M_{500} = 4.1$ and $3.9 \times 10^{14} h^{-1} M_\odot$ for $z = 0.1$ and 0.2, and $L_X = 0.45 \times 10^{44}\text{ergs}^{-1}$ corresponds to $M_{500} = 0.84$ and $0.80 \times 10^{14} h^{-1} M_\odot$ for $z = 0.1$ and 0.2, respectively.

^e With the “REXCESS” scaling relation, $r_{500} = \frac{0.717 h^{-1} \text{Mpc}}{E^{1.19}(z)} [L_X/(10^{44} h^{-2} \text{erg s}^{-1})]^{0.222}$, used by Melin et al. (2010). For this scaling relation, $L_X = 4.5 \times 10^{44}\text{ergs}^{-1}$ corresponds to $M_{500} = 3.4$ and $3.1 \times 10^{14} h^{-1} M_\odot$ for $z = 0.1$ and 0.2, and $L_X = 0.45 \times 10^{44}\text{ergs}^{-1}$ corresponds to $M_{500} = 0.73$ and $0.68 \times 10^{14} h^{-1} M_\odot$ for $z = 0.1$ and 0.2, respectively. The quoted errors are statistical.

^f With the “intrinsic” scaling relation, $r_{500} = \frac{0.745 h^{-1} \text{Mpc}}{E^{1.15}(z)} [L_X/(10^{44} h^{-2} \text{erg s}^{-1})]^{0.207}$, used by Melin et al. (2010). For this scaling relation, $L_X = 4.5 \times 10^{44}\text{ergs}^{-1}$ corresponds to $M_{500} = 3.7$ and $3.4 \times 10^{14} h^{-1} M_\odot$ for $z = 0.1$ and 0.2, and $L_X = 0.45 \times 10^{44}\text{ergs}^{-1}$ corresponds to $M_{500} = 0.88$ and $0.82 \times 10^{14} h^{-1} M_\odot$ for $z = 0.1$ and 0.2, respectively. The quoted errors are statistical.

^g The gas extension is truncated at $r_{\text{out}} = 2r_{500}$, instead of $6r_{500}$. The fiducial r_{500} – L_X relation is used. The quoted errors are statistical.

^h The gas extension is truncated at $r_{\text{out}} = r_{500}$, instead of $6r_{500}$. The fiducial r_{500} – L_X relation is used. The quoted errors are statistical.

amount of SZ effect seen in the *WMAP* data by $\sim 30\%$ – 50% . This conclusion is made robust by the results we presented in Section 7.3: the analysis that does *not* use scaling relations between L_X and r_{500} , but uses only a subset of clusters that have the detailed follow-up observations by *Chandra*, yields the same result. This is one of the main results of our SZ analysis.

7.6. Luminosity Bin analysis

To see the dependence of the best-fitting normalization on X-ray luminosities (hence M_{500}), we divide the cluster samples into three luminosity bins: (1) “High L_X ” with $4.5 < L_X/(10^{44}\text{ergs}^{-1}) \leq 45$, (2) “Low L_X ” with $0.45 < L_X/(10^{44}\text{ergs}^{-1}) \leq 4.5$, and (3) clusters fainter than (2). There are 82, 417, and 129 clusters in (1), (2), and (3), respectively. In Table 13, we show that we detect significant SZ signals in (1) and (2), despite the smaller number of clusters used in each luminosity bin. We do not have a statistically significant detection in (3).

The high L_X clusters have $M \gtrsim 4 \times 10^{14} h^{-1} M_\odot$. For these clusters, the agreement between the *WMAP* data and the expected SZ signals is much better. In particular, for the REXCESS scaling relation, we find $a = 0.90 \pm 0.12$, which is consistent with unity within the 1σ statistical error. This implies that, at least for high X-ray luminosity clusters, our results and the results of Melin et al. (2010) agree within the statistical uncertainty.

On the other hand, we find that less luminous clusters tend to have significantly lower best-fitting amplitudes for all models of gas-pressure profiles and scaling relations that we have

explored. This trend is consistent with, for example, the gas mass fraction being lower for lower mass clusters. It is also consistent with radio point sources filling some of the SZ effect seen in the *WMAP* data. For the point-source contamination, see Section 7.7.

7.7. Systematic Errors

The best-fitting amplitudes may be shifted up and down by $\approx 50\%$ due to the calibration error in the size–luminosity relation (Equation (81)). As we have shown already, the best-fitting amplitudes for the KS profiles can be shifted up to 0.77 and 0.91 for the concentration parameters of Seljak (2000) and Duffy et al. (2008), respectively. Similarly, the amplitude for Arnaud et al.’s profile can be shifted up to 0.97. As this calibration error shifts all amplitudes given in Table 13 by the same amount, it does not affect our conclusion that all of the gas pressure profiles considered above yield similar results.

This type of systematic error can be reduced by using a subset of clusters of galaxies for which the scaling relations are more tightly constrained (see, e.g., Pratt et al. 2009; Vikhlinin et al. 2009a; Mantz et al. 2010a); however, reducing the number of samples increases the statistical error. Indeed, the analysis presented in Section 7.3 does not suffer from the ambiguity in the scaling relations.

How important are radio point sources? While we have not attempted to correct for potential contamination from unresolved radio point sources, we estimate the magnitude of effects here. If, on average, each cluster has an $F_{\text{src}} = 10 \text{ mJy}$

source, then the corresponding temperatures,

$$\Delta T_{\text{src}} = 40.34 \mu\text{K} \left[\frac{\sinh^2(x/2)}{x^4} \frac{F_{\text{src}}}{10\text{mJy}} \frac{10^{-5}\text{sr}}{\Omega_{\text{beam}}} \right], \quad (86)$$

are 2.24, 2.29, and 2.19 μK in Q, V, and W bands, respectively. Here, $x = v/(56.78\text{GHz})$, and $\Omega_{\text{beam}} = 9.0 \times 10^{-5}, 4.2 \times 10^{-5}$, and 2.1×10^{-5} sr are the solid angles of beams in Q, V, and W bands, respectively (Jarosik et al. 2011). Using the radio sources observed in clusters of galaxies by Lin et al. (2009), Diego & Partridge (2010) estimated that the mean flux of sources in Q band is 10.4 mJy, and that at 90 GHz (which is close to 94 GHz of W band) is $\approx 4\text{--}6$ mJy. Using these estimates, we expect the source contamination at the level of $\approx 1\text{--}2 \mu\text{K}$ in V and W bands, which is $\approx 5\%\text{--}10\%$ of the measured SZ temperature. Therefore, the best-fitting amplitudes reported in Table 13 could be underestimated by $\approx 5\%\text{--}10\%$.

7.8. Discussion

The gas pressure profile is not the only factor that determines the SZ power spectrum. The other important factor is the mass function, dn/dM :

$$C_l \propto \int dz \frac{dV}{dz} \int dM \frac{dn}{dM} |\tilde{P}_l^{2d}|^2, \quad (87)$$

where $V(z)$ is the comoving volume of the universe and \tilde{P}_l^{2d} is the two-dimensional Fourier transform of $P^{2d}(\theta)$. Therefore, a lower-than-expected A_{SZ} may imply either a lower-than-expected amplitude of matter density fluctuations, i.e., σ_8 , or a lower-than-expected gas pressure, or both.

As the predictions for the SZ power spectrum available today (see, e.g., Shaw et al. 2009; Sehgal et al. 2010, and references therein) are similar to the prediction of Komatsu & Seljak (2002) (for example, Lueker et al. 2010 found $A_{\text{SZ}} = 0.55 \pm 0.21$ for the prediction of Sehgal et al. 2010, which is based on the gas model of Bode et al. 2009), a plausible explanation for a lower-than-expected A_{SZ} is a lower-than-expected gas pressure.

Arnaud et al. (2007) find that the X-ray observed integrated pressure enclosed within r_{500} , $Y_X \equiv M_{\text{gas},500} T_X$, for a given M_{500} is about a factor of 0.75 times the prediction from the Cooling+SF simulation of Nagai et al. (2007). This is in good agreement with our corresponding result for the “High L_X ” samples, 0.79 ± 0.10 (68% CL; statistical error only).

While the KS profile is generally in good agreement with Arnaud et al.’s profile, the former is more extended than the latter (see Figure 17), which makes the KS prediction for the projected SZ profiles bigger. Note, however, that the outer slope of the fitting formula given by Arnaud et al. (2010) (Equation (D3)) has been forced to match that from hydrodynamical simulations of Nagai et al. (2007) in $r \geq r_{500}$. See the bottom panels of Figure 17. The steepness of the profile at $r \gtrsim r_{500}$ from the simulation may be attributed to a significant non-thermal pressure support from ρv^2 , which makes it possible to balance gravity by less thermal pressure at larger radii. In other words, the *total* pressure (i.e., thermal plus ρv^2) profile would probably be closer to the KS prediction, but the thermal pressure would decline more rapidly than the total pressure would.

If the SZ effect seen in the *WMAP* data is less than theoretically expected, what would be the implications? One possibility is that protons and electrons do not share the same temperature. The electron–proton equilibration time is longer than the Hubble time at the virial radius, so that the electron temperature

may be lower than the proton temperature in the outer regions of clusters which contribute a significant fraction of the predicted SZ flux (Rudd & Nagai 2009; Wong & Sarazin 2009). The other sources of non-thermal pressure support in outskirts of the cluster (turbulence, magnetic field, and cosmic rays) would reduce the thermal SZ effect relative to the expectation, if these effects are not taken into account in modeling the intracluster medium. Heat conduction may also play some role in suppressing the gas pressure (Loeb 2002, 2007).

In order to explore the impact of gas pressure at $r > r_{500}$, we cut the pressure profile at $r_{\text{out}} = r_{500}$ (instead of $6r_{500}$) and repeat the analysis. We find $a = 0.74 \pm 0.09$ and 0.44 ± 0.14 for high and low L_X clusters, respectively. (We found $a = 0.67 \pm 0.09$ and 0.43 ± 0.12 for $r_{\text{out}} = 6r_{500}$. See Table 13.) These results are somewhat puzzling—the X-ray observations directly measure gas out to r_{500} , and thus we would expect to find $a \approx 1$ at least out to r_{500} . This result may suggest that, as we have shown in Section 7.3, the problem is not with the outskirts of the cluster, but with the inner parts where the cooling flow has the largest effect.

The *relative* amplitudes between high and low L_X clusters suggest that a significant amount of pressure is missing in low-mass ($M_{500} \lesssim 4 \times 10^{14} h^{-1} M_\odot$) clusters, even if we scale all the results such that high-mass clusters are forced to have $a = 1$. A similar trend is also seen in Figure 3 of Melin et al. (2010). This interpretation is consistent with the SZ power spectrum being lower than theoretically expected. The SPT measures the SZ power spectrum at $l \gtrsim 3000$. At such high multipoles, the contributions to the SZ power spectrum are dominated by relatively low-mass clusters, $M_{500} \lesssim 4 \times 10^{14} h^{-1} M_\odot$ (see Figure 6 of Komatsu & Seljak 2002). Therefore, a plausible explanation for the lower-than-expected SZ power spectrum is a missing pressure (relative to theory) in lower mass clusters.

Scaling relations, gas pressure, and entropy of low-mass clusters and groups have been studied in the literature.⁴⁰ Leauthaud et al. (2010) obtained a relation between L_X of 206 X-ray-selected galaxy groups and the mass (M_{200}) derived from the stacking analysis of weak lensing measurements. Converting their best-fitting relation to r_{200} – L_X relation, we find $r_{200} = \frac{1.26 h^{-1} \text{Mpc}}{E^{0.89}(z)} [L_X/(10^{44} h^{-2} \text{erg s}^{-1})]^{0.22}$. (Note that the pivot luminosity of the original scaling relation is $2.6 \times 10^{42} h^{-2} \text{erg s}^{-1}$.) As $r_{500} \approx 0.65 r_{200}$, their relation is $\approx 1\sigma$ higher than the fiducial scaling relation that we adopted (Equation (81)). Had we used their scaling relation, we would find even lower normalizations.

The next generation of simulations or analytical calculations of the SZ effect should be focused more on understanding the gas pressure profiles, both the amplitude and the shape, especially in low-mass clusters. New measurements of the SZ effect toward many individual clusters with unprecedented sensitivity are now becoming available (Staniszewski et al. 2009; Hincks et al. 2009; Plagge et al. 2010). These new measurements would be important for understanding the gas pressure in low-mass clusters.

8. CONCLUSION

With the *WMAP* seven-year temperature and polarization data, new measurements of H_0 (Riess et al. 2009), and improved large-scale structure data (Percival et al. 2010), we have been

⁴⁰ A systematic study of the thermodynamic properties of low-mass clusters and groups is given in Finoguenov et al. (2007; also see Finoguenov et al. 2005a, 2005b).

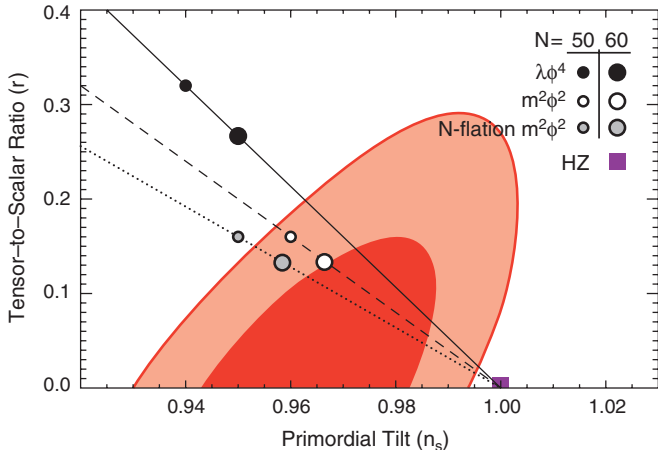


Figure 20. Two-dimensional joint marginalized constraint (68% and 95% CL) on the primordial tilt, n_s , and the tensor-to-scalar ratio, r , derived from the data combination of $WMAP+BAO+H_0$. The symbols show the predictions from “chaotic” inflation models whose potential is given by $V(\phi) \propto \phi^\alpha$ (Linde 1983), with $\alpha = 4$ (solid) and $\alpha = 2$ (dashed) for single-field models, and $\alpha = 2$ for multi-axion field models with $\beta = 1/2$ (dotted; Easter & McAllister 2006).

able to rigorously test the standard cosmological model. The model continues to be an exquisite fit to the existing data. Depending on the parameters, we also use the other data sets such as the small-scale CMB temperature power spectra (Brown et al. 2009; Reichardt et al. 2009, for the primordial helium abundance), the power spectrum of LRGs derived from SDSS (Reid et al. 2010b, for neutrino properties), the Type Ia supernova data (Hicken et al. 2009a, for dark energy), and the time-delay distance to the lens system B1608+656 (Suyu et al. 2010, for dark energy and spatial curvature). The combined data sets enable improved constraints over the $WMAP$ -only constraints on the cosmological parameters presented in Larson et al. (2011) on physically motivated extensions of the standard model.

We summarize the most significant findings from our analysis (also see Tables 2–4):

1. **Gravitational waves and primordial power spectrum.** Our best estimate of the spectral index of a power-law primordial power spectrum of curvature perturbations is $n_s = 0.968 \pm 0.012$ (68% CL). We find no evidence for tensor modes: the 95% CL limit is $r < 0.24$.⁴¹ There is no evidence for the running spectral index, $dn_s/d\ln k = -0.022 \pm 0.020$ (68% CL). Given that the improvements on n_s , r , and $dn_s/d\ln k$ from the five-year results are modest, their implications for models of inflation are similar to those discussed in Section 3.3 of Komatsu et al. (2009a). Also see Kinney et al. (2008), Peiris & Easter (2008) and Finelli et al. (2010) for more recent surveys of implications for inflation. In Figure 20, we compare the seven-year $WMAP+BAO+H_0$ limits on n_s and r to the predictions from inflation models with monomial potential, $V(\phi) \propto \phi^\alpha$.
2. **Neutrino properties.** Better determinations of the amplitude of the third acoustic peak of the temperature power spectrum and H_0 have led to improved limits on the total mass of neutrinos, $\sum m_\nu < 0.58$ eV (95% CL), and the effective number of neutrino species, $N_{\text{eff}} = 4.34^{+0.86}_{-0.88}$ (68% CL), both of which are derived from $WMAP+BAO+H_0$

⁴¹ This is the seven-year $WMAP+BAO+H_0$ limit. The five-year $WMAP+BAO+SN$ limit was $r < 0.22$ (95% CL). For comparison, the seven-year $WMAP+BAO+SN$ limit is $r < 0.20$ (95% CL). These limits do not include systematic errors in the supernova data.

without any information on the growth of structure. When BAO is replaced by the LRG power spectrum, we find $\sum m_\nu < 0.44$ eV (95% CL), and the effective number of neutrino species, $N_{\text{eff}} = 4.25^{+0.76}_{-0.80}$ (68% CL).

3. **Primordial helium abundance.** By combining the $WMAP$ data with the small-scale CMB data, we have detected, by more than 3σ , a change in the Silk damping on small angular scales ($l \gtrsim 500$) due to the effect of primordial helium on the temperature power spectrum. We find $Y_p = 0.326 \pm 0.075$ (68% CL). The astrophysical measurements of helium abundance in stars or H II regions provide tight upper limits on Y_p , whereas the CMB data can be used to provide a lower limit. With a conservative hard prior on $Y_p < 0.3$, we find $0.23 < Y_p < 0.3$ (68% CL). Our detection of helium at $z \sim 1000$ contradicts versions of the “cold big bang model,” where most of the cosmological helium is produced by the first generation of stars (Aguirre 2000).
4. **Parity violation.** The seven-year polarization data have significantly improved over the five-year data. This has led to a significantly improved limit on the rotation angle of the polarization plane due to potential parity-violating effects. Our best limit is $\Delta\alpha = -1.1 \pm 1.4$ (statistical) ± 1.5 (systematic) (68% CL).
5. **Axion dark matter.** The seven-year $WMAP+BAO+H_0$ limit on the non-adiabatic perturbations that are uncorrelated with curvature perturbations, $\alpha_0 < 0.077$ (95% CL), constrains the parameter space of axion dark matter in the context of the misalignment scenario. It continues to suggest that a future detection of tensor-to-scalar ratio, r , at the level of $r = 10^{-2}$ would require a fine-tuning of parameters such as the misalignment angle, $\theta < 3 \times 10^{-9}$, a significant amount of entropy production between the QCD phase transition and the BBN, $\gamma < 0.9 \times 10^{-9}$, a super-Planckian axion decay constant, $f_a > 3 \times 10^{32}$ GeV, an axion contribution to the matter density of the universe being totally sub-dominant, or a combination of all of the above with less tuning in each (also see Section 3.6.3 of Komatsu et al. 2009a). The seven-year $WMAP+BAO+H_0$ limit on correlated isocurvature perturbations, which is relevant to the curvaton dark matter, is $\alpha_{-1} < 0.0047$ (95% CL).
6. **Dark energy.** With $WMAP+BAO+H_0$ but without high-redshift Type Ia supernovae, we find $w = -1.10 \pm 0.14$ (68% CL) for a flat universe. Adding the supernova data reduces the error bar by about a half. For a curved universe, addition of supernova data reduces the error in w dramatically (by a factor of more than four), while the error in curvature is well constrained by $WMAP+BAO+H_0$. In Figure 13, we show the seven-year limits on a time-dependent equation of state in the form of $w = w_0 + w_a(1-a)$. We find $w_0 = -0.93 \pm 0.13$ and $w_a = -0.41^{+0.72}_{-0.71}$ (68% CL) from $WMAP+BAO+H_0+SN$. The data are consistent with a flat universe dominated by a cosmological constant.
7. **Primordial non-Gaussianity.** The 95% CL limits on physically motivated primordial non-Gaussianity parameters are $-10 < f_{NL}^{\text{local}} < 74$, $-214 < f_{NL}^{\text{equil}} < 266$, and $-410 < f_{NL}^{\text{orthog}} < 6$. When combined with the limit on f_{NL}^{local} from SDSS, $-29 < f_{NL}^{\text{local}} < 70$ (Slosar et al. 2008), we find $-5 < f_{NL}^{\text{local}} < 59$. The data are consistent with Gaussian primordial curvature perturbations.
8. **Sunyaev-Zel'dovich effect.** Using the optimal estimator, we have measured the SZ effect toward clusters of galaxies. We have detected the SZ effect toward the Coma cluster at

3.6σ and made the statistical detection of the SZ effect by optimally stacking the *WMAP* data at the locations of known clusters of galaxies. By stacking 11 nearby massive clusters, we detect the SZ effect at 6.5σ , and find that the measured SZ signal and the predictions from the X-ray data agree well. On the other hand, we find that the SZ signal from the stacking analysis is about 0.5–0.7 times the predictions from the current generation of analytical calculations, hydrodynamical simulations, and the “universal pressure profile” of Arnaud et al. (2010). We detect the expected SZ signal in relaxed clusters that have cool cores. We find that the SZ signal from non-relaxed clusters has SZ signals that are 50% of the signal predicted by Arnaud et al.’s profile. The discrepancy with theoretical predictions presents a puzzle. This lower-than-theoretically-expected SZ signal is consistent with the lower-than-theoretically-expected SZ power spectrum recently measured by the SPT Collaboration (Lueker et al. 2010). While we find a better agreement between the *WMAP* data and the expectations for massive clusters with $M_{500} \gtrsim 4 \times 10^{14} h^{-1} M_\odot$, a significant amount of pressure (relative to theory) is missing in lower mass clusters. Our results imply that we may not fully understand the gas pressure in low-mass clusters. This issue would become particularly important when the SZ effect is used as a cosmological probe.

We also reported a novel analysis of the *WMAP* temperature and polarization data that enable us to directly “see” the imprint of adiabatic scalar fluctuations in the maps of polarization directions around temperature hot and cold spots. These give a striking confirmation of our understanding of the physics at the decoupling epoch in the form of radial and tangential polarization patterns at two characteristic angular scales that are important for the physics of acoustic oscillation: the compression phase at $\theta = 2\theta_A$ and the reversal phase at $\theta = \theta_A$.

The CMB data have provided us with many stringent constraints on various properties of our universe. One of many lessons that we have learned from the CMB data is that, given the data that we have, inventions of new, physically motivated, observables beyond the spherically averaged power spectrum often lead to new insights into the physics of the universe. Well-studied examples include primordial non-Gaussianity parameters (f_{NL} from the bispectrum), parity-violation angle ($\Delta\alpha$ from the TB and EB correlations), modulated primordial power spectrum ($g(k)$ from direction-dependent power spectra; Ackerman et al. 2007; Hanson & Lewis 2009; Groeneboom et al. 2010, see Bennett et al. 2011 for the seven-year limits).

The data continue to improve, including more integration of the *WMAP* observations. At the same rate, it is important to find more ways to subject the data to various properties of the universe that have not been explored yet.

The *WMAP* mission is made possible by the support of the Science Mission Directorate Office at NASA Headquarters. This research was additionally supported by NASA grants NNG05GE76G, NNX07AL75G S01, LTSA03-000-0090, ATPNNG04GK55G, ADP03-0000-092, and NNX08AL43G, and NSF grants AST-0807649 and PHY-0758153. E.K. acknowledges support from an Alfred P. Sloan Research Fellowship. J.D. is partly supported by an Research Councils UK (RCUK) fellowship. We thank Mike Greason for his help on the analysis of the *WMAP* data, and T. B. Griswold for the artwork. We thank D. Jeong for his help on calculating the peak

bias presented in Section 2, B. A. Reid for discussion on the treatment of massive neutrinos in the expansion rate which has led to our exact treatment in Section 3.3, A. G. Riess for discussion on the Type Ia supernova data set and the H_0 measurement, M. Sullivan for discussion on the Type Ia supernova data set, S. H. Suyu and P. J. Marshall for providing us with the likelihood function for the time-delay distance and discussion on strong lensing measurements, A. Vikhlinin for the X-ray data on his nearby cluster samples (used in Section 7.3), N. Afshordi, P. Bode, R. Lieu, Y.-T. Lin, D. Nagai, N. Sehgal, L. Shaw, and H. Trac for discussion and feedback on Section 7 (SZ effect), and F. Takahashi for his help on refining the results on axion dark matter presented in Section 4.4. Computations for the analysis of non-Gaussianity in Section 6 were carried out by the Terascale Infrastructure for Groundbreaking Research in Engineering and Science (TIGRESS) at the Princeton Institute for Computational Science and Engineering (PICSciE). This research has made use of NASA’s Astrophysics Data System Bibliographic Services. We acknowledge use of the HEALPix (Gorski et al. 2005), CAMB (Lewis et al. 2000), and CMBFAST (Seljak & Zaldarriaga 1996) packages.

APPENDIX A

EFFECTS OF THE IMPROVED RECOMBINATION HISTORY ON THE Λ CDM PARAMETERS

The constraints on the cosmological parameters reported in the original version of this paper were based on a version of CAMB which used a recombination history calculated by the RECFAST version 1.4.2 (Seager et al. 1999, 2000; Wong et al. 2008; Scott & Moss 2009). Shortly after the submission of the original version, a new version CAMB was released with the RECFAST version 1.5. This revision incorporates the improved treatment of the hydrogen and helium recombination, following numerous work done over the last several years (see Rubiño-Martín et al. 2010, and references therein). Specifically, the code multiplies the ionization fraction, $x_e(z)$, by a cosmology-independent “fudge function,” $f(z)$, found by Rubiño-Martín et al. (2010). A change in the recombination history mostly affects the time and duration of the photon decoupling which, in turn, affects the amount of Silk damping. Therefore, it is expected to affect the cosmological parameters such as n_s and $\Omega_b h^2$ (Rubiño-Martín et al. 2010).

In order to see the effects of the improved recombination code on the cosmological parameters, we have re-run the Λ CDM chain with the latest CAMB code that includes RECFAST version 1.5. We find that the effects are small, and in most cases negligible compared to the error bars; however, we find that the significance at which $n_s = 1$ is excluded is no longer more than 3σ : with the improved recombination code, we find $n_s = 0.968 \pm 0.012$ (68% CL), and $n_s = 1$ is excluded at 99.5% CL.

Finally, the *WMAP* likelihood code has also changed from the initial version (4.0), which used a temperature power spectrum with a slightly incorrect estimate for the residual point-source amplitude, and a TE power spectrum with a slightly incorrect f_{sky} factor. The new version (4.1) corrects both errors; however, the change in the parameters is largely driven by the above modification of the recombination history.

Throughout the main body of this paper, we have adopted the new parameters for the simplest six-parameter Λ CDM model, but we have kept the previous parameters for all the other models because the changes are too small to report. We compare the

Table 14
Comparison of the Λ CDM Parameters ($WMAP+BAO+H_0$): RECFAST Version 1.4.2 Versus 1.5

Class	Parameter	ML (1.5)	ML (1.4.2)	Mean (1.5)	Mean (1.4.2)
Primary	$100\Omega_b h^2$	2.253	2.246	2.255 ± 0.054	2.260 ± 0.053
	$\Omega_c h^2$	0.1122	0.1120	0.1126 ± 0.0036	0.1123 ± 0.0035
	Ω_Λ	0.728	0.728	0.725 ± 0.016	$0.728^{+0.015}_{-0.016}$
	n_s	0.967	0.961	0.968 ± 0.012	0.963 ± 0.012
	τ	0.085	0.087	0.088 ± 0.014	0.087 ± 0.014
Derived	$\Delta_R^2(k_0)$	2.42×10^{-9}	2.45×10^{-9}	$(2.430 \pm 0.091) \times 10^{-9}$	$(2.441^{+0.088}_{-0.092}) \times 10^{-9}$
	σ_8	0.810	0.807	0.816 ± 0.024	0.809 ± 0.024
	H_0	$70.4 \text{ km s}^{-1} \text{ Mpc}^{-1}$	$70.2 \text{ km s}^{-1} \text{ Mpc}^{-1}$	$70.2 \pm 1.4 \text{ km s}^{-1} / \text{Mpc}^{-1}$	$70.4^{+1.3}_{-1.4} \text{ km s}^{-1} / \text{Mpc}^{-1}$
	Ω_b	0.0455	0.0455	0.0458 ± 0.0016	0.0456 ± 0.0016
	Ω_c	0.226	0.227	0.229 ± 0.015	0.227 ± 0.014
	$\Omega_m h^2$	0.1347	0.1344	0.1352 ± 0.0036	0.1349 ± 0.0036
	z_{reion}	10.3	10.5	10.6 ± 1.2	10.4 ± 1.2
	t_0	13.76 Gyr	13.78 Gyr	$13.76 \pm 0.11 \text{ Gyr}$	$13.75 \pm 0.11 \text{ Gyr}$

Λ CDM parameters derived from $WMAP+BAO+H_0$ in Table 14. See Larson et al. (2011) for the comparison of $WMAP$ -only parameters.

APPENDIX B

STACKED PROFILES OF TEMPERATURE AND POLARIZATION OF THE CMB

B.1. Formulae of Stacked Profiles from Peak Theory

In order to calculate the stacked profiles of temperature and polarization of the CMB at the locations of temperature peaks, we need to relate the peak number density contrast, δ_{pk} , to the underlying temperature fluctuation, ΔT .

One often encounters a similar problem in the large-scale structure of the universe: how can we relate the number density contrast of galaxies to the underlying matter density fluctuation? It is often assumed that the number density contrast of peaks with a given peak height v is simply proportional to the underlying density field. If one adopted such a linear and *scale-independent* bias prescription, one would find⁴²

$$\delta_{\text{pk}}(\hat{\mathbf{n}}) = b_v \Delta T(\hat{\mathbf{n}}). \quad (\text{B1})$$

However, our numerical simulations show that the linear bias does not give an accurate description of $\langle Q_r \rangle$ or $\langle T_r \rangle$. In fact, breakdown of the linear bias is precisely what is expected from the statistics of peaks. From detailed investigations of the statistics of peaks, Desjacques (2008) found the following *scale-dependent* bias:

$$\delta_{\text{pk}}(\hat{\mathbf{n}}) = [b_v - b_\zeta (\partial_1^2 + \partial_2^2)] \Delta T(\hat{\mathbf{n}}). \quad (\text{B2})$$

While the first, constant term b_v has been known for a long time (Kaiser 1984; Bardeen et al. 1986), the second term b_ζ has been recognized only recently. The presence of b_ζ is expected because, to define peaks, one needs to use the information on the first and second derivatives of ΔT . As the first derivative must vanish at the locations of peaks, the above equation does not contain the first derivative.

Desjacques (2008) has derived the explicit forms of b_v and b_ζ :

$$b_v = \frac{1}{\sigma_0} \frac{v - \gamma \bar{u}}{1 - \gamma^2}, \quad b_\zeta = \frac{1}{\sigma_2} \frac{\bar{u} - \gamma v}{1 - \gamma^2}, \quad (\text{B3})$$

⁴² For convenience, we write the bias parameters in units of $(\text{temperature})^{-1}$.

where $v \equiv \Delta T / \sigma_0$, $\gamma \equiv \sigma_1^2 / (\sigma_0 \sigma_2)$, σ_j is the rms of j th derivatives of the temperature fluctuation:

$$\sigma_j^2 = \frac{1}{4\pi} \sum_l (2l+1)[l(l+1)]^j C_l^{\text{TT}} (W_l^T)^2, \quad (\text{B4})$$

and W_l^T is the harmonic transform of a window function (which is a combination of the experimental beam, pixel window, and any other additional smoothing applied to the temperature data). The quantity \bar{u} is called the “mean curvature,” and is given by $\bar{u} \equiv G_1(\gamma, \gamma v) / G_0(\gamma, \gamma v)$, where

$$G_n(\gamma, x_*) \equiv \int_0^\infty dx x^n f(x) \frac{\exp[-\frac{(x-x_*)^2}{2(1-\gamma^2)}]}{\sqrt{2\pi(1-\gamma^2)}}. \quad (\text{B5})$$

While Desjacques (2008) applied this formalism to a three-dimensional Gaussian random field, it is straightforward to generalize his results to a two-dimensional case, for which $f(x)$ is given by (Bond & Efstathiou 1987),

$$f(x) = x^2 - 1 + \exp(-x^2). \quad (\text{B6})$$

With the bias given by Equation (B2), we find

$$\langle \delta_{\text{pk}}(\hat{\mathbf{n}}) Q_r(\hat{\mathbf{n}} + \hat{\boldsymbol{\theta}}) \rangle = \int \frac{d^2 \mathbf{l}}{(2\pi)^2} W_l^T W_l^P (b_v + b_\zeta l^2) \times \{C_l^{\text{TE}} \cos[2(\phi - \varphi)] + C_l^{\text{TB}} \sin[2(\phi - \varphi)]\} e^{i \mathbf{l} \cdot \hat{\boldsymbol{\theta}}}, \quad (\text{B7})$$

$$\langle \delta_{\text{pk}}(\hat{\mathbf{n}}) U_r(\hat{\mathbf{n}} + \hat{\boldsymbol{\theta}}) \rangle = - \int \frac{d^2 \mathbf{l}}{(2\pi)^2} W_l^T W_l^P (b_v + b_\zeta l^2) \times \{C_l^{\text{TE}} \sin[2(\phi - \varphi)] - C_l^{\text{TB}} \cos[2(\phi - \varphi)]\} e^{i \mathbf{l} \cdot \hat{\boldsymbol{\theta}}}, \quad (\text{B8})$$

where W_l^T and W_l^P are spherical harmonic transforms of the smoothing functions applied to the temperature and polarization data, respectively. Recalling $\mathbf{l} \cdot \hat{\boldsymbol{\theta}} = l\theta \cos(\phi - \varphi)$, $\int_0^{2\pi} d\varphi \sin[2(\phi - \varphi)] e^{ix \cos(\phi - \varphi)} = 0$, and

$$J_m(x) = \int_x^{2\pi+\alpha} \frac{d\psi}{2\pi} e^{i(m\psi - x \sin \psi)}, \quad (\text{B9})$$

with $m = 2$, $\psi = \varphi - \phi - \pi/2$ and $\alpha = -\phi - \pi/2$, we find

$$\langle \delta_{\text{pk}}(\hat{\mathbf{n}}) Q_r(\hat{\mathbf{n}} + \hat{\boldsymbol{\theta}}) \rangle = - \int \frac{l dl}{2\pi} W_l^T W_l^P (b_v + b_\zeta l^2) C_l^{\text{TE}} J_2(l\theta), \quad (\text{B10})$$

$$\langle \delta_{\text{pk}}(\hat{\mathbf{n}}) U_r(\hat{\mathbf{n}} + \hat{\boldsymbol{\theta}}) \rangle = - \int \frac{l dl}{2\pi} W_l^T W_l^P (b_v + b_\zeta l^2) C_l^{\text{TE}} J_2(l\theta). \quad (\text{B11})$$

Using these results in Equations (9) and (10), we finally obtain the desired formulae for the stacked polarization profiles:

$$\langle Q_r \rangle(\theta) = - \int \frac{l dl}{2\pi} W_l^T W_l^P (b_v + b_\zeta l^2) C_l^{\text{TE}} J_2(l\theta), \quad (\text{B12})$$

$$\langle U_r \rangle(\theta) = - \int \frac{l dl}{2\pi} W_l^T W_l^P (b_v + b_\zeta l^2) C_l^{\text{TB}} J_2(l\theta). \quad (\text{B13})$$

Incidentally, the stacked profile of the temperature fluctuation can also be calculated in a similar way:

$$\langle T \rangle(\theta) = \int \frac{l dl}{2\pi} (W_l^T)^2 (b_v + b_\zeta l^2) C_l^{\text{TT}} J_0(l\theta). \quad (\text{B14})$$

B.2. A Cookbook for Computing $\langle Q_r \rangle(\theta)$ and $\langle U_r \rangle(\theta)$

How can we evaluate Equations (B12)–(B14)? One may follow the following steps:

1. Compute σ_0 , σ_1 , and σ_2 from Equation (B4). For example, the *WMAP* five-year best-fitting temperature power spectrum for a power-law Λ CDM model (Dunkley et al. 2009),⁴³ multiplied by a Gaussian smoothing of 0.5 full-width-at-half-maximum (FWHM) and the pixel window function for the HEALPix resolution of $N_{\text{side}} = 512$, gives $\sigma_0 = 87.9 \mu\text{K}$, $\sigma_1 = 1.16 \times 10^4 \mu\text{K}$, and $\sigma_2 = 2.89 \times 10^6 \mu\text{K}$.
2. Compute $\gamma = \sigma_1^2 / (\sigma_0 \sigma_2)$. For the above example, we find $\gamma = 0.5306$.
3. As we need to integrate over peak heights v , we need to compute the functions $G_0(\gamma, \gamma v)$ and $G_1(\gamma, \gamma v)$ for various values of v . The former function, $G_0(\gamma, \gamma v)$, can be found analytically (see Equation (A1.9) of Bond & Efstathiou 1987). For G_1 , we need to integrate Equation (B5) numerically.
4. Compute $\bar{u} = G_1/G_0$. For the above example, we find $\bar{u} = 1.596, 1.831, 3.206$, and 5.579 for $v = 0, 1, 5$, and 10 , respectively.
5. Choose a threshold peak height v_t , and compute the mean surface number density of peaks, \bar{n}_{pk} , from Equation (A1.9) of Bond & Efstathiou (1987):

$$\bar{n}_{\text{pk}}(v_t) = \frac{\sigma_2^2}{(2\pi)^{3/2}(2\sigma_1^2)} \int dv e^{-v^2/2} G_0(\gamma, \gamma v). \quad (\text{B15})$$

The integration boundary is taken from v_t to $+\infty$ for temperature hot spots, and from $-\infty$ to $-|v_t|$ for temperature cold spots. For the above example, we find $4\pi\bar{n}_{\text{pk}} = 15354.5, 8741.5, 2348.9$, and 247.5 for $v_t = 0, 1, 2$, and 3 , respectively.

6. Compute b_v and b_ζ from Equation (B3) for various values of v .
7. Average b_v and b_ζ over v . We calculate the averaged bias parameters, \bar{b}_v and \bar{b}_ζ , by integrating b_v and b_ζ multiplied by the number density of peaks for a given v . We then divide

⁴³ We used the five-year best-fitting power spectrum to calculate the predicted polarization pattern (before the seven-year parameter were obtained) and compare it to the seven-year polarization data.

the integral by the mean number density of peaks, \bar{n}_{pk} , to find

$$\bar{b}_v = \frac{1}{\bar{n}_{\text{pk}}(v_t)} \frac{\sigma_2^2}{(2\pi)^{3/2}(2\sigma_1^2)} \int dv e^{-v^2/2} G_0(\gamma, \gamma v) b_v, \quad (\text{B16})$$

$$\bar{b}_\zeta = \frac{1}{\bar{n}_{\text{pk}}(v_t)} \frac{\sigma_2^2}{(2\pi)^{3/2}(2\sigma_1^2)} \int dv e^{-v^2/2} G_0(\gamma, \gamma v) b_\zeta. \quad (\text{B17})$$

The integration boundary is taken from v_t to $+\infty$ for temperature hot spots, and from $-\infty$ to $-|v_t|$ for temperature cold spots. For the above example, we find $(\bar{b}_v, \bar{b}_\zeta) = (3.289 \times 10^{-3}, 6.039 \times 10^{-7}), (1.018 \times 10^{-2}, 5.393 \times 10^{-7}), (2.006 \times 10^{-2}, 4.569 \times 10^{-7})$, and $(3.128 \times 10^{-2}, 3.772 \times 10^{-7})$ for $v_t = 0, 1, 2$, and 3 , respectively (all in units of μK^{-1}). The larger the peak height is, the larger the linear bias and the smaller the scale-dependent bias becomes.

8. Use \bar{b}_v and \bar{b}_ζ in Equations (B12) and (B13) to compute $\langle Q_r \rangle(\theta)$ and $\langle U_r \rangle(\theta)$ for a given set of C_l^{TE} and C_l^{TB} , respectively.

Very roughly speaking, the bias takes on the following values:

$$\bar{b}(l) \equiv \bar{b}_v + \bar{b}_\zeta l^2 \sim \begin{cases} \frac{0.3}{100 \mu\text{K}} [1 + (\frac{l}{75})^2] & (\text{for } v_t = 0) \\ \frac{3}{100 \mu\text{K}} [1 + (\frac{l}{290})^2] & (\text{for } v_t = 3) \end{cases}. \quad (\text{B18})$$

The scale dependence of bias becomes important at $l \sim 75$ for $v_t = 0$, but the higher peaks are closer to having a linear bias on large scales. One may also rewrite this using the stacked temperature values at the center, $\langle T \rangle(0) = (107.0, 151.4, 216.4, 292.1) \mu\text{K}$ for $v_t = 0, 1, 2$, and 3 :

$$\bar{b}(l) \simeq \frac{(0.35, 1.5, 4.3, 9.1)}{(107, 151, 216, 292) \mu\text{K}} \left[1 + \left(\frac{l}{(74, 137, 219, 288)} \right)^2 \right]. \quad (\text{B19})$$

APPENDIX C

OPTIMAL ESTIMATOR FOR SZ STACKING

C.1. Optimal Estimator

In this appendix, we describe an optimal likelihood-based method for estimating the stacked SZ profile around clusters whose locations are taken from external catalogs.

Formally, we can set up the problem as follows. We represent the *WMAP* data as a vector of length $(N_{\text{chan}} \times N_{\text{pix}})$ and denote it by d_{vp} , where the index $v = 1, \dots, N_{\text{chan}}$ ranges over channels, and the index $p = 1, \dots, N_{\text{pix}}$ ranges over sky pixels. (We typically take $N_{\text{chan}} = 6$ corresponding to V1, V2, W1, W2, W3, and W4; and $N_{\text{pix}} = 12(2^{10})^2$ corresponding to a HEALPix resolution of $N_{\text{side}} = 1024$.) We model the *WMAP* data as a sum of CMB, noise, and SZ contributions as follows:

$$d_{vp} = \sum_{\ell m} A_{vp, \ell m} a_{\ell m} + n_{vp} + \sum_{\alpha=1}^{N_{\text{tmp}}} p_\alpha(t_\alpha)_{vp}. \quad (\text{C1})$$

In this equation, we have written the SZ contribution as a sum of N_{tmp} template maps, $t_1, \dots, t_{N_{\text{tmp}}}$, whose coefficients p_α

are free parameters to be determined. The operator, $A_{vp,\ell m}$, in Equation (C1) converts a harmonic-space CMB realization, $a_{\ell m}$, into a set of maps with black-body frequency dependence and channel-dependent beam convolution. More formally, the matrix element $A_{vp,\ell m}$ is defined by

$$A_{vp,\ell m} = b_{v\ell} Y_{\ell m}(p), \quad (\text{C2})$$

where $b_{v\ell}$ is the beam transfer function (including HEALPix window function) for channel v .

The specific form of the template maps, t_α , will depend on the type of profile reconstruction which is desired. For example, if we want to estimate a stacked amplitude for the SZ signal in N angular bins, we define one template for each bin. If the bin corresponds to angular range $\theta_{\min} \leq \theta \leq \theta_{\max}$, we define a map m_p which is $=1$ if the angular distance θ between pixel p and *some* galaxy cluster in the catalog is in the range $\theta_{\min} \leq \theta \leq \theta_{\max}$, and zero otherwise. We convolve this map with the beam in each channel v and multiply by the SZ frequency dependence to obtain the template t_{vp} . As another example, if we want to fit for an overall multiple of a fiducial model m_p for the total SZ signal (summed over all clusters) then we define a single (i.e., $N_{\text{tmpl}} = 1$) template t_{vp} by applying beam convolution and the SZ frequency dependence for each channel v .

Given this setup, we would like to compute the likelihood function $\mathcal{L}[p_\alpha | d_{vp}]$ for the profile p_α , given the noisy data d_{vp} , marginalizing over the CMB realization. We assume a fixed fiducial model C_ℓ and represent the CMB signal covariance by a (diagonal) matrix S_{harm} in harmonic space:

$$(S_{\text{harm}})_{\ell m, \ell' m'} = C_\ell \delta_{\ell \ell'} \delta_{mm'}. \quad (\text{C3})$$

We represent the noise covariance by an (also diagonal) pixel-matrix $N_{vp,v'p'}$:

$$(N_{\text{pix}})_{vp,v'p'} = \sigma_{vp}^2 \delta_{vv'} \delta_{pp'}. \quad (\text{C4})$$

The joint (CMB, SZ) likelihood function can now be written (up to an overall normalizing constant) as

$$\begin{aligned} \mathcal{L}[a, p | d] \propto & \exp \left[-\frac{1}{2} a^T S_{\text{harm}}^{-1} a - \frac{1}{2} (d - Aa - p_\alpha t_\alpha)^T N^{-1} \right. \\ & \times (d - Aa - p_\alpha t_\alpha) \Big]. \end{aligned} \quad (\text{C5})$$

(In this equation we have omitted some indexes for notational compactness, e.g., $d_{vp} \rightarrow d$ and $a_{\ell m} \rightarrow a$. The summation over α is assumed.) We can now integrate out the CMB realization a to obtain the marginalized likelihood for the profile:

$$\mathcal{L}[p | d] = \int Da \mathcal{L}[a, p | d] \quad (\text{C6})$$

$$\propto \exp \left[-\frac{1}{2} (p_\alpha - \hat{p}_\alpha)^T F_{\alpha\beta} (p_\beta - \hat{p}_\beta) \right], \quad (\text{C7})$$

where we have defined the (N_{tmpl})-by-(N_{tmpl}) matrix

$$F_{\alpha\beta} = (t_\alpha)_{v'p'} [N_{\text{pix}} + AS_{\text{harm}}A^T]_{v'p', vp}^{-1}, \quad (\text{C8})$$

and the length-(N_{tmpl}) vector

$$\hat{p}_\alpha = F_{\alpha\beta}^{-1} (t_\beta)_{v'p'} [N_{\text{pix}} + AS_{\text{harm}}A^T]_{v'p', vp}^{-1} d_{vp}. \quad (\text{C9})$$

The likelihood function $\mathcal{L}[p | d]$ in Equation (C7) has a simple interpretation. The likelihood for p_α is a Gaussian with mean \hat{p}_α and covariance matrix $F_{\alpha\beta}^{-1}$. This is the main result of this section and is the basis for all our SZ results in the body of the paper. For example, when we reconstruct the stacked SZ profile in angular bins, the estimated profile in each bin α is given by \hat{p}_α and the 1σ error is given by $\sqrt{(F^{-1})_{\alpha\alpha}}$.

It is worth mentioning that the statistic \hat{p}_α also appears naturally if we use an estimator framework rather than a likelihood formalism. If we think of \hat{p}_α , defined by Equation (C9), as an estimator for the profile given the data d , then one can verify that the estimator is unbiased (i.e., $\langle \hat{p}_\alpha \rangle = p_\alpha$, where the expectation value is taken over random CMB + noise realizations with a fixed SZ contribution) and its covariance is $F_{\alpha\beta}^{-1}$. Conversely, it is not hard to show that \hat{p}_α is the unbiased estimator with minimum variance, thus obtaining \hat{p}_α in a different way. This alternate derivation also shows that the error bars on the profile obtained in our likelihood formalism are the same as would be obtained in a direct Monte Carlo treatment.

Either from the likelihood or estimator formalism, one sees that the statistic \hat{p}_α is optimal. In the limit where all frequency channels are in the Rayleigh-Jeans regime, the statistic \hat{p}_α corresponds to C^{-1} -filtering the data and multiplying by each template map. In this case, the C^{-1} filter acts as a high-pass filter which optimally suppresses CMB power on scales larger than the clusters, and also optimally weights the channels (in a way which is ℓ -dependent if the beams differ). When channels with higher frequency are included, the statistic \hat{p}_α would get most of its information from linear combinations of channels which contain zero CMB signal, but nonzero response to an SZ signal. (Such a combination of channels does not need to be high-pass filtered, increasing its statistical weight.)

For the V + W combination in *WMAP*, the N^{-1} -filtered (V – W) null map is used to separate the SZ effect and CMB, as CMB is canceled in this map while the SZ is effect not.

We conclude with a few comments on implementation. Inspection of Equations (C8) and (C9) shows that it would be straightforward to compute $F_{\alpha\beta}$ and \hat{p}_α , given an algorithm for multiplying a set of N_{chan} pixel space maps d_{vp} by the operator $[N_{\text{pix}} + AS_{\text{harm}}A^T]^{-1}$. A fast multigrid-based algorithm for this inverse problem was found in Smith et al. (2007) but there is one small wrinkle in the implementation: in Smith et al. (2007) the problem was formulated in harmonic space and an algorithm was given for multiplying by the operator $[S_{\text{harm}}^{-1} + A^T N_{\text{pix}}^{-1} A]^{-1}$. However, the matrix identity

$$[N_{\text{pix}} + AS_{\text{harm}}A^T]^{-1} = N_{\text{pix}}^{-1} - A [S_{\text{harm}}^{-1} + A^T N_{\text{pix}}^{-1} A]^{-1} A^T, \quad (\text{C10})$$

allows us to relate the two inverse problems. In fact, there is another advantage to using the expression on the right-hand side of Equation (C10): because the inverse noise, N_{pix}^{-1} , appears instead of the noise covariance N_{pix} , a galactic mask can be straightforwardly included in the analysis by zeroing the matrix entries of N_{pix}^{-1} which correspond to masked pixels, so that the pixels are treated as infinitely noisy.

APPENDIX D

PRESSURE PROFILES

D.1. Pressure Profile from X-ray Observations

Recently, Arnaud et al. (2010) found that the following parameterized phenomenological electron pressure profile, which

is based on a “generalized Navarro–Frenk–White profile” proposed by Nagai et al. (2007), fits the electron pressure profiles directly derived from X-ray data of clusters well (see Equation (13) of Arnaud et al. 2010):

$$P_e(r) = 1.65(h/0.7)^2 \text{eVcm}^{-3} \times E^{8/3}(z) \left[\frac{M_{500}}{3 \times 10^{14}(0.7/h) M_\odot} \right]^{2/3+\alpha_p} p(r/r_{500}), \quad (\text{D1})$$

where $\alpha_p = 0.12$, $E(z) \equiv H(z)/H_0 = [\Omega_m(1+z)^3 + \Omega_\Lambda]^{1/2}$ for a Λ CDM model, r_{500} is the radius within which the mean overdensity is 500 times the critical density of the universe, $\rho_c(z) = 2.775 \times 10^{11} E^2(z) h^2 M_\odot \text{Mpc}^{-3}$, and M_{500} is the mass enclosed within r_{500} :

$$M_{500} \equiv \frac{4\pi}{3} [500\rho_c(z)] r_{500}^3. \quad (\text{D2})$$

The function $p(x)$ is defined by

$$p(x) \equiv \frac{8.403(0.7/h)^{3/2}}{(c_{500}x)^\gamma [1 + (c_{500}x)^\alpha]^{(\beta-\gamma)/\alpha}}, \quad (\text{D3})$$

where $c_{500} = 1.177$, $\alpha = 1.051$, $\beta = 5.4905$, and $\gamma = 0.3081$.

The SPT Collaboration stacked the SZ maps of 11 known clusters and fitted the stacked SZ radial profile to the above form, finding $c_{500} = 1.0$, $\alpha = 1.0$, $\beta = 5.5$, and $\gamma = 0.5$ (Plagge et al. 2010). While they did not compare the overall amplitude (which is the focus of our analysis), the shape of the pressure profile found by the SPT Collaboration (using the SZ data) is in an excellent agreement with that found by Arnaud et al. (2010, using the X-ray data).

D.2. Pressure Profile from Hydrostatic Equilibrium

The KS profile builds on and extends the idea originally put forward by Makino et al. (1998) and Suto et al. (1998): (1) gas is in hydrostatic equilibrium with gravitational potential given by an NFW dark matter density profile (Navarro et al. 1997) and (2) the equation of state of gas is given by a polytropic form, $P \propto \rho^\gamma$. However, this model still contains two free parameters: a polytropic index γ and the normalization of P . Komatsu & Seljak (2001) found that an additional, physically reasonable assumption that (3) the slope of the gas density profile and that of the dark matter density profile agree at around the virial radius, uniquely fixes γ , leaving only one free parameter: the normalization of P . These assumptions are supported by hydrodynamical simulations of clusters of galaxies, and the resulting shape of the KS profile indeed agrees with simulations reasonably well (see, however, Section 7.8 for a discussion on the shape of the profile in the outer parts of clusters).

Determining the normalization of the KS profile requires an additional assumption, described below. Also note that this model does not take into account any non-thermal pressure (such as ρv^2 where v is the bulk or turbulent velocity), gas cooling, or star formation (see, e.g., Bode et al. 2009; Frederiksen et al. 2009, and references therein for various attempts to incorporate more gas physics).

The KS gas pressure profile is given by (see Section 3.3 of Komatsu & Seljak 2002, for more detailed descriptions)

$$P_{\text{gas}}(r) = P_{\text{gas}}(0)[y_{\text{gas}}(r/r_s)]^\gamma. \quad (\text{D4})$$

The electron pressure profile, P_e , is then given by $P_e = [(2+2X)/(3+5X)]P_{\text{gas}} = 0.518P_{\text{gas}}$ for $X = 0.76$. Here, r_s

is the so-called scale radius of the NFW profile, and a function $y_{\text{gas}}(x)$ is defined by

$$y_{\text{gas}}(x) \equiv \left\{ 1 - B \left[1 - \frac{\ln(1+x)}{x} \right] \right\}^{1/(\gamma-1)}, \quad (\text{D5})$$

with

$$B \equiv 3\eta^{-1}(0) \frac{\gamma-1}{\gamma} \left[\frac{\ln(1+c)}{c} - \frac{1}{1+c} \right]^{-1}, \quad (\text{D6})$$

$$\gamma = 1.137 + 8.94 \times 10^{-2} \ln(c/5) - 3.68 \times 10^{-3}(c-5), \quad (\text{D7})$$

and

$$\eta(0) = 2.235 + 0.202(c-5) - 1.16 \times 10^{-3}(c-5)^2. \quad (\text{D8})$$

Here, c is the so-called concentration parameter of the NFW profile, which is related to the scale radius, r_s , via $c = r_{\text{vir}}/r_s$, and r_{vir} is the virial radius. The virial radius gives the virial mass, M_{vir} , as

$$M_{\text{vir}} = \frac{4\pi}{3} [\Delta_c(z)\rho_c(z)] r_{\text{vir}}^3. \quad (\text{D9})$$

Here, $\Delta_c(z)$ depends on Ω_m and Ω_Λ as (Bryan & Norman 1998)

$$\Delta_c(z) = 18\pi^2 + 82[\Omega(z)-1] - 39[\Omega(z)-1]^2, \quad (\text{D10})$$

where $\Omega(z) = \Omega_m(1+z)^3/E^2(z)$ (also see Lacey & Cole 1993; Nakamura & Suto 1997, for other fitting formulae). For $\Omega_m = 0.277$, one finds $\Delta_c(0) \simeq 98$.

The central gas pressure, $P_{\text{gas}}(0)$, is given by

$$P_{\text{gas}}(0) = 55.0h^2 \text{eVcm}^{-3} \left[\frac{\rho_{\text{gas}}(0)}{10^{14}h^2 M_\odot \text{Mpc}^{-3}} \right] \left[\frac{k_B T_{\text{gas}}(0)}{8 \text{keV}} \right], \quad (\text{D11})$$

where k_B is the Boltzmann constant. The central gas temperature, $T_{\text{gas}}(0)$, is given by

$$k_B T_{\text{gas}}(0) = 8.80 \text{keV} \eta(0) \left[\frac{M_{\text{vir}}/(10^{15} h^{-1} M_\odot)}{r_{\text{vir}}/(1 h^{-1} \text{Mpc})} \right]. \quad (\text{D12})$$

The central gas density, $\rho_{\text{gas}}(0)$, will be determined such that the gas density at the virial radius is the cosmic mean baryon fraction, Ω_b/Ω_m , times the dark matter density at the same radius. This is an assumption. In fact, the cosmic mean merely provides an upper limit on the baryon fraction of clusters, and thus we expect the gas pressure to be less than what is given here. How much less needs to be determined from observations (or possibly from more detailed modeling of the intracluster medium). In any case, with this assumption, we find

$$\begin{aligned} \rho_{\text{gas}}(0) &= 7.96 \times 10^{13} h^2 M_\odot \text{Mpc}^{-3} \\ &\times \left(\frac{\Omega_b}{\Omega_m} \right) \frac{M_{\text{vir}}/(10^{15} h^{-1} M_\odot)}{[r_{\text{vir}}/(1 h^{-1} \text{Mpc})]^3} \\ &\times \frac{c^2}{(1+c)^2} \frac{1}{y_{\text{gas}}(c)} \left[\ln(1+c) - \frac{c}{1+c} \right]^{-1}. \end{aligned} \quad (\text{D13})$$

This equation fixes a typo in Equation (21) of Komatsu & Seljak (2002).

The virial radius, r_{vir} , is approximately given by $2r_{500}$; thus, M_{vir} is approximately given by $8\Delta_c/500 \simeq 1.6$. However, the

exact relation depends on the mass (see, e.g., Figure 1 of Komatsu & Seljak 2001). We calculate the mass within a given radius, r , by integrating the NFW density profile (Navarro et al. 1997):

$$\rho_{\text{NFW}}(r) = \frac{\rho_s}{(r/r_s)(1+r/r_s)^2}. \quad (\text{D14})$$

Specifically, for a given M_{500} and r_{500} , we solve the following nonlinear equation for M_{vir} :

$$M_{\text{vir}} \frac{m(cr_{500}/r_{\text{vir}})}{m(c)} = M_{500}, \quad (\text{D15})$$

where $m(x) \equiv \ln(1+x) - x/(1+x)$. Here, r_{vir} is related to M_{vir} via Equation (D9). We also need a relation between the concentration parameter, c , and M_{vir} . Komatsu & Seljak (2002) used

$$\begin{aligned} c_{\text{seljak}} &= \frac{10}{1+z} \left(\frac{M_{\text{vir}}}{3.42 \times 10^{12} h^{-1} M_\odot} \right)^{-0.2} \\ &= \frac{5.09}{1+z} \left(\frac{M_{\text{vir}}}{10^{14} h^{-1} M_\odot} \right)^{-0.2}, \end{aligned} \quad (\text{D16})$$

which was adopted from Seljak (2000).

Recently, Duffy et al. (2008) ran large N -body simulations with the *WMAP* five-year cosmological parameters to find a more accurate fitting formula for the concentration parameter:

$$\begin{aligned} c_{\text{duffy}} &= \frac{7.85}{(1+z)^{0.71}} \left(\frac{M_{\text{vir}}}{2 \times 10^{12} h^{-1} M_\odot} \right)^{-0.081} \\ &= \frac{5.72}{(1+z)^{0.71}} \left(\frac{M_{\text{vir}}}{10^{14} h^{-1} M_\odot} \right)^{-0.081}. \end{aligned} \quad (\text{D17})$$

This formula makes clusters of galaxies ($M_\odot \gtrsim 10^{14} M_\odot$) more concentrated than c_{seljak} would predict.

REFERENCES

- Abbott, B. P., et al. 2009, *Nature*, **460**, 990
 Abdalla, F. B., & Rawlings, S. 2007, *MNRAS*, **381**, 1313
 Ackerman, L., Carroll, S. M., & Wise, M. B. 2007, *Phys. Rev. D*, **75**, 083502
 Acquaviva, V., Bartolo, N., Matarrese, S., & Riotto, A. 2003, *Nucl. Phys.*, **B667**, 119
 Afshordi, N., Lin, Y.-T., Nagai, D., & Sanderson, A. J. R. 2007, *MNRAS*, **378**, 293
 Afshordi, N., Lin, Y.-T., & Sanderson, A. J. R. 2005, *ApJ*, **629**, 1
 Aguirre, A. N. 2000, *ApJ*, **533**, 1
 Albrecht, A., & Steinhardt, P. J. 1982, *Phys. Rev. Lett.*, **48**, 1220
 Alishahiha, M., Silverstein, E., & Tong, D. 2004, *Phys. Rev. D*, **70**, 123505
 Allen, S. W., Rapetti, D. A., Schmidt, R. W., Ebeling, H., Morris, R. G., & Fabian, A. C. 2008, *MNRAS*, **383**, 879
 Amarzguioui, M., Elgaroy, Ø., Mota, D. F., & Multamäki, T. 2006, *A&A*, **454**, 707
 Amin, M. A., Wagoner, R. V., & Blandford, R. D. 2008, *MNRAS*, **390**, 131
 Arkani-Hamed, N., Creminelli, P., Mukohiyama, S., & Zaldarriaga, M. 2004, *J. Cosmol. Astropart. Phys.*, **JCAP04(2004)001**
 Arnaud, M., Pointecouteau, E., & Pratt, G. W. 2005, *A&A*, **441**, 893
 Arnaud, M., Pointecouteau, E., & Pratt, G. W. 2007, *A&A*, **474**, L37
 Arnaud, M., Pratt, G. W., Piffaretti, R., Böhringer, H., Croston, J. H., & Pointecouteau, E. 2010, *A&A*, **517**, A92
 Arvanitaki, A., Dimopoulos, S., Dubovsky, S., Kaloper, N., & March-Russell, J. 2010, *Phys. Rev. D*, **81**, 123530
 Asplund, M., Grevesse, N., Sauval, A. J., & Scott, P. 2009, *ARA&A*, **47**, 481
 Atrio-Barandela, F., Kashlinsky, A., Kocevski, D., & Ebeling, H. 2008, *ApJ*, **675**, L57
 Atrio-Barandela, F., & Mücke, J. P. 1999, *ApJ*, **515**, 465
 Babich, D. 2005, *Phys. Rev. D*, **72**, 043003
 Babich, D., Creminelli, P., & Zaldarriaga, M. 2004, *J. Cosmol. Astropart. Phys.*, **JCAP08(2004)009**
 Bardeen, J. M. 1980, *Phys. Rev. D*, **22**, 1882
 Bardeen, J. M., Bond, J. R., Kaiser, N., & Szalay, A. S. 1986, *ApJ*, **304**, 15
 Bardeen, J. M., Steinhardt, P. J., & Turner, M. S. 1983, *Phys. Rev. D*, **28**, 679
 Bartolo, N., Komatsu, E., Matarrese, S., & Riotto, A. 2004, *Phys. Rep.*, **402**, 103
 Bartolo, N., & Liddle, A. R. 2002, *Phys. Rev. D*, **65**, 121301
 Bartolo, N., Matarrese, S., & Riotto, A. 2006, *J. Cosmol. Astropart. Phys.*, **JCAP06(2006)024**
 Bartolo, N., Matarrese, S., & Riotto, A. 2007, *J. Cosmol. Astropart. Phys.*, **JCAP01(2007)019**
 Basko, M. M., & Polnarev, A. G. 1980, *MNRAS*, **191**, 207
 Bassett, B. A., Tsujikawa, S., & Wands, D. 2006, *Rev. Mod. Phys.*, **78**, 537
 Battistelli, E. S., et al. 2003, *ApJ*, **598**, L75
 Bean, R., Bernat, D., Pogosian, L., Silvestri, A., & Trodden, M. 2007, *Phys. Rev. D*, **75**, 064020
 Bean, R., Dunkley, J., & Pierpaoli, E. 2006, *Phys. Rev. D*, **74**, 063503
 Beltran, M., Garcia-Bellido, J., & Lesgourgues, J. 2007, *Phys. Rev. D*, **75**, 103507
 Bennett, C. L., et al. 1996, *ApJ*, **464**, L1
 Bennett, C. L., et al. 2003a, *ApJ*, **583**, 1
 Bennett, C. L., et al. 2003b, *ApJS*, **148**, 1
 Bennett, C. L., et al. 2003c, *ApJS*, **148**, 97
 Bennett, C. L., et al. 2011, *ApJS*, **192**, 17
 Bertschinger, E., & Zukin, P. 2008, *Phys. Rev. D*, **78**, 024015
 Bielby, R. M., & Shanks, T. 2007, *MNRAS*, **382**, 1196
 Birkshire, M. 1999, *Phys. Rep.*, **310**, 97
 Bode, P., Ostriker, J. P., & Vikhlinin, A. 2009, *ApJ*, **700**, 989
 Böhringer, H., et al. 2004, *A&A*, **425**, 367
 Böhringer, H., et al. 2007, *A&A*, **469**, 363
 Bonamente, M., Joy, M. K., LaRoque, S. J., Carlstrom, J. E., Reese, E. D., & Dawson, K. S. 2006, *ApJ*, **647**, 25
 Bonamente, M., Lieu, R., Joy, M. K., & Nevalainen, J. H. 2002, *ApJ*, **576**, 688
 Bond, J. R., & Efstathiou, G. 1984, *ApJ*, **285**, L45
 Bond, J. R., & Efstathiou, G. 1987, *MNRAS*, **226**, 655
 Bond, J. R., Efstathiou, G., & Tegmark, M. 1997, *MNRAS*, **291**, L33
 Bond, J. R., Frolov, A. V., Huang, Z., & Kofman, L. 2009, *Phys. Rev. Lett.*, **103**, 071301
 Bond, J. R., et al. 2005, *ApJ*, **626**, 12
 Boubekeur, L., Creminelli, P., D'Amico, G., Noreña, J., & Vernizzi, F. 2009, *J. Cosmol. Astropart. Phys.*, **JCAP08(2009)029**
 Brandbyge, J., & Hannestad, S. 2009, *J. Cosmol. Astropart. Phys.*, **JCAP05(2009)002**
 Brandbyge, J., Hannestad, S., Haugbølle, T., & Thomsen, B. 2008, *J. Cosmol. Astropart. Phys.*, **JCAP08(2008)020**
 Briel, U. G., Henry, J. P., & Böhringer, H. 1992, *A&A*, **259**, L31
 Brown, M. L., et al. 2009, *ApJ*, **705**, 978
 Bryan, G. L., & Norman, M. L. 1998, *ApJ*, **495**, 80
 Cabella, P., Natoli, P., & Silk, J. 2007, *Phys. Rev. D*, **76**, 123014
 Cabella, P., Pietroni, D., Veneziani, M., Balbi, A., Crittenden, R., de Gasperis, G., Quercellini, C., & Vittorio, N. 2010, *MNRAS*, **405**, 961
 Calabrese, E., Smidt, J., Amblard, A., Cooray, A., Melchiorri, A., Serra, P., Heavens, A., & Munshi, D. 2010, *Phys. Rev. D*, **81**, 043529
 Carlstrom, J. E., Holder, G. P., & Reese, E. D. 2002, *ARA&A*, **40**, 643
 Carroll, S. M. 1998, *Phys. Rev. Lett.*, **81**, 3067
 Cavalieri, A., & Fusco-Femiano, R. 1976, *A&A*, **49**, 137
 Chambers, A., & Rajantie, A. 2008, *Phys. Rev. Lett.*, **100**, 041302
 Chen, X., Huang, M.-X., Kachru, S., & Shiu, G. 2007, *J. Cosmol. Astropart. Phys.*, **JCAP01(2007)002**
 Chen, X., & Wang, Y. 2010, *Phys. Rev. D*, **81**, 063511
 Chen, X., & Wang, Y. 2010, *J. Cosmol. Astropart. Phys.*, **JCAP04(2010)027**
 Cheung, C., Creminelli, P., Fitzpatrick, A. L., Kaplan, J., & Senatore, L. 2008, *J. High Energy Phys.*, **JHEP03(2008)014**
 Chevallier, M., & Polarski, D. 2001, *Int. J. Mod. Phys.*, **D10**, 213
 Chiang, H. C., et al. 2010, *ApJ*, **711**, 1123
 Chiba, T., & Takahashi, R. 2002, *Prog. Theor. Phys.*, **107**, 625
 Chiba, T., & Takahashi, R. 2007, *Phys. Rev. D*, **75**, 101301
 Chu, M., Eriksen, H. K., Knox, L., Górski, K. M., Jewell, J. B., Larson, D. L., O'Dwyer, I. J., & Wandelt, B. D. 2005, *Phys. Rev. D*, **71**, 103002
 Coe, D., & Moustakas, L. A. 2009, *ApJ*, **706**, 45
 Copeland, E. J., & Kibble, T. W. B. 2009, *Phys. Rev. D*, **80**, 123523
 Corasaniti, P. S., & Melchiorri, A. 2008, *Phys. Rev. D*, **77**, 103507
 Coulson, D., Crittenden, R. G., & Turok, N. G. 1994, *Phys. Rev. Lett.*, **73**, 2390
 Creminelli, P., Nicolis, A., Senatore, L., Tegmark, M., & Zaldarriaga, M. 2006, *J. Cosmol. Astropart. Phys.*, **JCAP05(2006)004**
 Creminelli, P., Senatore, L., Zaldarriaga, M., & Tegmark, M. 2007, *J. Cosmol. Astropart. Phys.*, **JCAP03(2007)005**

- Creminelli, P., & Zaldarriaga, M. 2004, *J. Cosmol. Astropart. Phys.*, **JCAP10(2004)006**
- Crittenden, R. G., Coulson, D., & Turok, N. G. 1995, *Phys. Rev. D*, **52**, 5402
- Cyburt, R. H., Fields, B. D., Olive, K. A., & Skillman, E. 2005, *Astropart. Phys.*, **23**, 313
- Damour, T., & Vilenkin, A. 2000, *Phys. Rev. Lett.*, **85**, 3761
- Damour, T., & Vilenkin, A. 2001, *Phys. Rev. D*, **64**, 064008
- Daniel, S. F., Caldwell, R. R., Cooray, A., & Melchiorri, A. 2008, *Phys. Rev. D*, **77**, 103513
- Davis, T. M., et al. 2007, *ApJ*, **666**, 716
- De Petris, M., et al. 2002, *ApJ*, **574**, L119
- Desjacques, V. 2008, *Phys. Rev. D*, **78**, 103503
- Diego, J. M., & Partridge, B. 2010, *MNRAS*, **402**, 1179
- Dobke, B. M., King, L. J., Fassnacht, C. D., & Auger, M. W. 2009, *MNRAS*, **397**, 311
- Doré, O., et al. 2007, arXiv:[0712.1599](#)
- Duffy, A. R., Schaye, J., Kay, S. T., & Dalla Vecchia, C. 2008, *MNRAS*, **390**, L64
- Dunkley, J., et al. 2009, *ApJS*, **180**, 306
- Dvali, G., Gruzinov, A., & Zaldarriaga, M. 2004a, *Phys. Rev. D*, **69**, 083505
- Dvali, G., Gruzinov, A., & Zaldarriaga, M. 2004b, *Phys. Rev. D*, **69**, 023505
- Easter, R., & McAllister, L. 2006, *J. Cosmol. Astropart. Phys.*, **JCAP05(2006)018**
- Ebeling, H., Edge, A. C., Allen, S. W., Crawford, C. S., Fabian, A. C., & Huchra, J. P. 2000, *MNRAS*, **318**, 333
- Ebeling, H., Edge, A. C., Boehringer, H., Allen, S. W., Crawford, C. S., Fabian, A. C., Voges, W., & Huchra, J. P. 1998, *MNRAS*, **301**, 881
- Ebeling, H., Voges, W., Boehringer, H., Edge, A. C., Huchra, J. P., & Briel, U. G. 1996, *MNRAS*, **281**, 799
- Eisenstein, D. J., & Hu, W. 1998, *ApJ*, **496**, 605
- Eisenstein, D. J., et al. 2005, *ApJ*, **633**, 560
- Elgarøy, O., & Multamäki, T. 2007, *A&A*, **471**, 65
- Enqvist, K., Jokinen, A., Mazumdar, A., Multamäki, T., & Väihkönen, A. 2005, *Phys. Rev. Lett.*, **94**, 161301
- Eriksen, H. K., Banday, A. J., Górski, K. M., Hansen, F. K., & Lilje, P. B. 2007a, *ApJ*, **660**, L81
- Eriksen, H. K., Hansen, F. K., Banday, A. J., Górski, K. M., & Lilje, P. B. 2004, *ApJ*, **605**, 14
- Eriksen, H. K., Huey, G., Banday, A. J., Górski, K. M., Jewell, J. B., O'Dwyer, I. J., & Wandelt, B. D. 2007b, *ApJ*, **665**, L1
- Fabian, A. C. 1994, *ARA&A*, **32**, 277
- Fadely, R., Keeton, C. R., Nakajima, R., & Bernstein, G. M. 2010, *ApJ*, **711**, 246
- Falk, T., Rangarajan, R., & Srednicki, M. 1993, *ApJ*, **403**, L1
- Fang, W., Hu, W., & Lewis, A. 2008, *Phys. Rev. D*, **78**, 087303
- Fassnacht, C. D., Womble, D. S., Neugebauer, G., Browne, I. W. A., Readhead, A. C. S., Matthews, K., & Pearson, T. J. 1996, *ApJ*, **460**, L103
- Feng, B., Li, H., Li, M.-Z., & Zhang, X.-M. 2005, *Phys. Lett. B*, **620**, 27
- Feng, B., Li, M., Xia, J.-Q., Chen, X., & Zhang, X. 2006, *Phys. Rev. Lett.*, **96**, 221302
- Finelli, F., Hamann, J., Leach, S. M., & Lesgourgues, J. 2010, *J. Cosmol. Astropart. Phys.*, **JCAP04(2010)011**
- Finoguenov, A., Böhringer, H., Osmond, J. P. F., Ponman, T. J., Sanderson, A. J. R., Zhang, Y., & Zimer, M. 2005a, *Adv. Space Res.*, **36**, 622
- Finoguenov, A., Böhringer, H., & Zhang, Y. 2005b, *A&A*, **442**, 827
- Finoguenov, A., Ponman, T. J., Osmond, J. P. F., & Zimer, M. 2007, *MNRAS*, **374**, 737
- Fosalba, P., Gaztañaga, E., & Castander, F. J. 2003, *ApJ*, **597**, L89
- Fowler, J. W., et al. 2010, *ApJ*, **722**, 1148
- Frederiksen, T. F., Hansen, S. H., Host, O., & Roncadelli, M. 2009, *ApJ*, **700**, 1603
- Freedman, W. L., et al. 2001, *ApJ*, **553**, 47
- Frieman, J. A., Turner, M. S., & Huterer, D. 2008, *ARA&A*, **46**, 385
- Fu, L., et al. 2008, *A&A*, **479**, 9
- Fukugita, M., Futamase, T., & Kasai, M. 1990, *MNRAS*, **246**, 24P
- Fukugita, M., & Kawasaki, M. 2006, *ApJ*, **646**, 691
- Futamase, T., & Yoshida, S. 2001, *Prog. Theor. Phys.*, **105**, 887
- Gangui, A., Lucchin, F., Matarrese, S., & Mollerach, S. 1994, *ApJ*, **430**, 447
- Gold, B., et al. 2009, *ApJS*, **180**, 265
- Gold, B., et al. 2011, *ApJS*, **192**, 15
- Goldberg, D. M., & Spergel, D. N. 1999, *Phys. Rev. D*, **59**, 103002
- Gorski, K. M., Hivon, E., Banday, A. J., Wandelt, B. D., Hansen, F. K., Reinecke, M., & Bartlemann, M. 2005, *ApJ*, **622**, 759
- Groeneboom, N. E., Ackerman, L., Kathrine Wehus, I., & Eriksen, H. K. 2010, *ApJ*, **722**, 452
- Gruenwald, R., Steigman, G., & Viegas, S. M. 2002, *ApJ*, **567**, 931
- Gubitosi, G., Pagano, L., Amelino-Camelia, G., Melchiorri, A., & Cooray, A. 2009, *J. Cosmol. Astropart. Phys.*, **JCAP08(2009)021**
- Guth, A. H. 1981, *Phys. Rev. D*, **23**, 347
- Guth, A. H., & Pi, S. Y. 1982, *Phys. Rev. Lett.*, **49**, 1110
- Guy, J., et al. 2007, *A&A*, **466**, 11
- Haiman, Z., Mohr, J. J., & Holder, G. P. 2001, *ApJ*, **553**, 545
- Hamann, J., Shafieloo, A., & Souradeep, T. 2010, *J. Cosmol. Astropart. Phys.*, **JCAP04(2010)010**
- Hannestad, S. 2005, *Phys. Rev. Lett.*, **95**, 221301
- Hannestad, S., & Wong, Y. Y. Y. 2007, *J. Cosmol. Astropart. Phys.*, **JCAP07(2007)004**
- Hanson, D., & Lewis, A. 2009, *Phys. Rev. D*, **80**, 063004
- Hanson, D., Smith, K. M., Challinor, A., & Liguori, M. 2009, *Phys. Rev. D*, **80**, 083004
- Harari, D. D., & Zaldarriaga, M. 1993, *Phys. Lett. B*, **319**, 96
- Hawking, S. W. 1982, *Phys. Lett. B*, **115**, 295
- Herbig, T., Lawrence, C. R., Readhead, A. C. S., & Gulkis, S. 1995, *ApJ*, **449**, L5
- Hernández-Monteagudo, C., & Rubino-Martín, J. A. 2004, *MNRAS*, **347**, 403
- Hernández-Monteagudo, C., Genova-Santos, R., & Atrio-Barandela, F. 2004, *ApJ*, **613**, L89
- Herranz, D., Sanz, J. L., Hobson, M. P., Barreiro, R. B., Diego, J. M., Martínez-González, E., & Lasenby, A. N. 2002, *MNRAS*, **336**, 1057
- Hertzberg, M. P., Tegmark, M., & Wilczek, F. 2008, *Phys. Rev. D*, **78**, 083507
- Hicken, M., Wood-Vasey, W. M., Blondin, S., Challis, P., Jha, S., Kelly, P. L., Rest, A., & Kirshner, R. P. 2009a, *ApJ*, **700**, 1097
- Hicken, M., et al. 2009b, *ApJ*, **700**, 331
- Hincks, A. D., et al. 2009, arXiv:[0907.0461](#)
- Hinshaw, G., et al. 2007, *ApJS*, **170**, 288
- Hinshaw, G., et al. 2009, *ApJS*, **180**, 225
- Hirabayashi, H., et al. 2000, *PASJ*, **52**, 997
- Holman, R., & Tolley, A. J. 2008, *J. Cosmol. Astropart. Phys.*, **JCAP05(2008)001**
- Hu, W. 2005, in ASP Conf. Ser. 339, Observing Dark Energy, ed. S. C. Wolff & T. R. Lauer (San Francisco, CA: ASP), 215
- Hu, W. 2008, *Phys. Rev. D*, **77**, 103524
- Hu, W., Eisenstein, D. J., & Tegmark, M. 1998, *Phys. Rev. Lett.*, **80**, 5255
- Hu, W., & Sawicki, I. 2007, *Phys. Rev. D*, **76**, 104043
- Hu, W., Scott, D., Sugiyama, N., & White, M. 1995, *Phys. Rev. D*, **52**, 5498
- Hu, W., & Sugiyama, N. 1996, *ApJ*, **471**, 542
- Hu, W., & White, M. 1997, *Phys. Rev. D*, **56**, 596
- Huey, G., Cyburt, R. H., & Wandelt, B. D. 2004, *Phys. Rev. D*, **69**, 103503
- Ichikawa, K., Fukugita, M., & Kawasaki, M. 2005, *Phys. Rev. D*, **71**, 043001
- Ichikawa, K., Sekiguchi, T., & Takahashi, T. 2008, *Phys. Rev. D*, **78**, 043509
- Ichikawa, K., & Takahashi, T. 2006, *Phys. Rev. D*, **73**, 063528
- Ichiki, K., Nagata, R., & Yokoyama, J. 2010, *Phys. Rev. D*, **81**, 083010
- Ikebe, Y., Reiprich, T. H., Böhringer, H., Tanaka, Y., & Kitayama, T. 2002, *A&A*, **383**, 773
- Ishak, M., Upadhye, A., & Spergel, D. N. 2006, *Phys. Rev. D*, **74**, 043513
- Izotov, Y. I., & Thuan, T. X. 2004, *ApJ*, **602**, 200
- Jain, B., & Zhang, P. 2008, *Phys. Rev. D*, **78**, 063503
- Jarosik, N., et al. 2011, *ApJS*, **192**, 14
- Janet, F. A., et al. 2006, *ApJ*, **653**, 1571
- Jeong, D., Komatsu, E., & Jain, B. 2009, *Phys. Rev. D*, **80**, 123527
- Jewell, J., Levin, S., & Anderson, C. H. 2004, *ApJ*, **609**, 1
- Jha, S., Riess, A. G., & Kirshner, R. P. 2007, *ApJ*, **659**, 122
- Jokinen, A., & Mazumdar, A. 2006, *J. Cosmol. Astropart. Phys.*, **JCAP04(2006)003**
- Jones, W. C., et al. 2006, *ApJ*, **647**, 823
- Kain, B. 2006, *Phys. Rev. D*, **73**, 123521
- Kaiser, N. 1983, *MNRAS*, **202**, 1169
- Kaiser, N. 1984, *ApJ*, **284**, L9
- Kamionkowski, M., Kosowsky, A., & Stebbins, A. 1997a, *Phys. Rev. Lett.*, **78**, 2058
- Kamionkowski, M., Kosowsky, A., & Stebbins, A. 1997b, *Phys. Rev. D*, **55**, 7368
- Kashlinsky, A., Atrio-Barandela, F., Kocevski, D., & Ebeling, H. 2008, *ApJ*, **686**, L49
- Kawasaki, M., Moroi, T., & Yanagida, T. 1996, *Phys. Lett. B*, **383**, 313
- Kawasaki, M., & Sekiguchi, T. 2008, *Prog. Theor. Phys.*, **120**, 995
- Kawasaki, M., & Takahashi, F. 2005, *Phys. Lett. B*, **618**, 1
- Kazin, E. A., et al. 2010, *ApJ*, **710**, 1444
- Kessler, R., et al. 2009, *ApJS*, **185**, 32
- Khatri, R., & Wandelt, B. D. 2009, *Phys. Rev. D*, **79**, 023501
- Khatri, R., & Wandelt, B. D. 2010, *Phys. Rev. D*, **81**, 103518
- Kinney, W. H., Kolb, E. W., Melchiorri, A., & Riotto, A. 2008, *Phys. Rev. D*, **78**, 087302

- Kitching, T. D., Heavens, A. F., Verde, L., Serra, P., & Melchiorri, A. 2008, *Phys. Rev. D*, **77**, 103008
- Kodama, H., & Sasaki, M. 1984, *Prog. Theor. Phys. Suppl.*, **78**, 1
- Koester, B. P., et al. 2007, *ApJ*, **660**, 239
- Kogut, A., et al. 2003, *ApJS*, **148**, 161
- Komatsu, E. 2001, PhD thesis, Tohoku Univ.
- Komatsu, E., & Kitayama, T. 1999, *ApJ*, **526**, L1
- Komatsu, E., & Seljak, U. 2001, *MNRAS*, **327**, 1353
- Komatsu, E., & Seljak, U. 2002, *MNRAS*, **336**, 1256
- Komatsu, E., & Spergel, D. N. 2001, *Phys. Rev. D*, **63**, 063002
- Komatsu, E., Spergel, D. N., & Wandelt, B. D. 2005, *ApJ*, **634**, 14
- Komatsu, E., Wandelt, B. D., Spergel, D. N., Banday, A. J., & Górski, K. M. 2002, *ApJ*, **566**, 19
- Komatsu, E., et al. 2003, *ApJS*, **148**, 119
- Komatsu, E., et al. 2009a, *ApJS*, **180**, 330
- Komatsu, E., et al. 2009b, Astro2010: The Astronomy and Astrophysics Decadal Survey, Science White Papers, No. 158 (arXiv:0902.4759)
- Koopmans, L. V. E., Treu, T., Fassnacht, C. D., Blandford, R. D., & Surpi, G. 2003, *ApJ*, **599**, 70
- Kosowsky, A., & Turner, M. S. 1995, *Phys. Rev. D*, **52**, 1739
- Kostelecký, V. A., & Mewes, M. 2007, *Phys. Rev. Lett.*, **99**, 011601
- Kostelecký, V. A., & Mewes, M. 2008, *ApJ*, **689**, L1
- Kovac, J. M., Leitch, E. M., Pryke, C., Carlstrom, J. E., Halverson, N. W., & Holzapfel, W. L. 2002, *Nature*, **420**, 772
- Kowalski, M., et al. 2008, *ApJ*, **686**, 749
- Koyama, K., & Maartens, R. 2006, *J. Cosmol. Astropart. Phys.*, **JCAP01(2006)016**
- Lacey, C., & Cole, S. 1993, *MNRAS*, **262**, 627
- Landt, H., Padovani, P., Perlman, E. S., Giommi, P., Bignall, H., & Tzioumis, A. 2001, *MNRAS*, **323**, 757
- Larson, D. L., Eriksen, H. K., Wandelt, B. D., Górski, K. M., Huey, G., Jewell, J. B., & O'Dwyer, I. J. 2007, *ApJ*, **656**, 653
- Larson, D. L., et al. 2011, *ApJS*, **192**, 16
- Leauthaud, A., et al. 2010, *ApJ*, **709**, 97
- Lehners, J. 2008, *Phys. Rep.*, **465**, 223
- Lesgourgues, J., Matarrese, S., Pietroni, M., & Riotto, A. 2009, *J. Cosmol. Astropart. Phys.*, **JCAP06(2009)017**
- Lesgourgues, J., & Pastor, S. 2006, *Phys. Rep.*, **429**, 307
- Lewis, A. 2008, *Phys. Rev. D*, **78**, 023002
- Lewis, A., Challinor, A., & Lasenby, A. 2000, *ApJ*, **538**, 473
- Li, H., Xia, J., Zhao, G., Fan, Z., & Zhang, X. 2008, *ApJ*, **683**, L1
- Li, M., Wang, T., & Wang, Y. 2008, *J. Cosmol. Astropart. Phys.*, **JCAP03(2008)028**
- Liddle, A. R., & Lyth, D. H. 2000, Cosmological Inflation and Large-scale Structure (Cambridge: Cambridge Univ. Press)
- Liddle, A. R., & Lyth, D. H. 2009, The Primordial Density Perturbation: Cosmology, Inflation and the Origin of Structure (Cambridge: Cambridge Univ. Press)
- Lieu, R., Mittaz, J. P. D., & Zhang, S. 2006, *ApJ*, **648**, 176
- Lin, Y., Partridge, B., Pober, J. C., Bouchevry, K. E., Burke, S., Klein, J. N., Coish, J. W., & Huffenberger, K. M. 2009, *ApJ*, **694**, 992
- Linde, A. 2008, Inflationary Cosmology (Lect. Notes Phys., Vol. 738; Berlin: Springer), 1
- Linde, A., & Mukhanov, V. 1997, *Phys. Rev. D*, **56**, 535
- Linde, A. D. 1982, *Phys. Lett. B*, **108**, 389
- Linde, A. D. 1983, *Phys. Lett. B*, **129**, 177
- Linde, A. D. 1985, *Phys. Lett. B*, **158**, 375
- Linde, A. D. 1990, Particle Physics and Inflationary Cosmology (Chur, Switzerland: Harwood)
- Linde, A. D. 1991, *Phys. Lett. B*, **259**, 38
- Linder, E. V. 2003, *Phys. Rev. Lett.*, **90**, 091301
- Linder, E. V., & Cahn, R. N. 2007, *Astropart. Phys.*, **28**, 481
- Linder, E. V., & Jenkins, A. 2003, *MNRAS*, **346**, 573
- Liu, G.-C., Lee, S., & Ng, K.-W. 2006, *Phys. Rev. Lett.*, **97**, 161303
- Loeb, A. 2002, *New Astron.*, **7**, 279
- Loeb, A. 2007, *J. Cosmol. Astropart. Phys.*, **JCAP03(2007)001**
- Lue, A., Wang, L., & Kamionkowski, M. 1999, *Phys. Rev. Lett.*, **83**, 1506
- Lueker, M., et al. 2010, *ApJ*, **719**, 1045
- Lyth, D. H., & Rodriguez, Y. 2005, *Phys. Rev. Lett.*, **95**, 121302
- Lyth, D. H., & Stewart, E. D. 1992, *Phys. Lett. B*, **283**, 189
- Lyth, D. H., Ungarelli, C., & Wands, D. 2003, *Phys. Rev. D*, **67**, 23503
- Lyth, D. H., & Wands, D. 2003, *Phys. Rev. D*, **68**, 103516
- Mack, K. J. 2009, arXiv:0911.0421
- Mack, K. J., & Steinhardt, P. J. 2009, arXiv:0911.0418
- Makino, N., Sasaki, S., & Suto, Y. 1998, *ApJ*, **497**, 555
- Maldacena, J. M. 2003, *J. High Energy Phys.*, **JHEP05(2003)013**
- Mangano, G., et al. 2005, *Nucl. Phys. B*, **729**, 221
- Mangilli, A., & Verde, L. 2009, *Phys. Rev. D*, **80**, 123007
- Mantz, A., Allen, S. W., Ebeling, H., Rapetti, D., & Drlica-Wagner, A. 2010a, *MNRAS*, **406**, 1773
- Mantz, A., Allen, S. W., & Rapetti, D. 2010b, *MNRAS*, **406**, 1805
- Mantz, A., Allen, S. W., Rapetti, D., & Ebeling, H. 2010c, *MNRAS*, **406**, 1759
- Masi, S., et al. 2006, *A&A*, **458**, 687
- Massey, R., et al. 2007, *ApJS*, **172**, 239
- Melin, J., Bartlett, J. G., Delabrouille, J., Arnaud, M., Piffaretti, R., & Pratt, G. W. 2010, arXiv:1001.0871
- Mollerach, S., & Matarrese, S. 1997, *Phys. Rev. D*, **56**, 4494
- Montroy, T. E., et al. 2006, *ApJ*, **647**, 813
- Moroi, T., & Takahashi, T. 2001, *Phys. Lett. B*, **522**, 215
- Moroi, T., & Takahashi, T. 2002, *Phys. Rev. D*, **66**, 063501
- Moss, I. G., & Graham, C. M. 2007, *J. Cosmol. Astropart. Phys.*, **JCAP11(2007)004**
- Moss, I. G., & Xiong, C. 2007, *J. Cosmol. Astropart. Phys.*, **JCAP04(2007)007**
- Mukhanov, V. F., & Chibisov, G. V. 1981, *JETP Lett.*, **33**, 532
- Mukhanov, V. F., Feldman, H. A., & Brandenberger, R. H. 1992, *Phys. Rep.*, **215**, 203
- Munshi, D., & Heavens, A. 2010, *MNRAS*, **401**, 2406
- Munshi, D., Valageas, P., Cooray, A., & Heavens, A. 2009, arXiv:0907.3229
- Myers, A. D., Shanks, T., Outram, P. J., Frith, W. J., & Wolfendale, A. W. 2004, *MNRAS*, **347**, L67
- Myers, S. T., et al. 1995, *ApJ*, **447**, L5
- Nagai, D., Kravtsov, A. V., & Vikhlinin, A. 2007, *ApJ*, **668**, 1
- Nakamura, T. T., & Suto, Y. 1997, *Prog. Theor. Phys.*, **97**, 49
- Navarro, J. F., Frenk, C. S., & White, S. D. M. 1997, *ApJ*, **490**, 493
- Nitta, D., Komatsu, E., Bartolo, N., Matarrese, S., & Riotto, A. 2009, *J. Cosmol. Astropart. Phys.*, **JCAP05(2009)014**
- Nolta, M. R., et al. 2009, *ApJS*, **180**, 296
- O'Dwyer, I. J., et al. 2004, *ApJ*, **617**, L99
- Oguri, M. 2007, *ApJ*, **660**, 1
- Ohyama, Y., et al. 2002, *AJ*, **123**, 2903
- Olive, K. A., & Skillman, E. D. 2004, *ApJ*, **617**, 29
- Pagano, L., et al. 2009, *Phys. Rev. D*, **80**, 043522
- Page, L., et al. 2003, *ApJ*, **585**, 566
- Page, L., et al. 2007, *ApJS*, **170**, 335
- Paraficz, D., & Hjorth, J. 2009, *A&A*, **507**, L49
- Peimbert, M., Luridiana, V., & Peimbert, A. 2007, *ApJ*, **666**, 636
- Peiris, H. V., & Easther, R. 2008, *J. Cosmol. Astropart. Phys.*, **JCAP07(2008)024**
- Peiris, H. V., & Verde, L. 2010, *Phys. Rev. D*, **81**, 021302
- Peiris, H. V., et al. 2003, *ApJS*, **148**, 213
- Percival, W. J., Cole, S., Eisenstein, D. J., Nichol, R. C., Peacock, J. A., Pope, A. C., & Szalay, A. S. 2007, *MNRAS*, **381**, 1053
- Percival, W. J., et al. 2010, *MNRAS*, **401**, 2148
- Perlman, E. S., Padovani, P., Giommi, P., Sambruna, R., Jones, L. R., Tzioumis, A., & Reynolds, J. 1998, *AJ*, **115**, 1253
- Perlmutter, S., et al. 1999, *ApJ*, **517**, 565
- Piacentini, F., et al. 2006, *ApJ*, **647**, 833
- Pitrou, C. 2009a, *Class. Quantum Grav.*, **26**, 065006
- Pitrou, C. 2009b, *Gen. Rel. Grav.*, **41**, 2587
- Pitrou, C., Uzan, J., & Bernardeau, F. 2008, *Phys. Rev. D*, **78**, 063526
- Plagge, T., et al. 2010, *ApJ*, **716**, 1118
- Polnarev, A. G. 1985, *AZh*, **62**, 1041
- Pratt, G. W., Croston, J. H., Arnaud, M., & Böhringer, H. 2009, *A&A*, **498**, 361
- Pyne, T., & Carroll, S. M. 1996, *Phys. Rev. D*, **53**, 2920
- Rees, M. J. 1968, *ApJ*, **153**, L1
- Refsdal, S. 1964, *MNRAS*, **128**, 307
- Reichardt, C. L., et al. 2009, *ApJ*, **694**, 1200
- Reid, B. A., Verde, L., Jimenez, R., & Mena, O. 2010a, *J. Cosmol. Astropart. Phys.*, **JCAP01(2010)003**
- Reid, B. A., et al. 2010b, *MNRAS*, **404**, 60
- Rephaeli, Y. 1995, *ARA&A*, **33**, 541
- Riess, A. G., et al. 1998, *AJ*, **116**, 1009
- Riess, A. G., et al. 2009, *ApJ*, **699**, 539
- Rozo, E., et al. 2010, *ApJ*, **708**, 645
- Rubiño-Martín, J. A., Chluba, J., Fendt, W. A., & Wandelt, B. D. 2010, *MNRAS*, **403**, 439
- Rudd, D. H., & Nagai, D. 2009, *ApJ*, **701**, L16
- Sachs, R. K., & Wolfe, A. M. 1967, *ApJ*, **147**, 73
- Saito, S., Takada, M., & Taruya, A. 2008, *Phys. Rev. Lett.*, **100**, 191301
- Saito, S., Takada, M., & Taruya, A. 2009, *Phys. Rev. D*, **80**, 083528
- Salopek, D. S., & Bond, J. R. 1990, *Phys. Rev. D*, **42**, 3936
- Sato, K. 1981, *MNRAS*, **195**, 467
- Schneider, P., Kochanek, C. S., & Wambsganss, J. 2006, Gravitational Lensing: Strong, Weak and Micro (Berlin: Springer)
- Schrabback, T., et al. 2010, *A&A*, **516**, A63

- Scott, D., & Moss, A. 2009, *MNRAS*, **397**, 445
- Seager, S., Sasselov, D. D., & Scott, D. 1999, *ApJ*, **523**, L1
- Seager, S., Sasselov, D. D., & Scott, D. 2000, *ApJS*, **128**, 407
- Seckel, D., & Turner, M. S. 1985, *Phys. Rev. D*, **32**, 3178
- Seery, D., & Lidsey, J. E. 2005, *J. Cosmol. Astropart. Phys.*, **JCAP06(2005)003**
- Sehgal, N., Bode, P., Das, S., Hernandez-Monteagudo, C., Huffenberger, K., Lin, Y., Ostriker, J. P., & Trac, H. 2010, *ApJ*, **709**, 920
- Sekiguchi, T., Ichikawa, K., Takahashi, T., & Greenhill, L. 2010, *J. Cosmol. Astropart. Phys.*, **JCAP03(2010)015**
- Seljak, U. 2000, *MNRAS*, **318**, 203
- Seljak, U., Pen, U.-L., & Turok, N. 1997, *Phys. Rev. Lett.*, **79**, 1615
- Seljak, U., & Zaldarriaga, M. 1996, *ApJ*, **469**, 437
- Seljak, U., & Zaldarriaga, M. 1997, *Phys. Rev. Lett.*, **78**, 2054
- Senatore, L., Smith, K. M., & Zaldarriaga, M. 2010, *J. Cosmol. Astropart. Phys.*, **JCAP01(2010)028**
- Senatore, L., Tashev, S., & Zaldarriaga, M. 2009a, *J. Cosmol. Astropart. Phys.*, **JCAP08(2009)031**
- Senatore, L., Tashev, S., & Zaldarriaga, M. 2009b, *J. Cosmol. Astropart. Phys.*, **JCAP09(2009)038**
- Serra, P., & Cooray, A. 2008, *Phys. Rev. D*, **77**, 107305
- Shaw, L. D., Zahn, O., Holder, G. P., & Doré, O. 2009, *ApJ*, **702**, 368
- Shoji, M., & Komatsu, E. 2009, *ApJ*, **700**, 705
- Siemens, X., Creighton, J., Maor, I., Majumder, S. R., Cannon, K., & Read, J. 2006, *Phys. Rev. D*, **73**, 105001
- Siemens, X., Mandic, V., & Creighton, J. 2007, *Phys. Rev. Lett.*, **98**, 111101
- Sievers, J. L., et al. 2007, *ApJ*, **660**, 976
- Sikivie, P. 2008, Axions (Lect. Notes Phys., Vol. 741; Berlin: Springer), 19
- Silverstein, E., & Tong, D. 2004, *Phys. Rev. D*, **70**, 103505
- Simha, V., & Steigman, G. 2008, *J. Cosmol. Astropart. Phys.*, **JCAP06(2008)016**
- Slosar, A. 2006, *Phys. Rev. D*, **73**, 123501
- Slosar, A., Hirata, C., Seljak, U., Ho, S., & Padmanabhan, N. 2008, *J. Cosmol. Astropart. Phys.*, **JCAP08(2008)031**
- Smidt, J., Amblard, A., Serra, P., & Cooray, A. 2009, *Phys. Rev. D*, **80**, 123005
- Smith, K. M., Senatore, L., & Zaldarriaga, M. 2009, *J. Cosmol. Astropart. Phys.*, **JCAP09(2009)006**
- Smith, K. M., Zahn, O., & Doré, O. 2007, *Phys. Rev. D*, **76**, 043510
- Smith, K. M., & Zaldarriaga, M. 2006, arXiv:astro-ph/0612571
- Smith, R. E., et al. 2003, *MNRAS*, **341**, 1311
- Smith, T. L., Pierpaoli, E., & Kamionkowski, M. 2006, *Phys. Rev. Lett.*, **97**, 021301
- Song, Y.-S., Hu, W., & Sawicki, I. 2007, *Phys. Rev. D*, **75**, 044004
- Spergel, D. N., & Zaldarriaga, M. 1997, *Phys. Rev. Lett.*, **79**, 2180
- Spergel, D. N., et al. 2003, *ApJS*, **148**, 175
- Spergel, D. N., et al. 2007, *ApJS*, **170**, 377
- Staniszewski, Z., et al. 2009, *ApJ*, **701**, 32
- Starobinskii, A. A. 1979, Sov. JETP Lett., **30**, 682
- Starobinsky, A. A. 1982, *Phys. Lett. B*, **117**, 175
- Starobinsky, A. A. 2007, Sov. JETP Lett., **86**, 157
- Steigman, G. 2007, *Annu. Rev. Nucl. Part. Sci.*, **57**, 463
- Steigman, G. 2008, arXiv:0807.3004
- Stickel, M., Meisenheimer, K., & Kühr, H. 1994, *A&AS*, **105**, 211
- Sunyaev, R. A., & Zel'dovich, Y. B. 1972, *Comments Astrophys. Space Phys.*, **4**, 173
- Suto, Y., Sasaki, S., & Makino, N. 1998, *ApJ*, **509**, 544
- Suyu, S. H., Marshall, P. J., Auger, M. W., Hilbert, S., Blandford, R. D., Koopmans, L. V. E., Fassnacht, C. D., & Treu, T. 2010, *ApJ*, **711**, 201
- Suyu, S. H., Marshall, P. J., Blandford, R. D., Fassnacht, C. D., Koopmans, L. V. E., McKean, J. P., & Treu, T. 2009, *ApJ*, **691**, 277
- Switzer, E. R., & Hirata, C. M. 2008, *Phys. Rev. D*, **77**, 083006
- Takada, M., Komatsu, E., & Futamase, T. 2006, *Phys. Rev. D*, **73**, 083520
- Takahashi, Y. D., et al. 2010, *ApJ*, **711**, 1141
- Teräsraanta, H., Urpo, S., Wieren, S., & Valtonen, M. 2001, *A&A*, **368**, 431
- Thomas, S. A., Abdalla, F. B., & Lahav, O. 2010, *Phys. Rev. Lett.*, **105**, 031301
- Trotta, R., & Hansen, S. H. 2004, *Phys. Rev. D*, **69**, 023509
- Turner, M. S., & Wilczek, F. 1991, *Phys. Rev. Lett.*, **66**, 5
- Upadhye, A. 2007, *Nucl. Phys. Proc. Suppl.*, **173**, 11
- Verde, L., & Spergel, D. N. 2002, *Phys. Rev. D*, **65**, 043007
- Verde, L., Wang, L., Heavens, A. F., & Kamionkowski, M. 2000, *MNRAS*, **313**, 141
- Vikhlinin, A., Burenin, R., Forman, W. R., Jones, C., Hornstrup, A., Murray, S. S., & Quintana, H. 2007, in ESO Astrophysics Symposia, Heating versus Cooling in Galaxies and Clusters of Galaxies, ed. H. Böhringer et al. (Berlin: Springer), 48
- Vikhlinin, A., Kravtsov, A., Forman, W., Jones, C., Markevitch, M., Murray, S. S., & Van Speybroeck, L. 2006, *ApJ*, **640**, 691
- Vikhlinin, A., et al. 2009a, *ApJ*, **692**, 1033
- Vikhlinin, A., et al. 2009b, *ApJ*, **692**, 1060
- Wandelt, B. D. 2003, in Statistical Problems in Particle Physics, Astrophysics, and Cosmology, ed. L. Lyons, R. Mount, & R. Reitmeyer (Menlo Park, CA: SLAC), 229
- Wandelt, B. D., Larson, D. L., & Lakshminarayanan, A. 2004, *Phys. Rev. D*, **70**, 083511
- Wang, L., & Steinhardt, P. J. 1998, *ApJ*, **508**, 483
- Wang, S., Haiman, Z., Hu, W., Khouri, J., & May, M. 2005, *Phys. Rev. Lett.*, **95**, 011302
- Wang, Y. 2008, *Phys. Rev. D*, **77**, 123525
- Wang, Y. 2009, *Phys. Rev. D*, **80**, 123525
- Wang, Y., & Mukherjee, P. 2007, *Phys. Rev. D*, **76**, 103533
- Weiland, J. L., et al. 2011, *ApJS*, **192**, 19
- Weinberg, S. 2008, Cosmology (Oxford: Oxford Univ. Press)
- Wik, D. R., Sarazin, C. L., Finoguenov, A., Matsushita, K., Nakazawa, K., & Clarke, T. E. 2009, *ApJ*, **696**, 1700
- Wong, K., & Sarazin, C. L. 2009, *ApJ*, **707**, 1141
- Wong, W. Y., Moss, A., & Scott, D. 2008, *MNRAS*, **386**, 1023
- Wong, Y. Y. Y. 2008, *J. Cosmol. AstroPart. Phys.*, **JCAP10(2008)035**
- Wright, E. L. 2006, *PASP*, **118**, 1711
- Wright, E. L. 2007, *ApJ*, **664**, 633
- Wu, E. Y. S., et al. 2009, *Phys. Rev. Lett.*, **102**, 161302
- Xia, J.-Q., Li, H., Wang, X., & Zhang, X. 2008a, *A&A*, **483**, 715
- Xia, J.-Q., Li, H., & Zhang, X. 2010, *Phys. Lett. B*, **687**, 129
- Xia, J.-Q., Li, H., Zhao, G.-B., & Zhang, X. 2008b, *Phys. Rev. D*, **78**, 083524
- Xia, J.-Q., Li, H., Zhao, G.-B., & Zhang, X. 2008c, *ApJ*, **679**, L61
- Xia, J.-Q., Zhao, G.-B., Feng, B., Li, H., & Zhang, X. 2006, *Phys. Rev. D*, **73**, 063521
- Yadav, A. P. S., Komatsu, E., Wandelt, B. D., Liguori, M., Hansen, F. K., & Matarrese, S. 2008, *ApJ*, **678**, 578
- Yadav, A. P. S., & Wandelt, B. D. 2008, *Phys. Rev. Lett.*, **100**, 181301
- Yamamoto, K., & Futamase, T. 2001, *Prog. Theor. Phys.*, **105**, 707
- Yamamoto, K., Kadoya, Y., Murata, T., & Futamase, T. 2001, *Prog. Theor. Phys.*, **106**, 917
- Yamamoto, K., Parkinson, D., Hamana, T., Nichol, R. C., & Suto, Y. 2007, *Phys. Rev. D*, **76**, 023504
- Zaldarriaga, M. 1997, *Phys. Rev. D*, **55**, 1822
- Zaldarriaga, M. 2004, *Phys. Rev. D*, **69**, 043508
- Zaldarriaga, M., & Seljak, U. 1997, *Phys. Rev. D*, **55**, 1830
- Zel'dovich, Y. B., & Sunyaev, R. A. 1969, *Ap&SS*, **4**, 301
- Zhang, P., Liguori, M., Bean, R., & Dodelson, S. 2007, *Phys. Rev. Lett.*, **99**, 141302
- Zhao, G.-B., Xia, J.-Q., Feng, B., & Zhang, X. 2007, *Int. J. Mod. Phys. D*, **16**, 1229
- Zhao, G.-B., Xia, J.-Q., Li, M., Feng, B., & Zhang, X. 2005, *Phys. Rev. D*, **72**, 123515